



University of Antwerp

Faculteit Wetenschappen
Departement Fysica

**Quantification of 3D atomic positions for nanoparticles
using scanning transmission electron microscopy:
statistical parameter estimation, dose-limited precision
and optimal experimental design**

**Kwantitatieve bepaling van 3D atomaire posities in
nanodeeltjes met rastertransmissie-elektronenmicroscopie:
statistisch parameterschatten, dosisgelimiteerde precisie
en optimale proefopzet**

Proefschrift voorgelegd tot het behalen van de graad van
doctor in de Wetenschappen aan de Universiteit Antwerpen te
verdedigen door

Marcos Alania

Promotor:
Prof. Dr. Sandra Van Aert

Antwerpen, 2017

Doctoral Committee

Chairman

Prof. Dr. Nick Van Remortel, University of Antwerp - Belgium

Promotor

Prof. Dr. Sandra Van Aert

Members

Prof. Dr. Dirk Lamoen , University of Antwerp - Belgium

Prof. Dr. Dirk Van Dyck, University of Antwerp - Belgium

Dr. Marco Schowalter, University of Bremen - Germany

Dr. Gerardo T. Martinez , University of Oxford - United Kingdom

Contact information

Marcos Antonio Alania Vicente

University of Antwerp - Department of Physics

EMAT - Electron Microscopy for Materials Science

Groenenborgerlaan 171

B-2020 Antwerp

Belgium

To my parents, my sisters and brother

Summary

Material properties are strongly connected to the atomic structure and chemical composition. For bulk materials, most of their properties can be measured and are well understood. However, for small particles such as nanoparticles or nanoclusters with sizes in the order of the nanometric scale ($1\text{nm}=10^{-9}\text{m}$) these properties differ from both atoms (molecules) and bulk matter. Thanks to their unique properties and numerous applications in a wide range of materials and devices, these types of particles have attracted enormous attention from the scientific and industrial community during the last years. It has been proven, both theoretically and experimentally, that the structure of such nanomaterials is connected to their characteristic properties. Therefore, in order to deeply understand their properties, a detailed structural characterization and chemical mapping at atomic level are required.

High resolution (HR) scanning transmission electron microscopy (STEM) is established as one of the experimental techniques to determine the internal structure of materials at the atomic scale. Especially when using the high angle annular dark field detector (HAADF) allows one to acquire atomically resolved images of materials, which are sensitive to their structure and chemical composition. However, one should never forget that STEM images correspond to two-dimensional (2D) projections of a three-dimensional (3D) object and very often such images cannot be used for a detailed 3D structural and morphological characterization. In order to obtain reliable 3D information, electron tomography has evolved toward a standard technique, which when combined with advanced reconstruction algorithms, enables one to visualize atoms and even determine in some nanoparticles the chemical nature atom-by-atom.

Once the atomic columns or individual atoms can be resolved in 2D or 3D, respectively, the next challenge is to refine their positions and composition in a quantitative manner in order to measure these structure parameters as precisely as possible. Although HR STEM is capable of reaching sub-Angstrom resolution, quantitative structural and chemical determination require both statistical parameter estimation and image simulations. Statistical parameter estimation theory allows us to estimate the parameters by fitting a parametric model to the experimental images, where parameters of the model are measured in an

iterative manner by optimising a criterion of goodness of fit. Image simulations allow us to interpret the quantum mechanical nature of the electron-specimen interaction, and are used for comparison with the experimental images in order to validate the estimated parameters. In order to develop a method that allows us to quantify the theoretical limits with which atomic columns or atoms of a nanocluster can be located in 2D and 3D, respectively, from a STEM experiment, the combination of both statistical parameter estimation and image simulations is proposed. The concept is explored from a theoretical point of view.

This thesis can be divided into four parts. The first part consist of a general introduction where the motivation and the relevance of the research is described in chapter 1. The second part summarizes the theory about the physics of the image formation in the STEM and the basic principles of statistical parameter estimation theory, in chapters 2 and 3, respectively. The third part consists of the results of this work which are discussed in chapters 4, 5 and 6. In chapter 4, the reliability of two of the most popular methods used to perform STEM image simulation are compared in terms of the parameters that are commonly used for image quantification including the integrated intensity and the precision of the atomic columns. In chapter 5, the theoretical limit with which atoms of a nanocluster can be located in 3D based on the acquisition of a tilt series of annular dark field (ADF) STEM images is explored. This study is based on the concept of the Fisher information matrix that allows us to determine an expression for the highest attainable precision with which atoms can be located in 3D. Furthermore, using this criterion some of the experimental settings are optimized. In chapter 6, the same concept is used to investigate the attainable precision with which the depth location of atoms and the centre of mass of an isolated column can be measured from a focal-series of images acquired with HAADF STEM. In addition, a 3D reconstruction method based on a focal series of HAADF STEM images is developed. Finally, in the fourth part, the general conclusions and future perspectives are drawn in chapter 7.

Contents

1	Introduction	1
1.1	Nanotechnology and nanomaterials	1
1.2	Nanomaterials	2
1.3	The scanning transmission electron microscope	6
1.4	Characterization techniques in 3D by using HAADF STEM	8
1.5	Quantitative HAADF STEM	9
1.6	This PhD thesis	11
2	Physics of the image formation in ADF-STEM	13
2.1	Introduction	13
2.2	Electron-probe formation	15
2.3	Specimen model	16
2.4	Electron-specimen interaction	17
2.5	Multislice method	20
2.6	Thermal vibration	22
2.6.1	Frozen phonon	22
2.6.2	Absorptive Potential	24
2.7	Intensity integration over the detector	26
2.8	Simulation programs	26
2.8.1	MULTEM	27
2.8.2	STEMSIM	27
2.9	Conclusions	29
3	Statistical parameter estimation theory	31
3.1	Introduction	31
3.2	Parametric model for the intensity observations	33
3.3	Statistical measurement precision	34
3.3.1	The joint probability density function of the observations	35
3.3.2	The Cramér-Rao lower bound	36
3.3.2.1	Fisher information matrix	36
3.3.2.2	Cramér-Rao inequality	37
3.4	Precision and experimental design	38
3.5	Maximum likelihood estimation	39

3.6	Conclusions	40
4	Comparison of frozen phonon and absorptive potential model for HAADF STEM image simulation	41
4.1	Introduction	41
4.2	Simulation parameters	42
4.3	Integrated intensity	43
4.3.1	Distribution over the annular detector	44
4.3.2	Isolated column	47
4.3.3	FCC structure	49
4.4	The ultimate precision to locate atoms	52
4.4.1	Isolated column	52
4.4.2	FCC structure	54
4.5	Conclusions	55
5	Ultimate precision of locating atoms of a nanocluster in 3D from a tilt series of STEM images	57
5.1	Introduction	57
5.2	Parametric model for the intensity observations	59
5.2.1	Rotation of a nanocluster	59
5.2.2	The Gaussian approximation model	60
5.3	Statistical measurement precision	61
5.4	Simulation settings	64
5.5	Results and discussion	65
5.5.1	Calculation of the attainable precision	65
5.5.2	Determination of the number of simulations for the computation of the attainable precision	66
5.5.3	The optimal angular tilt range	68
5.5.4	The optimal number of projection images	68
5.5.5	The optimal detector range	69
5.5.6	The attainable precision for locating the central atom	71
5.5.7	The precision as a function of the incident electron dose	72
5.5.8	The effect of the finite size of the source on the precision	73
5.5.9	The effect of the Debye-Waller factor on the precision	74
5.6	Conclusions	75
6	Three-dimensional particle reconstruction by depth sectioning in High-Angle Annular Dark-Field Scanning Transmission Electron Microscopy	77
6.1	Introduction	77
6.2	Statistical measurement precision for the depth location	80
6.3	Numerical results	80
6.4	3D atomic scale reconstruction of nanosized structures	83

CONTENTS	vii
6.4.1 Reconstruction algorithm	83
6.4.2 Experimental 3D reconstruction of a Au nanorod	84
6.5 Conclusion	88
7 General conclusions	89
A The effect of the neighbouring columns in the computation of the CRLB	93
B Fisher information matrix for the Gaussian model	95
B.1 Rotation matrix	95
B.2 Rotation model for the Gaussian method	96
B.3 Fisher information matrix for the central atom	96
References	117

Chapter 1

Introduction

1.1 Nanotechnology and nanomaterials

Nature has always used nanotechnology to synthesize molecular structures in the body such as enzymes, proteins, carbohydrates and lipids, which form components of cellular structures [Ahmed and Crean, 2014]. However, the beginning of nanotechnology as a concept is attributed to Richard P. Feynman after his talk "*There's Plenty of Room at the Bottom*" presented to the American Physical Society in Pasadena-California on the 29 December 1959. In this talk, Richard P. Feynman described the interesting possibilities that would open up when scientist would be able to manipulate and control single atoms and molecules, and to improve the performance of instruments such as electron microscopes. In one of his examples, he explained in detail how we would be able to write the entire 24 volumes of the Encyclopedia Britannica on the head of a pin, and read them by using an electron microscope. He also talked about the rearrangement of the atoms at atomic scale predicting the new properties that would appear due to the predominance of the laws of the quantum mechanics at this scale. The purpose of this talk was to challenge the physicists at the meeting: first, to get them to see that these things were possible and, second, to make them happen. The transcription of this talk was later published as a paper in California Institute of Technology Quarterly, a volume of essays entitled Miniaturization, and in the Technion Yearbook for 1962 [Toumey, 2009]. In this talk, Richard P. Feynman never mentioned the word *nanotechnology*. The first use of this word was by Norio Taniguchi in his paper "*On the basic concept of nanotechnology*" published in 1974 [Taniguchi et al., 1974], and the word became more popular after the publication of the book "*Engines of Creation: The Coming Era of Nanotechnology*" by Eric Drexler in 1986 [Drexler, 1986]. These three publications are cited in most of the articles related to the beginnings of nanotechnology and are often considered as the three pillars of nanotechnology. According to the Oxford dictionary, the word *nanotechnology* is defined as the branch of technology that deals with dimensions and tolerances of less than 100 nanometres ($1\text{nm}=10^{-9}\text{m}$),

especially the manipulation of individual atoms and molecules. The study of objects, structures, and phenomena at this scale (nanometric-scale), is known as nanoscience, which together with nanotechnology, are in charge of the study and application of nanomaterials that can be used across all the other science fields, such as chemistry, biology, physics, materials science, engineering, etc. Thanks to the evolution of nanotechnology we have numerous benefits such as:

- faster, smaller, and more powerful computers, smartphones and many other electronic devices,
- faster, more functional, and more accurate medical diagnostic equipment,
- use of nanoparticles in pharmaceutical products, improving in this way their absorption within the body and make them easier to be delivered,
- improved vehicle fuel efficiency and corrosion resistance by building vehicle parts from nanocomposite materials that are lighter, stronger, and more chemically resistant than metals,
- carbon nanotubes, having a variety of commercial uses, including the fabrication of stronger and at the same time lighter sports equipment,
- fabrication of chemical sensors, programmed to detect a particular chemical at single molecule level.

In figure 1.1 a length scale is presented in which the size of nanomaterials is compared to the size of different objects.

1.2 Nanomaterials

During the last few decades, nanomaterials have been gaining a great interest in a wide range of scientific and industrial fields. The main reason for this trend is that materials and structures having small dimensions present outstanding properties, enabling one to develop new materials, devices, solutions, etc. However, since the ancient times, nanomaterials have been widely used due to their unique properties, without knowing the scientific facts behind them. Such an example is the Lycurgus cup, which is currently located in the British Museum [Husain and Khan, 2016]. The word nanomaterial is typically used to describe a material in which at least one of the three dimensions is ranging from 1 to about 100 nm [Gwinn and Vallyathan, 2006, Simon Kaluza, 2009, Ahmed and Crean, 2014]. According to this definition, nano-objects can be classified into three main groups: 2D nano-objects (e.g. thin films), 1D nano-objects (e.g. nanowires, nanorods, and nanotubes) and 0D nano-objects, such as nanoparticles [Pokropivny and Skorokhod, 2007, Tiwari et al., 2012, Altantzis, 2015]. At

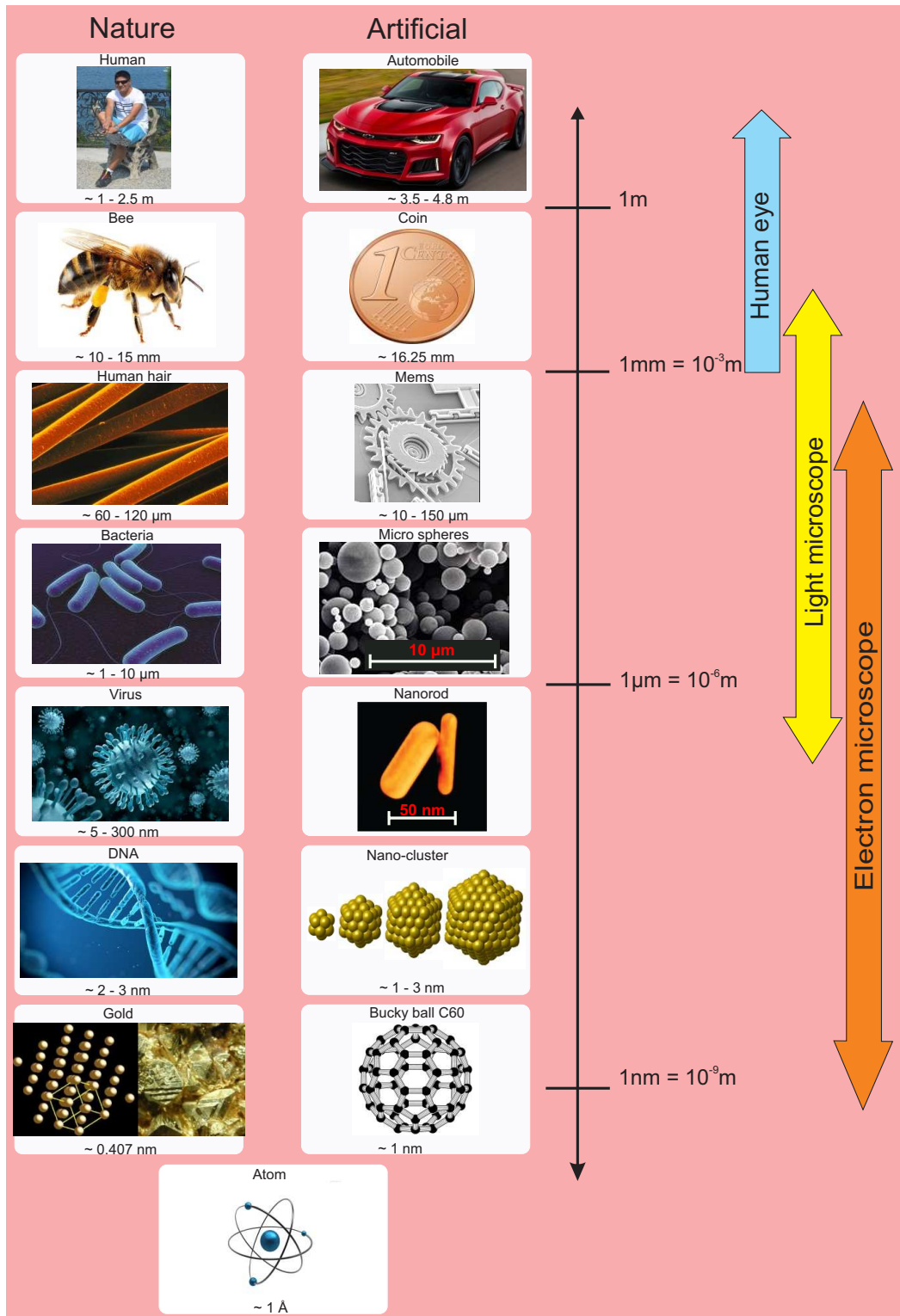


Figure 1.1: Length scale defining the size range of different objects.

this scale, the properties of nanomaterials are inseparably connected to their size. The reduction of size induces new properties and phenomena that cannot be seen at the bulk level [Husain and Khan, 2016]. In order to understand and explain or even being able to enhance these properties and phenomena, the structural characterization of nanomaterials, combined with theoretical modelling is of great importance. A technique which can be used for the structural characterization of such materials is transmission electron microscopy (TEM). In the frame of my thesis, different approaches were developed aiming on a quantitative analysis of nanoparticles (0D nano-objects), with a focus on gold nanoparticles.

Nanoparticles

Nanoparticles can be defined as aggregates of a few up to many millions of atoms or molecules [Ferrando et al., 2008]. They may consist of identical atoms, or molecules, or two or more different species and can be studied in a number of media, such as molecular beams, the vapour phase, and colloidal suspensions, and isolated in inert matrices or on surfaces [Jellinek, 1999, Johnston, 2002, Haberland, 2012, Martin, 2012]. One of the most important features of nanoparticles is that their properties depend on their size and shape, which is defined by the atomic arrangement. This size dependence is related to several phenomena such as quantum effects, surface area, optical properties, modification of thermal behaviour, among others [Mock et al., 2002, Sao-Joao et al., 2005, Ferrando et al., 2008, Jellinek, 2008, Khanal et al., 2014]. In order to under-

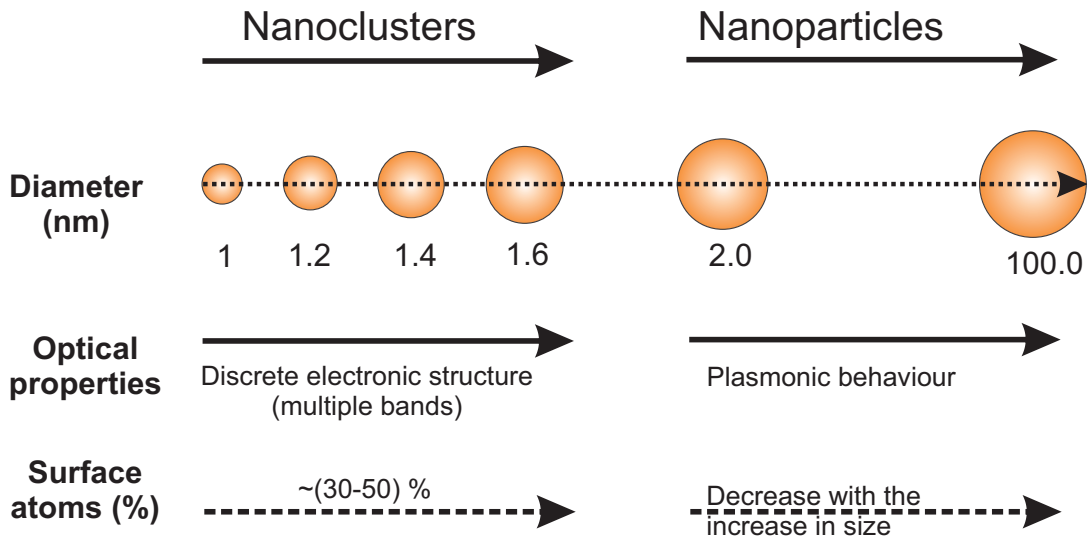


Figure 1.2: Length scale defining the size range of atomic clusters and nanoparticles, including the behaviour of their optical properties and the amount of surface atoms in percentage. This figure has been adapted from reference [Deepak et al., 2015].

stand and fully characterize these properties, researchers from different scientific fields, including also the field of materials science, are collaborating with each other. The importance of their unique physical and chemical properties is that they provide a particularly useful platform with a wide-range of potential applications. Particles consisting of a relatively small number of atoms and yielding only one or very few stable geometric structures are defined as atomic clusters. Their size is comparable to the Fermi wavelength of an electron and they can therefore be considered as a bridge between atoms and nanoparticles. A main difference between a nanoparticle and a cluster is that in the latter case, the physical properties vary greatly with every addition or subtraction of an atom, i.e. the quantum effects are dominant. When the number of atoms increases, the plasmonic effect [Notarianni et al., 2014] starts to appear. According to this reference [Deepak et al., 2015], the size for which of the plasmon resonance [Notarianni et al., 2014] is produced should be considered as the boundary between clusters and nanoparticles, as is illustrated in figure 1.2.

- **Synthesis:** There are several methods for the synthesis of nanoparticles. According to [Altantzis, 2015], the synthesis methods can be classified into three main groups: a) Grinding methods, including both wet or dry grinding or reactive grinding [Christodoulou et al., 2007, Zhang et al., 2007] b) Gas-phase methods such as chemical vapor deposition (CVD), laser ablation deposition (LAD), sputtering techniques [Gutsch et al., 2005, Vollath, 2008] and c) liquid phase synthesis methods, including sol-gel processes and micro-emulsion methods [Vollath, 2008, Rao et al., 2006, Burda et al., 2005]. In figure 1.3 an illustration of the "Top-down" and "the Bottom-up" approaches that are commonly used to synthesize nanoparticles are shown.
- **Applications:** Nanoparticles are used in a wide range of scientific fields, due to their peculiar properties, morphologies and shapes. From all nanoparticles, gold nanoparticles are probably among the most extensively studied [Johnston and Wilcoxon, 2012] and applied nanoparticles. Many books and papers can be found in literature which are entirely dedicated to the study of the properties and applications of gold nanoparticles [Murphy et al., 2008, Louis et al., 2012, Valcárcel and López-Lorente, 2014]. According to the following references [Tylecote, 1992, Louis et al., 2012], the first use of gold nanoparticles was around 1500 years ago as a decorative purpose (e.g. the Lycurgus cup). More recently, gold nanoparticles have been used in various fields of nanotechnology exploiting their electronic, optical, catalytic, decorative, biotechnological and medical properties [Louis et al., 2012] and [Khan et al., 2014].

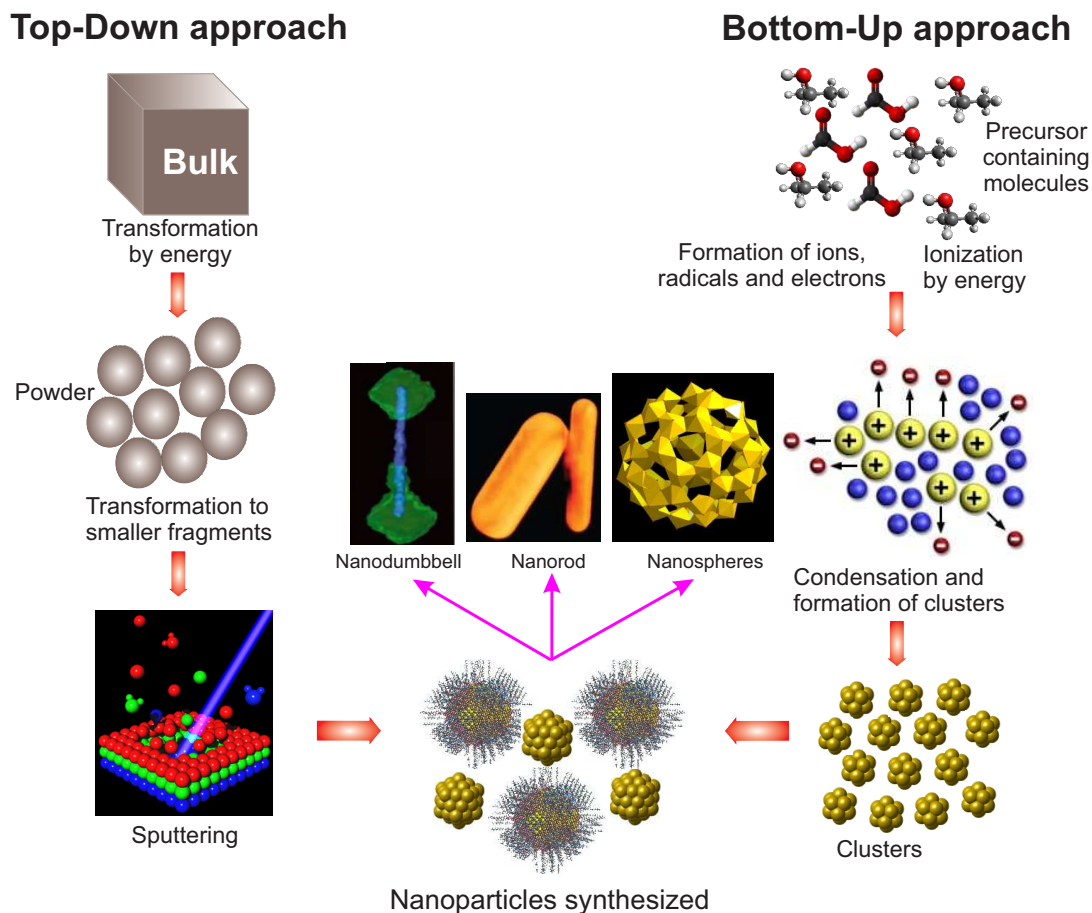


Figure 1.3: Illustration of the bottom-up and top-down approaches, adapted from reference [Habiba et al., 2014].

1.3 The scanning transmission electron microscope

The history of electron microscopy is very rich and starts after the discovery that mass particles such as electrons possess a wavelike character. Louis de Broglie in his PhD thesis proposed that just as light has both wave-like and particle-like properties, electrons have wave-like properties as well. By 1927 the experiment of C. J. Davisson and L. H. Germer [Davisson and Germer, 1928] confirmed the De Broglie's hypothesis and it was observed that electrons accelerated at 54 V are strongly diffracted from the regular array of atoms at the surface of the crystal. In the same year, increasing the acceleration voltage up to 50 kV, G. P. Thomson [Thomson, 1928] demonstrated that it is possible to form an electron diffraction pattern from electrons that have passed through a thin specimen. Four years later (1931), E. Ruska and M. Knoll [Knoll and Ruska, 1932] developed the first transmission electron microscope, where instead of glass lenses electromagnetic ones were used. At the same time, they also observed their

first transmission image (magnification = 17) of a metal grid. By 1933, Ruska added a third lens and obtained images of cotton fibre and aluminium foil with a resolution somewhat better than that of the light microscope. Similar microscopes were built by Marton and co-workers in Brussels, who by 1934 had produced the first images of nuclei within the interior of biological cells [Marton, 1934]. Since then, the TEM has evolved into a rather complex instrument. Now, the modern TEM can be operated in two different modes: the conventional (C) TEM (same as the first electron microscope) and the scanning (S) TEM, which was developed shortly after the CTEM by Von Ardenne [Von Ardenne, 1938] and greatly improved in the late 1960s by Crewe et al. [Crewe et al., 1968].

Both CTEM and STEM have been applied in many scientific and industrial fields. For example, it is widely used in semiconductor technology and data storage (e.g. defect analysis, failure analysis) [Kacher et al., 2015, Rai and Subramanian, 2009]; in biological and life sciences (e.g. mass measurement, structure and mapping information) [Wall and Hainfeld, 1986, Hainfeld and Wall, 1988, Engel and Colliex, 1993, Wall and Simon, 2001] and in materials science (e.g. characterization of porous system, characterization of nanoparticles, materials qualifications, quantitative and structural characterization in 3D) [Chalmers et al., 2012, Utsunomiya and Ewing, 2003, Hata et al., 2015]. After progress in hardware (e.g. Camera length, monochromator, detectors) and software, as well as in the development of aberration correctors, sub-angstrom resolution even in a mid-voltage microscope can be achieved [O’Keefe et al., 2005, Lentzen, 2006]. These improvements have turned TEM today into one of the most versatile and powerful tools enabling structural characterization and chemical mapping at the atomic scale [Van Aert et al., 2009, Grieb et al., 2013].

Although modern HRTEM is capable of reaching sub-angstrom resolution in both CTEM and STEM, difficulties in interpreting conventional HRTEM images, causing a strong dependence on the imaging parameters and dynamical diffraction effects, mostly arise from the coherent nature of the illumination [Nellist and Pennycook, 2000]. The use of incoherent imaging modes, such as the high angular annular dark field (HAADF) STEM, brings major benefits in the interpretation of the acquired images. In STEM [Pennycook and Nellist, 2011, Tanaka, 2014], an electron beam is focused into a fine probe that is scanned across the sample in a two-dimensional (2D) raster [Crewe et al., 1968]. For each probe position, the electrons scattered towards the detector are integrated and displayed as a function of the probe position. In HAADF STEM mode, an annular detector is used with a collection range outside of the illumination cone (greater than the aperture size). The high-angle scattering is mainly dominated by Rutherford and thermal diffuse scattering (TDS). Therefore, the HAADF signal emitted by each atom contributes incoherently [Loane et al., 1992, Hartel et al., 1996] and is sensitive to the structural and chemical information of the

specimen [Hartel et al., 1996, Nellist and Pennycook, 2000, Wang et al., 2011]. These advantages make HAADF STEM one of the most promising techniques to fully characterize materials in three dimensions (3D).

1.4 Characterization techniques in 3D by using HAADF STEM

Characterization techniques for nanotechnology applications refer to the study of material's features such as shape, structure, chemical composition, and some physical and chemical properties. In the previous section, we already mentioned that one of the most powerful techniques available with sub-angstrom resolution, is the aberration-corrected HAADF STEM technique due to the strong sensitivity to the structural and chemical composition. However, one should never forget that the results provided by the technique are only 2D projections of a 3D object. Therefore, to retrieve the information in 3D, alternative techniques should be used. Two techniques which have been widely implemented are:

- **Electron tomography:** Electron tomography has become a standard characterization technique to investigate the morphology of nanomaterials in 3D [Jinnai et al., 2000, Midgley et al., 2001, Cha et al., 2007, Bals et al., 2007, Midgley et al., 2007]. Given the aperiodic nature of the nanoparticles, it is of great importance to investigate their structure and composition in 3D [Bals et al., 2014]. In this technique, the specimen (e.g. a gold nanoparticle) is located parallel to the electron beam and acquisition of a tilt series from a part of the specimen under investigation is performed. The most popular acquisition geometries are based on a single tilt acquisition scheme, where a TEM holder is placed in between the upper and lower pole pieces of the objective lens [Altantzis, 2015]. For tomography, it is important to collect as many images as possible (e.g. using a tilt increment of 1° or 2°) covering an angular range that is preferably as wide as possible. The next step is to align the tilt series of projection images, using, for example, cross- or phase-correlation. Then, the 3D reconstruction of the original object can be obtained by using a mathematical algorithm. For further details about this technique, we suggest the following references [Frank, 1992, Van Tendeloo et al., 2012, Bals et al., 2014, Carter and Williams, 2016] to the reader.
- **Depth sectioning:** The improvement in the ability to correct the aberrations of the electron probe-forming lenses in modern (S)TEM microscopes provides not only a significant improvement in transverse resolution, but also in the lateral or depth resolution, which is a few nanometres [Borisevich et al., 2006, Alania et al., 2016a]. In the depth-sectioning technique, a set of STEM images of the specimen is acquired at different focus positions

of the electron probe, where the focus range should be as symmetrical as possible with respect to the Scherzer condition [Scherzer, 1936]. For the 3D reconstruction of a specimen, this technique could potentially be faster and more dose efficient as compared to traditional tilt-series electron tomography, which is more time-consuming to align and reconstruct [Ercius et al., 2012]. However, it is now well known that typical STEM setups result in a large cone of missing information analogous to the “missing wedge of information” in electron tomography [Xin and Muller, 2009]. This missing information together with the low depth-resolution (few nanometres) is limiting this technique. This technique was successfully applied to detect individual dopant atoms [van Benthem et al., 2005, van Benthem et al., 2006], to identify some complex dislocations [Hirsch et al., 2013, Yang et al., 2015], and to reconstruct a gold nanorod where prior knowledge on the lattice structure was needed [Alania et al., 2016a]. The latter case will be explained in detail in chapter 6.

1.5 Quantitative HAADF STEM

Materials science has evolved from macro- to micro- and, more recently, to nanotechnology [Van Tendeloo et al., 2012, Pag. 281]. As mentioned before in section 1.2, nanomaterials play an important role in nanotechnology due to their outstanding properties. These properties are inseparably connected to the atomic structure and chemical composition. Consequently, one of the main objectives of HAADF STEM is to provide enough information to quantify as precisely as possible the atomic structure and the chemical composition of nanomaterials. In other words, STEM has to evolve from describing to understanding materials properties. Understanding means matching observations with ab-initio calculations [Carter and Williams, 2016, Pag. 267], since their properties depend on the atomic position and atom type.

As mentioned in section 1.3, HAADF STEM imaging conditions hold major benefits in the interpretation of the images due to the strong sensitivity to the structural and chemical composition of the specimen. However, although modern high resolution (HR) STEM is capable of reaching sub-Angstrom resolution, quantitative structure determination requires image simulations to interpret the quantum mechanical nature of the electron-specimen interaction [Jiang et al., 2007, Li et al., 2008, LeBeau et al., 2008, Jones, 2016]. The physical processes of this interaction have been extensively studied and are relatively well understood. There are two principle means of calculating an HAADF STEM image: the Bloch wave method and the multislice method. As a result, many methods for HAADF STEM image simulations have been developed based on both methods [Cowley and Moodie, 1957, Kirkland, 1999, Ishizuka, 2002, Allen et al., 2003, Croitoru

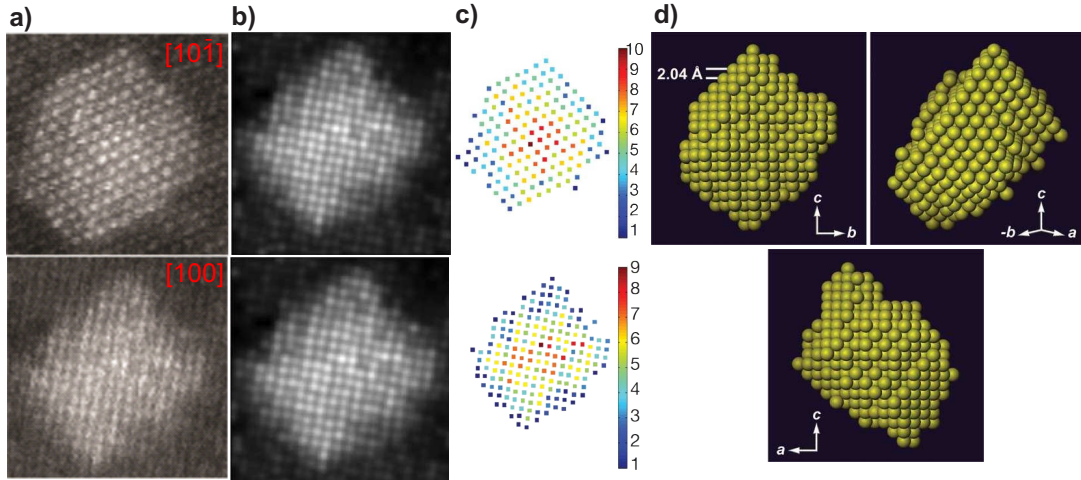


Figure 1.4: Illustration of the 3D atomic reconstruction of Ag nanoparticle. a) Experimental HAADF STEM images of nanosized Ag clusters embedded in an Al matrix along the $[101]$ and $[100]$ zone-axes. b) Refined model of the experimental images of (a). c) Number of Ag atoms per column. d) The computed 3D reconstruction of the Ag nanocluster viewed along three different directions. Figures taken from [Van Aert et al., 2011].

et al., 2006, Rosenauer et al., 2008]. These simulations take into account the TDS (produced by the atomic vibrations) by using the frozen phonon or absorptive potential approaches. The addition of different experimental conditions such as detector geometry [Hillyard and Silcox, 1995], detector sensitivity [LeBeau and Stemmer, 2008, Rosenauer et al., 2009, MacArthur et al., 2014, Martinez et al., 2015], specimen orientation [Klenov et al., 2007], specimen tilt [Maccagnano-Zacher et al., 2008], effect of an amorphous layer [Mkhoyan et al., 2008], strain effects [Grillo, 2009], and source size broadening [Verbeeck et al., 2012] to the simulated STEM images give us a better interpretation of the experiment, reducing the mismatch between the experimental and simulated images, and allowing to quantify the parameters more precisely. The comparison of experimental and simulated images for quantitative analysis can be done in two ways: a) relative measurements, where the maximum and minimum intensities are determined within the image and the results can be re-represented as fractional intensity within the two limits [Rose, 1976] or b) absolute intensity measurement, which is a more complicated processes since the STEM signal often consists of small modulations on a high background [LeBeau et al., 2008].

One step forward in the quantification of HAADF STEM images is the inclusion of statistical analysis methods, which were introduced in order to extract quantitative results from unknown parameters, such as structural and chemical composition of the specimen. In the dynamical process of the electron-specimen

interaction, the observations are usually not the quantities that we want to measure but are related to these quantities. A way to retrieve this information is the use of the principles of statistical parameter estimation theory. These principles have been demonstrated in a wide range of scientific fields as a powerful tool to quantify this type of information. In electron microscopy, it has been shown that by using imaging models, the unknown parameters can be quantified by fitting this model to the experimental HAADF STEM images using a criterion of goodness of fit such as least squares sum or the likelihood function [den Dekker et al., 2005, Van Aert et al., 2005]. For example, by this criterion, optimizing unknown parameters have been quantified such as the atomic column positions in 2D images [De Backer et al., 2011, Gonnissen et al., 2016], the relative quantification of the chemical composition of the atomic columns [Van Aert et al., 2009], or the number of atoms [Van Aert et al., 2013, De Backer et al., 2013]. Taking into account that the theory of the electron-specimen interaction is relative well understood in the mid-range of high voltages, the combination of HAADF STEM image simulations and statistical parameter estimation can also be applied to optimize some settings of the electron microscope such as the optimal detector range [Gonnissen et al., 2016, Alania et al., 2016b], or electron dose [Alania et al., 2016b]. Furthermore, this combination has been useful for the design of new methods of characterization such as the 3D reconstruction of gold nanoparticles by using the atom counting and the depth-sectioning technique [Alania et al., 2016a].

1.6 This PhD thesis

The observations in a STEM experiment, are characterized by a set of pixels values of the image. During the acquisition of the experimental images, both the instrument and the object are subjected to fluctuations which have an effect on the imaging process. As a consequence of these fluctuations, the measurements of the unknown parameters are of limited precision. Therefore, the development of techniques to measure these unknown parameters with high precision is important. In this thesis, we combine the physics of the image formation in STEM and the principles of statistical parameter estimation theory in order to develop a method that allow us to quantify the structural information. The concept of the method is explored from a theoretical point of view. The STEM images were obtained by performing simulations using the multislice algorithm, where the inclusion of the TDS intensity and the experimental conditions mentioned in the previous section are taken into account. The principles of parameter estimation theory were used to find an expression to compute the Cramér-Rao lower bound (CRLB) using the theory of the Fisher information matrix. This expression for the CRLB was used to investigate how precisely the unknown parameters can ultimately be measured from images acquired using ADF STEM. With this

work, we intend to provide crucial insight in the limits of the information with which the unknown structure parameters such as, the atomic column positions and/or individual atom positions can be calculated, or more correctly, can be estimated, from the observations that are acquired experimentally.

Since most of the results in this work were obtained theoretically, the organization of this thesis is as follows. In chapter 2, a mathematical description of the physics of the image formation in ADF STEM is described, starting with the description of the electron probe-forming lenses and their aberrations, followed by the description of the electron-specimen interaction given by the solution of the differential Schrödinger equation and its respective considerations, and finally closing with the integration of the diffracted exit wave over the detector geometry, which gives us a pixel in the process of image formation. In chapter 3, the principles of the statistical parameter estimation theory are introduced and used to derive an expression for the CRLB based on the Fisher information matrix. In chapter 4, both the frozen phonon and the absorptive potential approaches used to calculate the TDS intensity are compared in terms of the integrated intensity and precision. In chapter 5, we investigate how precisely atoms of a nanocluster can ultimately be located in 3D, from a tilt series of images acquired using ADF STEM. In chapter 6, we combine the atom counting method and the depth sectioning technique to develop a method to retrieve the 3D structure of a gold nanorod. Finally in chapter 7, conclusions are drawn.

Chapter 2

Physics of the image formation in ADF-STEM

2.1 Introduction

In experimental transmission electron microscope (TEM), the optics of the illumination system of an scanning (S)TEM is equipped with a high-brightness field emission source [Weiss et al., 1991]. The electrons emitted by the source can be focused by two or more condenser lenses to create a convergent electron beam [Weiss et al., 1991]. Thanks to the progress in aberration-correcting electron optics systems, nowadays, sub-angstrom imaging in both the broad beam and the scanning probe modes are possible [Batson et al., 2002, Nellist et al., 2004, Sawada et al., 2007, Erni et al., 2009]. Figure 2.1 presents a scheme of the STEM configuration. In this scheme, the devices positioned on top of the specimen correspond to the electron-optical arrangement, that has been developed to form a small spot, or probe, over the specimen. Then, after the interaction of this probe with the specimen, the transmitted electrons are transferred to the detector plane. The electrons scattered towards this detector are integrated and displayed as a function of probe position. This process is repeated for each probe position to build the full image.

In this chapter, the physics of the image formation in annular dark field (ADF) STEM will be explained from a theoretical point of view. Following the scheme of figure 2.1 from the top to the bottom. It starts with the mathematical description of the electron-probe formation including the aberrations and compensations of the magnetic lenses. Then, the most difficult and important part in the image formation is the electron-specimen interaction. In this part, when the energetic electrons strike the specimen, many types of reactions such as back scattering, X-rays, Bremsstrahlung, Auger, cathodoluminescence can occur. In our case, only the transmitted electrons that leave the sample under relatively high angles (e.g. larger than the aperture size) with respect to the optical axis

are important. The mathematical description of the electron-specimen interaction starts with the description of the Schrödinger equation and the usual approximations to calculate the total specimen potential. After that, the multislice methods, one of the most popular solutions of the Schrödinger equation, are described. Next, the thermal vibrations of the atoms in the specimen are taken into account, which is important for any quantitative image simulation. Finally, the integration of the intensity over the detector geometry is discussed.

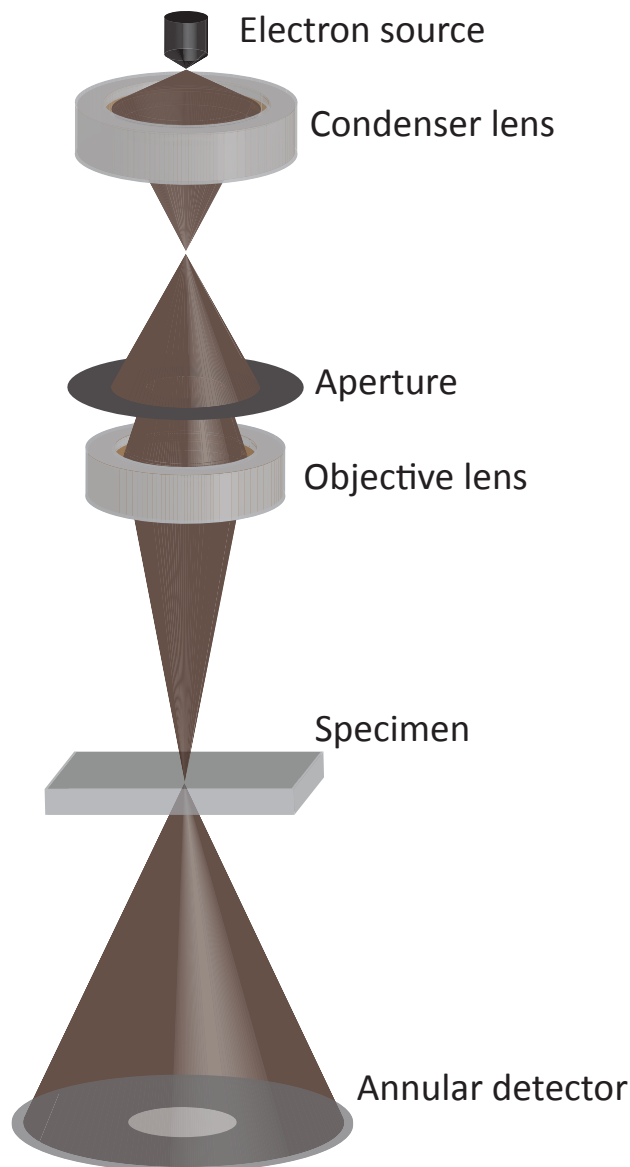


Figure 2.1: Scheme of the Scanning Transmission Electron Microscope STEM.

2.2 Electron-probe formation

Figure 2.1 shows a schematic of the STEM configuration, in which all the devices above the specimen, correspond to the electron-optical arrangement of the electron probe-forming system, in order to form a small spot or probe. The mathematical description of this focused probe is calculated by integrating the aberration wave function $\exp[-i\chi(\mathbf{g})]$ over the objective aperture with translation to a particular point in the image given by [Kirkland, 2010];

$$\psi_p(\mathbf{R}, \mathbf{R}_p) = A_p \int_0^{g_{max}} \exp[-i\chi(\mathbf{g}) - 2i\pi\mathbf{g} \cdot (\mathbf{R} - \mathbf{R}_p)] d^2\mathbf{g} \quad (2.1)$$

where $\mathbf{R} = (x, y)$ is the two-dimensional (2D) Cartesian coordinate vector in the plane, \mathbf{g} is a vector in the spatial frequency domain, $g_{max} = \alpha_{max}/\lambda$ is obtained by dividing the maximum angle in the objective aperture α_{max} by the electron wave length λ , and A_p is a normalization constant chosen such that [Kirkland, 2010]

$$\int |\psi_p(\mathbf{R}, \mathbf{R}_p)|^2 d^2\mathbf{R} = 1. \quad (2.2)$$

The latter equation normalizes the total incident intensity in the electron probe to unity. In this expression, the source is modelled as a point object. The finite size of the source image is generally included by convolving the final image with a normalized Gaussian.

Aberrations and compensation

The aberrations characterize the deviation of the electron wave function from an ideal spherical incoming wave [Kirkland, 2011]. Magnetic lenses have much larger aberration than their light optical counterparts, limiting them to the use of small objective aperture angles. The resolution of the non-corrected electron microscope is mainly limited by the third-order spherical aberration (C_3) [Kirkland, 2010]. In an aberration-corrected instrument, fifth-order spherical aberration (C_5) becomes important because C_3 is controlled and it can be reduced to near zero. It is important to note that correction of the first order aberrations makes it important to consider the aberrations of the next order. Considering aberrations up to the 5th order C_5 , the aberration function can be written as [Kirkland, 2016]

$$\chi(\alpha) = \frac{2\pi}{\lambda} \left(\frac{1}{2}C_1\alpha^2 + \frac{1}{4}C_3\alpha^4 + \frac{1}{6}C_5\alpha^6 \right) \quad (2.3)$$

where λ is the electron wavelength, $C_1 = -\Delta f$ is the defocus (can be defined with either sign) determined by the strength of the objective lens, C_3 is the third-

Table 2.1: Aberration symbols up to fifth order and their description, taken from reference [Kirkland, 2011].

Symbol	description
C_{10}	Defocus
C_{12}	2-fold astigmatism
C_{21}	Axial coma
C_{23}	3-fold astigmatism
$C_{30}=C_3=C_S$	3rd order spherical
C_{32}	Axial star aberration
C_{34}	4-fold astigmatism
C_{41}	4th order axial coma
C_{43}	3-lobe aberration
C_{45}	5-fold astigmatism
$C_{50}=C_5=C_{S5}$	5th order spherical
C_{52}	5th order axial star
C_{54}	5th order rosette
C_{56}	6-fold astigmatism

order spherical aberration, C_5 is the fifth-order spherical aberration, and $\alpha = \lambda g$ with g the spatial frequency in the image. Aberration-corrected instruments use a set of multipole lenses to correct for unavoidable third-order (and possibly higher) spherical aberration of a rotationally symmetric round lens. In this process, new aberrations are introduced and must also be corrected [Kirkland, 2016]. The mathematical expression to calculate the aberrations of the probe forming system can be written in different ways [Krivanek et al., 1999, Sawada et al., 2008, Sheppard, 2004]. Here, we use the notation of Kirkland [Kirkland, 2011] which describes the deviation from the spherical wave in terms of polar angle α and azimuthal angle ϕ as follows

$$\chi(\alpha, \phi) = \frac{2\pi}{\lambda} \sum_{mn} \frac{\alpha^{n+1}}{n+1} [C_{nma} \cos(m\phi) + C_{nmb} \sin(m\phi)] \quad (2.4)$$

where n and m are positive integers or zero. Some of the coefficients, C_{nma} and C_{nmb} , are listed in the table 2.1.

2.3 Specimen model

In electron microscopy, the electron-specimen interaction refers to the interaction between the charged incident electrons with the electrostatic potential (Coulomb potential) of the atoms inside the specimen. The most common approach to computing the electrostatic potential of the specimen ($V(\mathbf{r})$), is by linear superposition of the spherically symmetric electrostatic potentials of each

atom in the specimen [Lobato, 2014].

$$V(\mathbf{r}) = \sum_{j=1} V_j(\mathbf{r} - \mathbf{r}_j), \quad (2.5)$$

where $\mathbf{r} = (x, y, z)$ is the three-dimensional (3D) coordinate vector in the Cartesian plane and j represent the index of the j th atom. This linear superposition would be exact for single atoms separated by a distance that is large as compared to the size of the atom [Kirkland, 2010]. However, the atoms are bounded together, causing their outer valence electrons to be rearranged slightly. The main interaction resulting in high angle scattering is the interaction between the incident electrons and the electrostatic Coulomb potential of the atomic nucleus. Because the nucleus is unaffected by bonding in the solid the high angle scattering should be well represented by the linear superposition of atomic potentials. The bonding in the solid should primarily affect the low angle scattering.

Since we have the total specimen potential, we can move forward to describe the solution of the Schrödinger equation.

2.4 Electron-specimen interaction

After leaving the objective lenses, the electrons interact with the specimen and they can be reflected, transmitted, scattered, or absorbed. There are many possibilities because of the large amount of energy carried by the illumination. In this study, we will focus on the transmitted electrons only, which can be scattered kinematically when the specimen scatters the electron once (i.e., very thin specimens); or dynamically, when the specimen scatters the electrons more than once, during their passage through the specimen. In addition, for the energy range used in electron microscopy, the electron beam is relativistic, and the study of the motion of the electron should be described by the relativistic Dirac's equation, which is difficult to work with. Fujiwara [Fujiwara, 1961], Ferweda et al. [Ferwerda et al., 1986a, Ferwerda et al., 1986b], and Jagannathan et al. [Jagannathan et al., 1989, Jagannathan, 1990] have shown that the non-relativistic Schrödinger equation with the relativistically correct mass and wavelength yields accurate results in the typical energy ranges used in the electron microscope. A mathematical expression is given by [Kirkland, 2010]

$$\frac{-\hbar^2}{2m} \Delta \Psi(\mathbf{r}) - eV(\mathbf{r})\Psi(\mathbf{r}) = E_0\Psi(\mathbf{r}), \quad (2.6)$$

where $\hbar = h/2\pi$ is the Planck's constant divided by 2π , $m = \gamma m_0$ is the relativistic mass of the electron, $e = |e|$ is the magnitude of the electron charge, $V(\mathbf{r})$ is the electrostatic Coulomb potential of the specimen, $E_0 = eV_0$ is the kinetic energy of the incident electrons, and

$$\Delta\Psi(\mathbf{r}) = \left(\frac{\partial^2}{\partial x^2} + \frac{\partial^2}{\partial y^2} + \frac{\partial^2}{\partial z^2} \right) \Psi(\mathbf{r}) \quad (2.7)$$

is the three-dimensional (3D) Laplacian operator. Only elastic processes will be considered so the energy will remain constant. The 3D wave vector \mathbf{k}_0 and the kinetic energy of the incident wave are defined by:

$$k_0^2 = \frac{1}{\lambda^2} \quad (2.8)$$

$$E_0 = \frac{h^2 k_0^2}{2m}. \quad (2.9)$$

where λ is the relativistically corrected electron wavelength. Substitution of equations (2.8) and (2.9) into the non-relativistic Schrödinger equation (2.6) gives

$$\left(\Delta + 4\pi^2 k_0^2 + \frac{2me}{\hbar^2} V(\mathbf{r}) \right) \Psi(\mathbf{r}) = 0. \quad (2.10)$$

The theory of dynamical electron diffraction has been studied by many authors over a large portion of this century. All these methods solve the differential equation (2.10) under certain approximations.

The high energy Schrödinger equation

In electron microscopy, the kinetic energy of the incident electrons is large as compared to the additional energy the electrons gain and/or lose inside the specimen. The electron motion will be predominantly in the forward direction along the optical-axis (corresponding to the z -axis) and the specimen might be considered as a small perturbation on the electron's motion. Therefore, it is convenient to represent the electron wave function as a modulated plane wave [Kirkland, 2010, Lobato, 2014]

$$\Psi(\mathbf{r}) = \psi(\mathbf{r}) \exp(2\pi i \mathbf{k}_0 \cdot \mathbf{r}). \quad (2.11)$$

Substitution of equation (2.11) into equation (2.10) requires the calculation of $\Delta\Psi$, which can be obtained using the following Laplacian identity

$$\Delta(fg) = f(\Delta g) + 2(\nabla f) \cdot (\nabla g) + g(\Delta f) \quad (2.12)$$

where f and g are 3D functions. Applying this identity to equation (2.11) yields

$$\Delta\Psi(\mathbf{r}) = [\Delta\psi(\mathbf{r}) + 4\pi i \mathbf{k}_0 \cdot \nabla\psi(\mathbf{r}) - 4\pi^2 k_0^2 \psi(\mathbf{r})] e^{2\pi i \mathbf{k}_0 \cdot \mathbf{r}}. \quad (2.13)$$

Substitution of the latter equation (2.13) into equation (2.10) gives

$$\left[\Delta\psi(\mathbf{r}) + 4\pi i \mathbf{k}_0 \cdot \nabla\psi(\mathbf{r}) + \frac{2me}{\hbar^2} V(\mathbf{r}) \right] e^{2\pi i \mathbf{k}_0 \cdot \mathbf{r}} = 0. \quad (2.14)$$

Since this must hold for any position \mathbf{r} , it follows

$$\Delta\psi(\mathbf{r}) + 4\pi i \mathbf{k}_0 \cdot \nabla\psi(\mathbf{r}) + \frac{2me}{\hbar^2} V(\mathbf{r}) = 0. \quad (2.15)$$

If we split the 3D Laplacian operator of equation (2.7) and the gradient operator into a components parallel and perpendicular to the optical axis, this can be rewritten as:

$$\Delta\psi(\mathbf{r}) = \left(\Delta_{xy} + \frac{\partial^2}{\partial z^2} \right) \psi(\mathbf{r}), \quad (2.16)$$

$$\nabla\psi(\mathbf{r}) = \left(\nabla_{xy} + \frac{\partial}{\partial z} \right) \psi(\mathbf{r}). \quad (2.17)$$

In this manner, equation (2.15) can be rewritten as:

$$\left[\Delta_{xy} + \frac{\partial^2}{\partial z^2} + 4\pi i \left(k_z \frac{\partial}{\partial z} + \mathbf{k}_{xy} \cdot \nabla_{xy} \right) + \frac{2me}{\hbar^2} V(\mathbf{r}) \right] \psi(\mathbf{r}) = 0. \quad (2.18)$$

This equivalent form of the Schrödinger equation requires knowledge of two boundary conditions for the wave function, both at the entrance ($z = 0$) and exit ($z = \varepsilon$) planes of the specimen foil and it hardly appears to be solved when the crystal is not perfect and simple. Therefore, approximate solutions are to be sought. For high energy electrons, it is generally assumed that the z component of the wave vector k_z is large and the wave function $\psi(\mathbf{r})$ changes slowly with z , which means [Kirkland, 2010, Lobato, 2014]

$$\left| \frac{\partial^2 \psi}{\partial z^2} \right| \ll \left| 4\pi i k_z \frac{\partial \psi}{\partial z} \right|. \quad (2.19)$$

Using this assumption, equation (2.18) may be approximated as:

$$\left[4\pi i k_z \frac{\partial}{\partial z} + \Delta_{xy} + 4\pi i \mathbf{k}_{xy} \cdot \nabla_{xy} + \frac{2me}{\hbar^2} V(\mathbf{r}) \right] \psi(\mathbf{r}) = 0. \quad (2.20)$$

Ignoring the term of the second derivative with respect to the z -axis corresponds to neglecting the backscattered electrons, which is appropriate for high energy electrons. This approximation is probably better known as the paraxial approximation of the Schrödinger equation [Kirkland, 2010]. The error introduced by neglecting the second order derivative term, consists of two parts: the first one arises from the omission of backscattered electrons, which is shown to be negligible [Van Dyck, 1975]. The second part is due to a slight modification of the wave vector of the transmitted electrons, which becomes important for highly dynamical diffraction in thicker crystals. As a consequence of the latter effect,

the approximation is only valid for crystal thicknesses not exceeding a few tens of nanometres [Lobato, 2014].

Equation (2.20) may be written as a first order differential equation in z as

$$\frac{\partial}{\partial z}\psi(\mathbf{r}) = \left[\frac{i}{4\pi k_z}\Delta_{xy} - \frac{\mathbf{k}_{xy}}{k_z}\cdot\nabla_{xy} + \frac{k_0}{k_z}i\sigma V(\mathbf{r}) \right]\psi(\mathbf{r}). \quad (2.21)$$

When considering parallel illumination only $\mathbf{k}_{xy} = 0$, this reduces to

$$\frac{\partial}{\partial z}\psi(\mathbf{r}) = \left[\frac{i\lambda}{4\pi}\Delta_{xy} + i\sigma V(\mathbf{r}) \right]\psi(\mathbf{r}), \quad (2.22)$$

where $\psi(\mathbf{r})$ is defined by equation (2.11), λ is the relativistic electron wavelength and $\sigma = 2\pi m e \lambda / h^2$ is the interaction parameter. Equation (2.22) has the same form as the time-dependent Schrödinger equation in a 2D space, where the depth z plays the role of the time. The two most popular approaches for the numerical calculation of this equation are the Bloch wave method [Bethe, 1928] and the multislice method [Cowley and Moodie, 1957]. In this thesis, simulations are performed using the multislice approach only.

2.5 Multislice method

The multislice (MS) method developed by Cowley and Moodie [Cowley and Moodie, 1957], and later performed for fast computation by Ishizuka [Ishizuka and Uyeda, 1977] and Rez [Rez, 1985] is one of the most efficient methods to solve the non-relativistic Schrödinger equation (2.22). In this method, the specimen potential is divided into many slices along the electron-beam propagation as is shown in figure 2.2. Each slice has to be thin enough to be considered as a weak phase object, which modifies only the phase of the incident wave. The potential between two consecutive slices is considered to be zero and the propagation of the electron wave within the slice is approximated by the Fresnel propagator, which involves a convolution in real space. The electron wave at any depth z can be calculated by a repeated application of this process. A detailed explanation can be found in [Kirkland, 2010, Ishizuka, 2002]. The mathematical expression for the MS method is given by [Kirkland, 2010]

$$\psi(\mathbf{R}, z + \varepsilon) = P(\mathbf{R}, \varepsilon) \otimes [T(\mathbf{R}, \varepsilon)\psi(\mathbf{R}, z)] + \mathcal{O}(\varepsilon^2) \quad (2.23)$$

where ε is the distance between the slices,

$$P(\mathbf{R}, \varepsilon) = \exp\left(\frac{i\varepsilon}{4\pi k_0}\nabla_{xy}^2\right) = \frac{1}{i\lambda\varepsilon}\exp\left(\frac{i\pi}{\lambda\varepsilon}(x^2 + y^2)\right) \quad (2.24)$$

is the Fresnel propagator

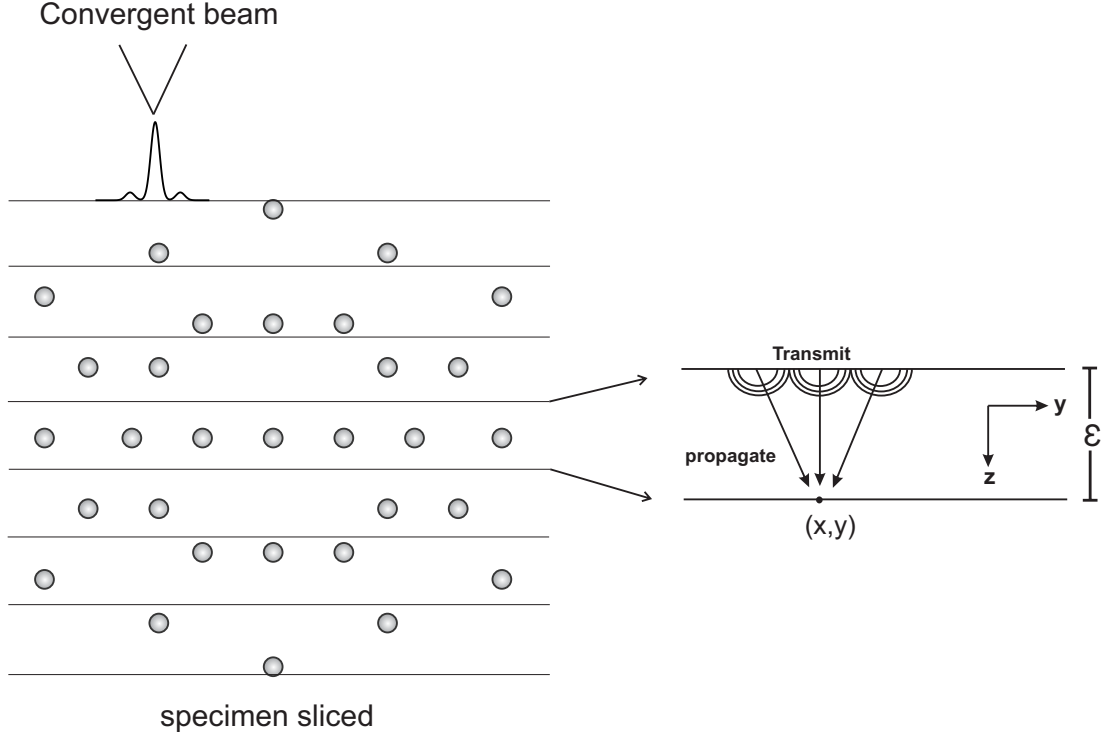


Figure 2.2: Schematic representation of the MS decomposition of a thick specimen and the propagation of electrons between two slices.

$$T(\mathbf{R}, \varepsilon) = \exp \left(i\sigma \int_z^{z+\varepsilon} V(\mathbf{R}, z') dz' \right), \quad (2.25)$$

is the transmission function for the corresponding slice with $\sigma = 2\pi m\lambda/h^2$ the interaction parameter. The operator convolution (\otimes) is defined as

$$f(\mathbf{r}) \otimes g(\mathbf{r}) = \int f(\mathbf{r}') g(\mathbf{r} - \mathbf{r}') d\mathbf{r}'. \quad (2.26)$$

For the full calculation, equation (2.23) has to be repeated for each slice thickness as follows. First, the slices in the specimen along the z -axis are labelled $n = 0, 1, \dots, N$, the depth in the specimen is z_n ($z_n = n\varepsilon$, assuming all the slices with the same thickness). Then, the wave function at the entrance of each slice is labelled $\psi_n(\mathbf{R})$, the propagator and the transmission function are labelled as $P_n(\mathbf{R}, \varepsilon_n)$ and $T_n(\mathbf{R})$, respectively. Therefore, the multislice equation (2.23) can be written in compact form as:

$$\psi_{n+1}(\mathbf{R}, z) = P_n(\mathbf{R}, \varepsilon_n) \otimes [T_n(\mathbf{R}, \varepsilon) \psi_n(\mathbf{R}, z)] + \mathcal{O}(\varepsilon^2). \quad (2.27)$$

In TEM/STEM experiments, both the microscope and the specimen are subject to fluctuations during the recording process. Therefore, the correct way to

describe and simulate these effects is by a repetitive calculation of the formed images for different states of the microscope and specimen [Van Dyck, 2011]. In most of the sophisticated simulation programs, the microscope fluctuations are carried out correctly, but the specimen fluctuations are still approximate. The fluctuation of the specimen can be described by the theory of the thermal vibrations, which will be the subject of the following section.

2.6 Thermal vibration

So far, we have treated the specimen as being static and rigid with the atoms located at their ideal positions. In a real specimen, the atoms are in constant vibration. There are two main reasons for this vibration [Zuo and Spence, 2016]. One is due to the quantum mechanics, where the uncertainty principle dictates that atoms must deviate from its equilibrium position in order to have a finite kinetic energy. The second reason is due to the thermal excitation. The thermal energy is stored in atomic motion. Atoms are bound together through attractive and repulsive forces.

In electron microscopy, most of the experiments are carried out at room temperature around 300 K (there are also experiments that use a heating or cooling system). Around this temperature, the atomic vibrations are very small compared with the interatomic distance. However, due to this vibration, the atoms are displaced from their ideal positions. These displacements produce effects in both the diffraction pattern and the electron microscopy images. The thermal vibration of the atoms in the specimen produces a low-intensity, diffuse background between the normal diffraction peaks. This background intensity will be referred to as thermal diffuse scattering or simply TDS [Kirkland, 2010]. The TDS signal plays an important role in high angular annular dark field (HAADF) STEM, where the largest part of the signal originates from the TDS.

To include this diffuse background intensity in the simulation, there are two useful approaches: the frozen phonon and the absorptive potential approximation.

2.6.1 Frozen phonon

The frozen phonon (FP) approach has been introduced to include the thermal vibrations in MS calculations of convergent-beam electron diffraction (CBED) patterns. This method produces a thermal diffuse background, Kikuchi bands and Debye-Waller factor, all of which are neglected in the standard MS calculation [Loane et al., 1991]. The FP describes the TDS in STEM and HRTEM very accurately [Muller et al., 2001, Wang, 1998], especially in HAADF STEM where the largest part of the signal in the annular dark field detector originates

from phonon scattering [Van Dyck, 2009, Nellist and Pennycook, 1999]. This model has been proved in a rigorous way that is fully equivalent to a full quantum mechanical treatment of the inelastic phonon scattering model [Van Dyck, 2009], and has been demonstrated good accuracy with the experiment even in the cases of thicker specimens [LeBeau et al., 2008], and specimens containing heavy atomic number [LeBeau and Stemmer, 2008]. This method is based on a classical description in which each electron sees a different configuration of atoms displaced from their mean positions. The resulting image intensity is obtained by averaging the simulated images performed for enough configurations. The displacement of the atoms due to the vibration of the crystal can be calculated by molecular dynamics, DFT calculations, or by using the approximated Einstein model in which the displacement is calculated for each atom independently (uncorrelated model).

In a general approach, the total specimen potential $V(\mathbf{r},t)$ and the electron wave $\psi(\mathbf{r},t)$ can be written as a sum of the time-independent and time-dependent components [Takagi, 1958, Van Dyck, 2009]

$$V(\mathbf{r},t) = \langle V(\mathbf{r}) \rangle_t + W(\mathbf{r},t) \quad (2.28)$$

$$\psi(\mathbf{r},t) = \langle \psi(\mathbf{r}) \rangle_t + \delta(\mathbf{r},t) \quad (2.29)$$

where $\langle \rangle_t$ is the average taken over the time t . From the latter equations (2.28) and (2.29), it follows

$$\langle W(t) \rangle_t = 0, \quad (2.30)$$

$$\langle \delta(\mathbf{r},t) \rangle_t = 0. \quad (2.31)$$

Following these premises, Van Dyck [Van Dyck, 2009] has shown that the frozen phonon model allows us to split the total intensity into two contributions: the coherent and incoherent intensity. By squaring Eq. (2.29) and using Eq. (2.31), the total intensity in the Fourier/Real space can be written as

$$\langle |\psi(\mathbf{g}/\mathbf{r},t)|^2 \rangle = |\langle \psi(\mathbf{g}/\mathbf{r}) \rangle|^2 + \langle |\delta(\mathbf{g}/\mathbf{r},t)|^2 \rangle \quad (2.32)$$

where the first term on the right-hand side corresponds to the coherent intensity (i.e. elastic scattering) and the second term to the incoherent intensity (i.e. inelastic scattering). Furthermore, \mathbf{g} and \mathbf{r} are vectors in the reciprocal and real space, respectively. The total intensity can be calculated by averaging the intensity over different configurations. In addition, the coherent intensity results from averaging the wave function of different configurations and then square it up. Finally, the incoherent intensity is calculated by subtracting the coherent intensity from the total intensity.

2.6.2 Absorptive Potential

One of the most accurate and successful approaches to include the TDS is the FP approach. However, computation of the image intensity for a large number of configurations (100 - 500 configurations) [Rosenauer et al., 2008] requires an enormous amount of computing power and is time-consuming. Especially in the calculation of STEM images where the whole MS calculation has to be repeated several times for each probe position (one probe-position corresponds to one pixel in the STEM image). In order to reduce the amount of calculations, the MS method with an absorptive potential method has been proposed [Pennycook and Jesson, 1991, Ishizuka, 2002, Allen et al., 2003, Croitoru et al., 2006, Rosenauer et al., 2008], which is based on the concept that the intensity produced by the TDS could be explained by including absorption in the dynamical equations of the electron diffraction by using a complex lattice potential. This concept, first introduced by Moliere [Molière, 1939] and later justified by Yoshioka [Yoshioka, 1957] with a general quantum-mechanical treatment is less intensive than the FP approach and it has shown to be in good agreement with a full FP calculations up to a thickness of 25 nm for SrTiO₃ along the [100] zone-axis [LeBeau et al., 2008].

For the calculation of this method, we followed Ishizuka [Ishizuka, 2002] and Rosenauer [Rosenauer et al., 2008] in which the absorptive potential approximation computed from e.g. Weickenmeier and Kohl parametrization [Weickenmeier and Kohl, 1991] is treated as a quasi-coherent approach, where, the distribution of the atomic displacements due to the thermal vibration, is described by the convolution of the atomic scattering factors with a Gaussian function. Then, the elastic electron diffraction is calculated by using the modified potentials. As a result, it reduces efficiently the structure factors due to the deviations from the ideal structure of the specimen.

The main approximation that is made in the absorptive potential method is the assumption that the TDS scattered electrons directly propagate towards the detector, without further interaction with the specimen. This assumption has almost the same result compared with the FP approach for small specimen thicknesses (less than 50 nm thick) and for light atoms [Rosenauer et al., 2008]. In practice, the effect of TDS in the absorptive potential method is implemented within the multislice approach by adding the imaginary component $V_{TDS}(\mathbf{r})$ to the electrostatic Coulomb potential $V_C(\mathbf{r})$ given before by equation (2.5). Under this assumption, the new total potential $V_T(\mathbf{r})$ may then be written as [Ishizuka, 2002, Rosenauer et al., 2008]

$$V_T(\mathbf{r}) = V_C(\mathbf{r}) + iV_{TDS}(\mathbf{r}). \quad (2.33)$$

The latter equation describes the total potential in 3D. Following the criterion of the multislice method, the specimen potential has to be divided in many slices along the electron-beam propagation and each slice thickness ε has to be thin enough to be considered as a weak phase object. Under this assumption, the projected potential in each slice can be calculated as

$$V_T(\mathbf{R}, z_n) = V_C(\mathbf{R}, z_n) + iV_{TDS}(\mathbf{R}, z_n), \quad (2.34)$$

where the projected electrostatic and TDS potential are given by

$$V_C(\mathbf{R}, z_n) = \int_{-\infty}^{+\infty} \sum_j V_j(\mathbf{R}_j, z') dz' \quad (2.35)$$

and

$$V_{TDS}(\mathbf{R}, z_n) = FT_{\mathbf{g} \rightarrow \mathbf{R}}^{-1} \left[\frac{\sigma \varepsilon}{\Omega} \sum_j e^{2i\pi \mathbf{g} \cdot \mathbf{R}_j} \int_{detector} f_{\mathbf{S}}^j f_{\mathbf{S}-\mathbf{g}}^j e^{-M_j \mathbf{g}^2} (1 - e^{-2M_j [S^2 - \mathbf{S} \cdot \mathbf{g}]}) d^2 \mathbf{S} \right] \quad (2.36)$$

respectively, with Ω the volume of the slice and σ the interaction constant. The index j refers to a specific atom in the volume Ω , $M_j = 2\pi \langle \mathbf{u}_j^2(t) \rangle$ is the Debye-Waller factor calculated from the atomic displacement vector \mathbf{u}_j , $f_{\mathbf{S}-\mathbf{g}}^j$ is the atomic scattering factor amplitude of atom j with scattering vector \mathbf{q} , and the integration is performed over all the possible scattering vector \mathbf{S} . The Fourier transform \mathcal{F} and the inverse of the Fourier transform $FT_{\mathbf{g} \rightarrow \mathbf{R}}^{-1}$ are given by

$$\mathcal{F}(\mathbf{g}) = \int_{-\infty}^{+\infty} f(\mathbf{R}) e^{-i2\pi \mathbf{g} \cdot \mathbf{R}} d\mathbf{R} \quad (2.37)$$

$$FT_{\mathbf{g} \rightarrow \mathbf{R}}^{-1}[\mathcal{F}(\mathbf{g})] = f(\mathbf{R}) = \int_{-\infty}^{+\infty} \mathcal{F}(\mathbf{g}) e^{i2\pi \mathbf{g} \cdot \mathbf{R}} d\mathbf{g}. \quad (2.38)$$

Following the assumption that each slice acts as a weak phase object, the electron wave can be approximated as

$$\psi(\mathbf{R}, z_n) \approx 1 + i\sigma V_T(\mathbf{R}, z_n). \quad (2.39)$$

It has been demonstrated that using the latter approximation and the TDS-potential $V_{TDS}(\mathbf{R}, z_n)$ of equation (2.36), the TDS intensity in the volume Ω can

be calculated as [Ishizuka, 2002]

$$I_{TDS}^n = \int |\psi(\mathbf{R}, \mathbf{z}_n)|^2 V_{TDS}(\mathbf{R}, \mathbf{z}_n) d^2\mathbf{R} \quad (2.40)$$

where, $n = 1, \dots, N$ counts the number of slices in which the specimen was divided. Therefore, the total intensity is given by the sum of the intensities calculated in all the slices

$$I_{TDS} = \sum_n I_{TDS}^n. \quad (2.41)$$

2.7 Intensity integration over the detector

After the electron wave leaves the specimen, it is diffracted onto the detector plane. This step can be represented by taking a Fourier transform. The intensity of this wave function $|\psi(\mathbf{g}, \mathbf{R}_p)|$ as a function of the scattering angle $\lambda\mathbf{g}$ is the convergent beam electron diffraction (CBED) pattern. The CBED pattern is incoherently integrated over the detector geometry and the result is the final STEM image signal $I(\mathbf{R}_p)$ for one probe position \mathbf{R}_p , given by

$$I(\mathbf{R}_p) = f_{kl} = \int_{detector} |\psi(\mathbf{g}, \mathbf{R}_p)|^2 D(\mathbf{g}) d^2\mathbf{g} \quad (2.42)$$

where $D(\mathbf{g})$ is the detector function.

$$\begin{aligned} D(\mathbf{g}) &= 1 \quad \text{for } g_{D_{min}} \leq g \leq g_{D_{max}} \\ &= 0 \quad \text{otherwise,} \end{aligned} \quad (2.43)$$

where $\lambda g_{D_{min}}$ and $\lambda g_{D_{max}}$ are the inner and outer radius of the annular detector. This calculation was done considering a perfect circular annular detector with homogeneous sensitivity. In real experiments this is not completely true as shown in reference [Martínez, 2014]. The best way to include the sensitivity of the detector is by including a function depending on the sensitivity that can be obtained by mapping the experimental detector [Rosenauer et al., 2009].

In the following chapters, the intensity for each probe position given by equation (2.42) will be referred to as observations and will be denoted as f_{kl} , where, the indexes k and l correspond to the pixel (k, l) of a STEM image of $K \times L$ pixels.

2.8 Simulation programs

The process of the simulated STEM images can be summarized by figure 2.3. In this thesis, the simulations were performed with two programs MULTEM

and STEMSIM. The first one, MULTEM program was used to simulate the STEM images with the inclusion of the frozen phonon (FP) calculations, and the STEMSIM program was used to perform the STEM images with the absorptive potential (AP) calculations. Even when both programs show the same results for simulation with FP calculations, the advantage of MULTEM with respect to STEMSIM is the computation time. Especially when MULTEM uses the graphical processor unit (GPU) instead of the central unit processor (CPU) demonstrating to be more time-efficient for this type of calculations.

2.8.1 MULTEM

The MULTEM program was developed by I. Lobato et al. [Lobato and Van Dyck, 2015] and more recently has been updated by the authors [Lobato et al., 2016] at the University of Antwerp. This program is a powerful tool to perform accurate and fast multislice calculations by combining higher order expansion of the multislice solution of the high energy Schrödinger equation, correct sub-slicing of the 3D potential, top-bottom surfaces and parallel processing. The program allows to perform simulations of several techniques used in electron microscopy such as CTEM, STEM, imaging STEM (ISTEM), energy filtered TEM (EFTEM), STEM electron energy loss spectroscopy (EELS), electron diffraction (ED), precession electron diffraction (PED), CBED, ADF-TEM, and annular bright field hollow cone (ABF-HC). Moreover, the program allows the user to work with or without user-interface. Another relevant advantage of MULTEM is that uses the central processor unit (CPU) or the graphical processor unit (GPU). For multislice calculations, GPUs have a huge advantage with respect to the CPUs in computing time. The MULTEM program is an open source code, and pre-compiled binaries of the program for the different platforms can be found at www.mulTEM.emat.uantwerpen.be.

If more flexibility or non-standard setups are needed, the user can choose to run the C++ MULTEM libraries by calling them from external codes or more conveniently through the use of MATLAB wrappers via the so-called mex interface. If this is the case, the MULTEM's C++ classes, Matlab mex functions and the GUI are available in the GitHub repository <https://github.com/Ivanlh20/MULTEM>. The MULTEM mex file has been compiled and tested for Windows, Ubuntu and Scientific Linux, and Mac-OS. For further and detailed information about the program, see the references [Lobato and Van Dyck, 2015, Lobato et al., 2016].

2.8.2 STEMSIM

The STEMSIM program was developed by A. Rosenauer et al. [Rosenauer and Schowalter, 2008] at the University of Bremen. This program has a very user friendly interface that allows us to see the progress of the simulations (STEM

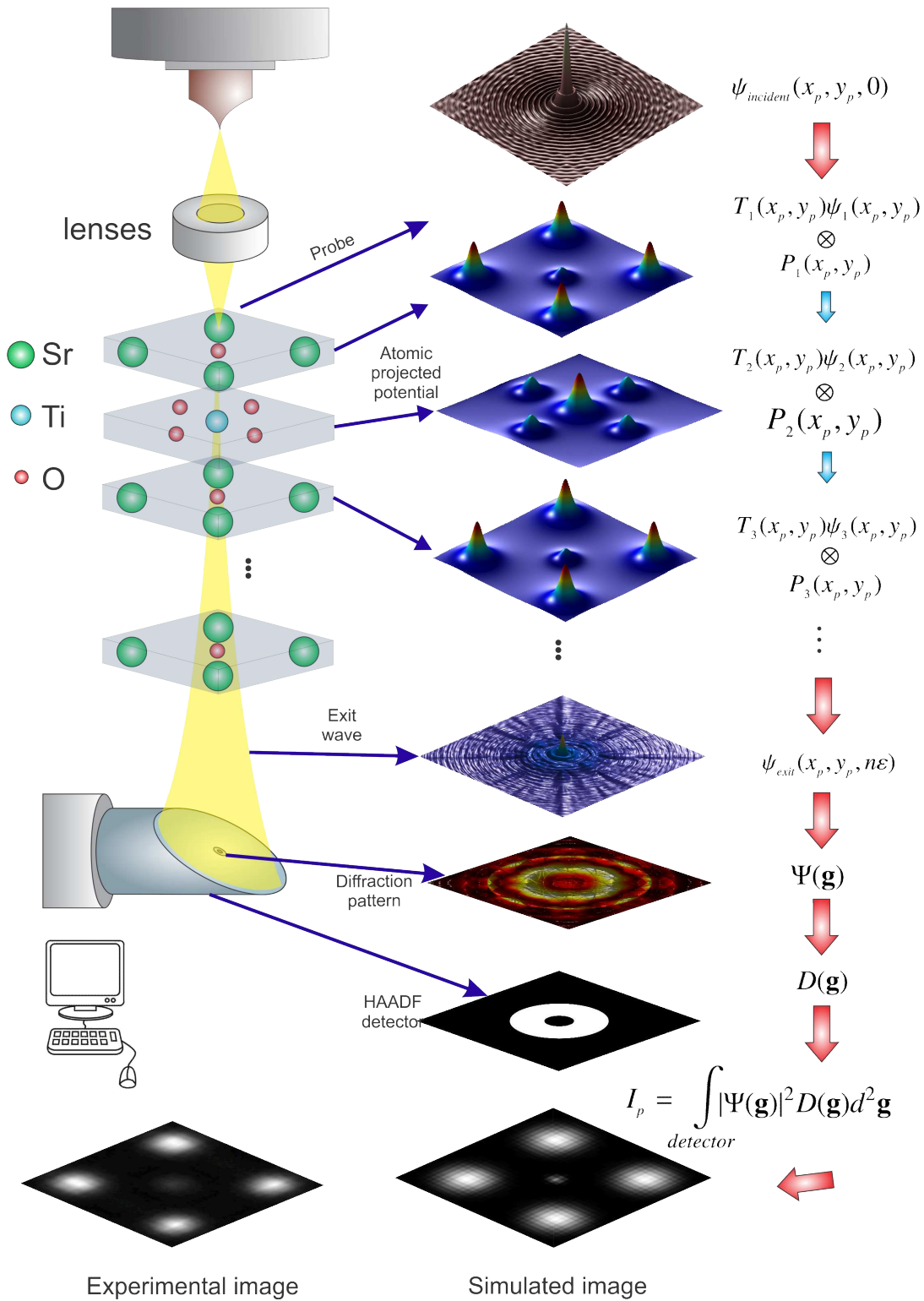


Figure 2.3: Schematic of STEM imaging simulation process.

simulations). The program is developed in Matlab, and can be installed in operative systems such as Linux or Windows. STEMSIM allows us to perform simulation by using "the Bloch wave method" or the multislice method. In the multislice method, the TDS calculation can be done by using full frozen phonon calculations, the absorptive potential model [Rosenauer and Schowalter, 2008] or the emission potential method [Rosenauer et al., 2008]. The emission potential method is an alternative method that reduces the number of calculations used for the frozen phonon to calculate the TDS signal. This approximation is based on the absorptive potential model. Also, this program enables us to perform simulations of CTEM, STEM, and EELS and can be easily implemented to simulate other technique of electron microscopy. Otherwise, the program can be used on a single desktop or can be installed on a cluster with multiple CPUs.

2.9 Conclusions

In this chapter, the physics of the STEM image formation has been explained. First, the mathematical derivation was given by solving the high energy Schrödinger equation of the electron-specimen interaction with the usual approximations, which have been proven to work for the energy range used in electron microscopy. Then, the numerical solution of this equation was performed by the multislice method, which is considered as one of the most efficient methods. Finally, the diffuse scattering produced due to the atomic vibration of the specimen was included in the calculation by using two different approaches: a) the so-called *frozen phonon* model and b) the *absorptive potential* approximation method.

In the next chapter, the simulated STEM images will be used to model the intensity observations. From this parametric model, an expression for the so-called Cramér-Rao lower bound (CRLB) will be derived. The CRLB is a lower bound on the variance with which unknown structure parameters can be estimated.

Chapter 3

Statistical parameter estimation theory

3.1 Introduction

In this chapter, the basic principles of statistical parameter estimation theory will be introduced. These principles have been applied in many scientific fields such as biology, chemistry, physics, image processing, computer vision, and astronomy. In general, parameter estimation is used as a statistical tool to determine, or more correctly, to estimate, unknown physical quantities or parameters on the basis of observations that are acquired experimentally [van den Bos, 2007]. In most of these experiments, a complete understanding of their physical processes is needed in order to simulate the behaviour of each parameter. These processes often can be described by mathematical models, which are usually solved by numerical methods [Bock et al., 2013]. However, in most of these cases, the observations, given by the solution of their models are not always the quantities to be measured but are related to them. Therefore, the use of estimators is needed in order to quantify the unknown parameters.

For scanning transmission electron microscope (STEM) experiments, the physical process of the electron-specimen interaction can be modelled by the differential Schrödinger equation explained in chapter 2. The solution of this equation is given by the numerical multislice (MS) method, where the frozen phonon (FP) or absorptive potential (AP) models have to be included in order to calculate the thermal diffuse scattering intensity. To obtain realistic model output results, the experimental conditions such as detector geometry [Hillyard and Silcox, 1995], detector sensitivity [MacArthur et al., 2014], specimen orientation [Klenov et al., 2007], specimen tilt [Maccagnano-Zacher et al., 2008], the effect of an amorphous layer [Mkhoyan et al., 2008], strain effects [Grillo, 2009], and source size broadening [Verbeeck et al., 2012] have to be included in the simulations. Taken into account all of these considerations and using the FP or

AP within the MS method, simulations of the specimen under various conditions of the electron microscope can be performed. The output of these simulations can be used to determine the unknown parameters by fitting this model to the experimental data. In this manner, the unknown parameters can be estimated by minimizing the residuals between the experimental data and the simulation results. It is well known that the experimental data are always subject to experimental fluctuations. As a result of these fluctuations, the precision with which the unknown parameters can be measured is limited.

In materials science, one of the central issues is to understand the relation between the structure and its properties of a given material [Van Tendeloo et al., 2012]. This requires both theoretical and experimental studies [Spence, 1999, Muller and Mills, 1999, Springborg, 2000]. From this point of view, understanding means matching observations with ab-initio calculations. Since all structure-property relations are encoded in the positions of the atoms [Carter and Williams, 2016], the precision with which the atomic arrangement of individual atoms is measured from the experiment becomes very important. As mentioned in chapter 1, extremely small changes in their local structure of the specimen may result in significant changes of their properties. Especially in nanoclusters, a very small displacement of a single atom can change their properties. A precision in the sub-picometre range is needed for the atom positions [Muller and Mills, 1999, Kisielowski et al., 2001]. This explains the growing interest in developing quantitative analysis tools in order to obtain a precise determination of the atomic arrangement.

In this thesis, the observations will be defined by a set of pixel values of the images acquired using STEM. The experimental STEM images fluctuate randomly about their expectation values due to the presence of noise. An effective way to describe this behaviour is by modelling the observations as stochastic variables. By definition, a set of stochastic variables is characterized by the joint probability density function which defines the expectation values of the observations and the fluctuations of the observations about the expectation values. The expectation values are described by the expectation model, i.e. a parametric model containing the unknown structure parameters. If the joint probability density function is known, the Fisher information matrix can be defined for the parameters that are continuous in their domain. Based on the concept of the Fisher information matrix, an expression for the Cramér-Rao lower bound (CRLB) can be derived. The CRLB corresponds to the lower bound on the variance of the parameters and is independent of the estimation method used to calculate the unknown parameters. This lower bound therefore represents the intrinsic limit to the precision. Using the CRLB in the following chapters, we investigate how precise a) an atomic column can ultimately be located from a two-dimensional (2D) high angle annular dark field (HAADF) STEM images, b) atoms of a nan-

ocluster can ultimately be located in three-dimensions (3D) from a tilt series of images acquired using annular dark field (ADF) STEM, c) the depth of atoms of an isolated column and the depth of the centre of mass of an isolated atomic column can ultimately be located from a focal series of images acquired with HAADF STEM.

This chapter is organized as follows. In section 3.2, parametric models for the intensity observations and the image recording are described. In section 3.3, the statistical measurement precision is quantified using the CRLB. In section 3.4, the precision and experimental design is explained. In section 3.5, the maximum likelihood estimation method is described. Finally, in section 3.6, conclusions will be drawn.

3.2 Parametric model for the intensity observations

In this section, a parametric model for the observations will be introduced. Specifically, this will be used to model STEM observations. This parametric model describes the expectations of the intensities observed when STEM images are recorded and will be used to derive an expression to calculate the attainable precision. Such a model can be derived using the solution of the dynamic equation of the electron-specimen interaction process and a description of the imaging process. For the purpose of this thesis, the multislice solution explained in chapter 2 will be used, but instead, also the Bloch wave or the channelling approximation method can be used as well.

The image recording and electron dose

As mentioned in chapter 1.3, in ADF STEM imaging, a focused electron probe is scanned across the sample in a raster fashion and the transmitted electrons are collected by an annular detector placed in the back focal plane. The image is thus recorded as a function of the probe position (x_k, y_l) . Therefore, the position of the probe directly corresponds to an image pixel at the same position. The recording device consists of $K \times L$ equidistant pixels of area $\Delta x \times \Delta y$, where Δx and Δy are the probe sampling distances in the x and y direction, respectively. This means that pixel (k, l) corresponds to position $(x_k, y_l) \equiv (x_1 + (k - 1)\Delta x, y_1 + (l - 1)\Delta y)$ with $k = 1, \dots, K$ and $l = 1, \dots, L$ and (x_1, y_1) represents the position of the pixel at the bottom left corner of the field of view. The number of incident electrons per probe position N_p is given by the following expression:

$$N_p = \frac{I\tau}{e} \quad (3.1)$$

with $e = 1.6 \times 10^{-19}$ C the electron charge. The recording time τ (dwell time) for one image point (pixel), correspond to the ratio of the frame time t divided by the number of pixels $K \times L$ of the whole image (field of view):

$$\tau = \frac{t}{KL}. \quad (3.2)$$

The probe current is given by [Barth and Kruit, 1996]

$$I = \frac{B_r E_0 \pi^2 d_{I50}^2 \alpha_0^2}{4e} \quad (3.3)$$

with B_r being the reduced brightness of the source, E_0 the beam energy, d_{I50} the diameter of the source image containing 50% of the current, α_0 the objective aperture semi-angle, and

$$d_{I50} = 2\sqrt{-2\ln 0.5} s. \quad (3.4)$$

As a consequence of the detector shape and size in STEM, only the electrons within a selected part of the CBED pattern are used to produce the image. The expected number of detected electrons per pixel position (k,l) equals

$$\lambda_{kl} = f_{kl} \frac{I\tau}{e} \quad (3.5)$$

with f_{kl} ($f_{kl} < 1$) the fraction of electrons expected to be recorded by the detector [Van Aert et al., 2009], i.e. f_{kl} is the intensity value at the pixel (k,l) and depends on the experimental STEM settings and the unknown structure parameters. The STEM settings enter to the calculations via equation (2.1), and the specimen parameters such as the atom type and atomic positions enter via equation (2.5). Notice that in this study the atomic positions will be considered as unknown parameters. Finally, f_{kl} is calculated using equation (2.42).

3.3 Statistical measurement precision

In the preceding subsection, the parametric model for the intensity observations has been described. This model describes the expected number of electrons arriving at the STEM detector and is parametric in their locations β of all atoms constituting the specimen. In what follows, it will be shown how these location parameters enter the probability density function of the statistical observations. From this parametrized probability density function, the so-called CRLB may be computed [van den Bos, 2007, van den Bos and den Dekker, 2001], which is a lower bound on the variance of the parameters. It is important to mention that this lower bound is independent of the estimation method used to estimate the unknown parameters (e.g. estimation of all the individual positions of the atoms in 3D). For the purpose of this thesis, the most important parameters are the 3D positions of the atoms. Therefore, an expression for the CRLB

on the variance of the positions will be derived in subsection 3.3.2 based on the joint probability density function of the observations derived in subsection 3.3.1.

3.3.1 The joint probability density function of the observations

In any STEM experiment, sets of observations made under the same conditions differ from experiment to experiment. These fluctuations have to be specified, which is the subject of this section. The usual way to describe this behaviour is to model the observations as stochastic variables. Stochastic variables are defined by probability density functions [van den Bos and den Dekker, 2001]. In a STEM experiment the observations are electron counting results. The fluctuations of these observations are denoted as electron counting noise, Poisson noise, or shot noise. The corresponding probability density function can be modelled as a Poisson distribution. Consider a set of stochastic observations w_{kl} , $k = 1, \dots, K$, and $l = 1, \dots, L$. Then the vector \boldsymbol{w} defined as

$$\boldsymbol{w} = (w_{11}, \dots, w_{KL})^T \quad (3.6)$$

represents the column vector of these observations of dimension $K \times L$, where $K \times L$ corresponds to the dimension of the 2D image. The observations are assumed to be statistically independent and have a Poisson distribution. Therefore, the probability that the observation w_{kl} is equal to ω_{kl} is given by [Mood et al., 1974]

$$\frac{(\lambda_{kl})^{\omega_{kl}}}{\omega_{kl}!} \exp(-\lambda_{kl}) \quad (3.7)$$

where λ_{kl} is the expected number of detected electrons at pixel (k, l) for which an expression is given by equation (3.5). Since the observations are assumed to be statistically independent, the probability $P(\boldsymbol{\omega}, \boldsymbol{\beta})$ that a set of observations is equal to $\boldsymbol{\omega} = (\omega_{11}, \dots, \omega_{KL})^T$ is the product of all the probabilities described by equation (3.7):

$$P(\boldsymbol{\omega}, \boldsymbol{\beta}) = \prod_{k=1}^K \prod_{l=1}^L \frac{(\lambda_{kl})^{\omega_{kl}}}{\omega_{kl}!} \exp(-\lambda_{kl}). \quad (3.8)$$

This is called the joint probability density function of the observations. Note that the location parameter $\boldsymbol{\beta}$ enter $P(\boldsymbol{\omega}; \boldsymbol{\beta})$ via the expression for λ_{kl} , given by equation (3.5). Indeed from section 3.2, it follows that in order to compute the expected number of detected electrons, use is made of the approximation method calculations, which require the atomic positions in the specimen as an input. In the following subsection, it will be shown how this expression for the joint probability density function can be used in order to compute the CRLB.

3.3.2 The Cramér-Rao lower bound

In this subsection, the CRLB is discussed. By definition, the CRLB is a theoretical lower bound on the variance of any unbiased estimator. Therefore, this expression can be used in order to determine the *attainable precision* with which the location parameters of all atoms present in a nanocluster can be estimated. Suppose that in electron tomography, we want to measure the 3D position parameters $\boldsymbol{\beta} = (\beta_{x1}, \beta_{y1}, \beta_{z1}, \dots, \beta_{xN}, \beta_{yN}, \beta_{zN})$ of a set of N atoms of a nanocluster quantitatively from a set of projection images acquired using HAADF STEM. For this purpose, one can use many estimators (e.g. least squares, least absolute values or maximum likelihood estimators). An estimator is a function of the observations that is used to compute the parameters. In this context, an estimator can be a tomographic reconstruction algorithm. The precision of an estimator is represented by the variance or by its square root, the standard deviation. Generally, different estimators will have different precisions. It can be shown, however, that the variance of unbiased estimators will never be lower than the CRLB, which is independent of the used estimation method. Fortunately, there exists a class of estimators (including the maximum likelihood estimator) that achieves this bound at least asymptotically, that is, for the number of observations going to infinity. For details of this lower bound we refer to [van den Bos and den Dekker, 2001, van den Bos, 2007].

3.3.2.1 Fisher information matrix

The CRLB follows from the concept of the Fisher information. The Fisher information matrix $F_{\boldsymbol{\beta}}$ for estimation of the position parameters of a set of N atoms $\boldsymbol{\beta} = (\beta_{x1}, \beta_{y1}, \beta_{z1}, \dots, \beta_{xN}, \beta_{yN}, \beta_{zN}) = (\beta_1, \dots, \beta_{3N})^T$ is defined as

$$F_{\boldsymbol{\beta}} = -\mathbb{E} \left[\frac{\partial^2 \ln P(\boldsymbol{\omega}; \boldsymbol{\beta})}{\partial \boldsymbol{\beta} \partial \boldsymbol{\beta}^T} \right] \quad (3.9)$$

where $\mathbb{E}[\cdot]$ is the expectation and $P(\boldsymbol{\omega}; \boldsymbol{\beta})$ is the joint probability density function of the observations described by equation (3.8) and

$$\frac{\partial^2 \ln P(\boldsymbol{\omega}; \boldsymbol{\beta})}{\partial \boldsymbol{\beta} \partial \boldsymbol{\beta}^T} \quad (3.10)$$

is the $3N \times 3N$ Hessian matrix of $\ln P(\boldsymbol{\omega}; \boldsymbol{\beta})$ defined by its (p, q) th element

$$\frac{\partial^2 \ln P(\boldsymbol{\omega}; \boldsymbol{\beta})}{\partial \beta_p \partial \beta_q} \quad (3.11)$$

where β_p and β_q correspond to the p and q th element of the vector $\boldsymbol{\beta}$, respectively.

3.3.2.2 Cramér-Rao inequality

Suppose that $\hat{\boldsymbol{\beta}} = (\hat{\beta}_{x1}, \hat{\beta}_{y1}, \hat{\beta}_{z1}, \dots, \hat{\beta}_{xN}, \hat{\beta}_{yN}, \hat{\beta}_{zN})^T$ is an unbiased estimator of $\boldsymbol{\beta}$. The Cramér-Rao inequality then states that [Kendall and Stuart, 1967]

$$\text{cov}(\hat{\boldsymbol{\beta}}, \hat{\boldsymbol{\beta}}) \geq F^{-1} \quad (3.12)$$

where $\text{cov}(\hat{\boldsymbol{\beta}}, \hat{\boldsymbol{\beta}})$ is the $3N \times 3N$ variance-covariance matrix of the estimator $\hat{\boldsymbol{\beta}}$, defined by its (p, q) th element $\text{cov}(\hat{\beta}_p, \hat{\beta}_q)$. Its diagonal elements are thus the variances of the elements of $\hat{\boldsymbol{\beta}}$. The matrix F^{-1} is called the Cramér-Rao lower bound on the variance of $\hat{\boldsymbol{\beta}}$. The Cramér-Rao inequality (3.12) expresses that the difference between the left-hand and right-hand member is positive semi-definite. A property of a positive semi-definite matrix is that its diagonal elements cannot be negative. This means that the diagonal elements of $\text{cov}(\hat{\boldsymbol{\beta}}, \hat{\boldsymbol{\beta}})$ will always be larger than or equal to the corresponding diagonal elements of the inverse of the Fisher information matrix. Therefore, the diagonal elements of F^{-1} define lower bounds on the variances of the elements of $\hat{\boldsymbol{\beta}}$

$$\text{var}(\hat{\beta}_p) \geq F^{-1}(p, p) \quad (3.13)$$

where $p = 1, \dots, 3N$ and $F^{-1}(p, p)$ is the (p, p) th element of the inverse of the Fisher information matrix. The elements $F(p, q)$ may be calculated explicitly using equations (3.5)-(3.11) [Van Aert et al., 2002b]:

$$F(p, q) = \sum_{k=1}^K \sum_{l=1}^L \frac{1}{\lambda_{kl}} \frac{\partial \lambda_{kl}}{\partial \beta_p} \frac{\partial \lambda_{kl}}{\partial \beta_q}. \quad (3.14)$$

Equation (3.14) is derived from the definition of the Fisher information given by equation (3.9) using the knowledge of the joint probability density function of the observations. This joint probability density function and the expectation values of the observations are the only requirements to be able to compute the ultimate precision for locating the atoms in 3D. The derivative of λ_{kl} with respect to $\boldsymbol{\beta}$ in equation (3.14) may be calculated from the parametric model of the intensity observations described in section 3.2.

For the multislice simulations, the derivatives cannot be computed analytically, since this is a numerical solution of the high energy Schrödinger equation. In order to calculate the partial derivatives for the multislice method, an additional set of multislice simulation is required in which one of the unknown parameters has to be shifted. For example, if we want to calculate the derivative of the central atom shown in figure 3.1 with respect to the x -coordinate, the central atom has to be displaced along the x -axis. Then, the partial derivative is approximated using the finite difference quotient:

$$\lambda'(x) = \frac{\lambda(x) - \lambda(x - h)}{h} \quad (3.15)$$

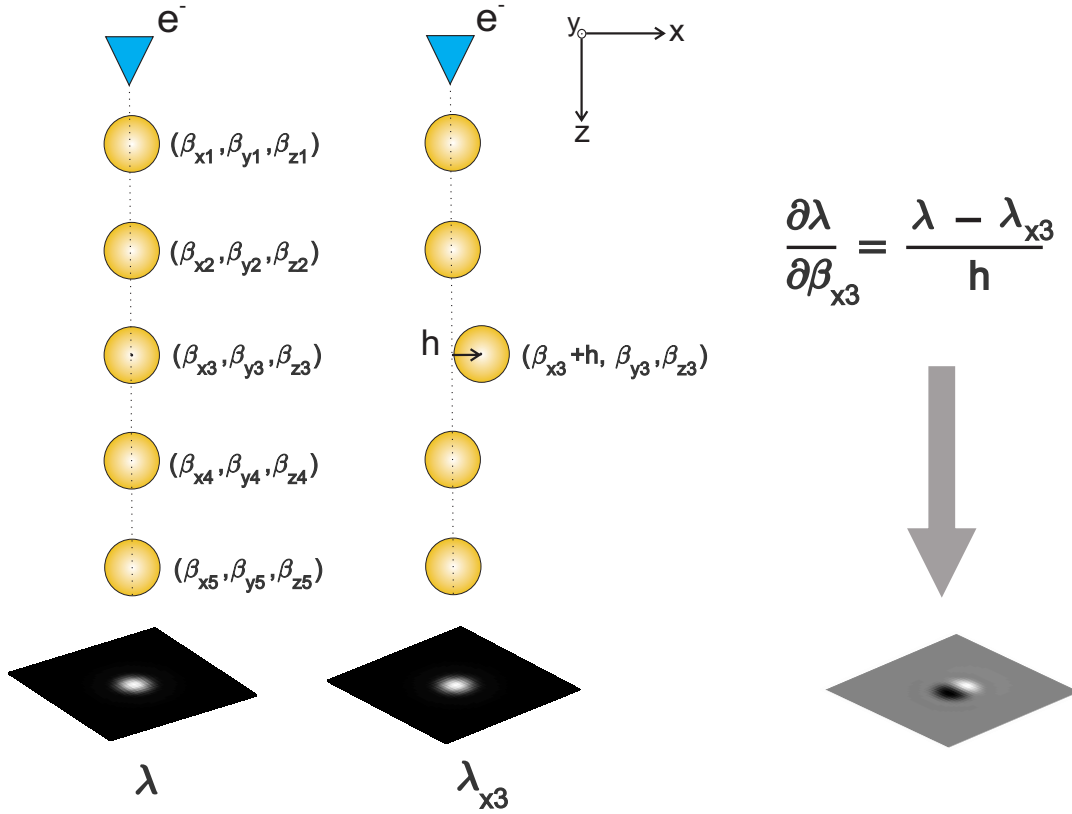


Figure 3.1: Example demonstrating how the numerical derivative of a STEM image with respect to the x -axis of the central atom can be computed.

where h denotes the shift of the atom. Similarly, the derivatives with respect to the y - and z -axis, for the other atoms, and for the different projected images of a tilt series or focal series can be calculated.

3.4 Precision and experimental design

One of the main objectives of STEM experiments is to fully characterize the specimen under study. This means that all the structural parameters and the chemical composition have to be measured as precisely as possible. To achieve this objective, STEM experiments should be set up in such a way that the data obtained can be analysed to yield most information concerning the structure and chemistry of the specimen. Therefore, when the estimators such as the maximum likelihood are applied to estimate these parameters, one aims to estimate them as precisely as possible.

Following the concept of the CRLB explained in section 3.3.2, the quantitative STEM experiment can be optimized in terms of the *attainable precision* of un-

known structure parameters [den Dekker et al., 1999, Van Aert et al., 2002b]. For example, according to [Van Aert et al., 2002b], the optimal experimental design to estimate the atomic column position in a 2D image acquired with STEM, can be performed as follows: a) minimizing a scalar measure σ_{CR}^2 of the CRLB as a function of the microscope parameters, b) selecting the microscope parameters, because some of them are tunable, while others are fixed, c) evaluating the dependence of the CRLB on the parameters, d) interpreting and comparing the results with the design that is assumed to be optimal.

The same procedure can be followed for others STEM experiments such as electron tomography or depth sectioning. In these cases, the election of the unknown parameter to minimize the measurement of the CRLB will be different. In chapter 5, the optimal experimental design to estimate the individual atomic positions of a gold nanocluster from a set of tilt-series images acquired using ADF STEM will be discussed. In chapter 6, the CRLB will be used to measure the depth of the centre of mass of the atomic column from a set of focal-series images acquired with HAADF STEM. Combined with the atom counting method, a STEM experiment is designed to obtain the individual 3D atomic position of a gold nanorod.

3.5 Maximum likelihood estimation

The maximum likelihood method for estimation of the parameters, is based on the *likelihood function* which follows from the distribution of the observations described by the probability density function (discussed in section 3.3.1) [van den Bos, 2007]. The importance of this method is that it achieves the CRLB asymptotically, that is, for the number of observations going to infinity. Thus, it is asymptotically most precise and is therefore often used in practice [Van Aert, 2003].

The procedure for this method can be summarized in three steps:

1. The available observations $\mathbf{w} = (w_1, \dots, w_M)^T$ are substituted for the corresponding independent variables $\boldsymbol{\omega} = (\omega_1, \dots, \omega_M)^T$ in the probability density function, for example, in equation (3.8). Since the observations are numbers, the resulting expression depends only on the elements of the parameter vector $\boldsymbol{\beta} = (\beta_1, \dots, \beta_N)^T$.
2. The elements of $\boldsymbol{\beta} = (\beta_1, \dots, \beta_N)^T$, which are the hypothetical true parameters, are considered to be variables. To express this, they are replaced by $\mathbf{t} = (t_1, \dots, t_N)^T$. The logarithm of the resulting function, $\ln P(\mathbf{w}; \mathbf{t})$, is called the *log-likelihood* function of the parameters \mathbf{t} for the observations \mathbf{w} , which is denoted as $q(\mathbf{w}; \mathbf{t})$.

3. The maximum likelihood estimates $\hat{\boldsymbol{\beta}}_{ML}$ of the parameters $\boldsymbol{\beta}$ are defined by the values of the elements of \mathbf{t} that maximize $q(\mathbf{w};\mathbf{t})$, or

$$\hat{\boldsymbol{\beta}}_{ML} = \arg \max_{\mathbf{t}} q(\mathbf{w};\mathbf{t}). \quad (3.16)$$

An important consideration is that the maximum likelihood estimator is usually relatively easily to be derived. All that needs to be done is to establish the dependence of the supposed probability or probability density function of the observations on the parameters.

According to [van den Bos, 2007], the most important properties of the maximum likelihood estimator are:

- *Invariance property.* The maximum likelihood estimates $\hat{\boldsymbol{\gamma}}_{ML}$ of a vector of functions of the parameters $\boldsymbol{\beta}$, that is $\boldsymbol{\gamma}(\boldsymbol{\beta}) = (\gamma_1(\boldsymbol{\beta}), \dots, \gamma_C(\boldsymbol{\beta}))^T$, are equal to $\boldsymbol{\gamma}(\hat{\boldsymbol{\beta}}_{ML}) = (\gamma_1(\hat{\boldsymbol{\beta}}_{ML}), \dots, \gamma_C(\hat{\boldsymbol{\beta}}_{ML}))$.
- *Consistency.* Generally, an estimator is said to be consistent if the probability that an estimate deviates more than a specific amount from the true value or the parameter can be made arbitrary small by increasing the number of observations used.
- *Asymptotic normality.* If the number of observations increases, the probability density function of a maximum likelihood estimator tends to a normal distribution.
- *Asymptotic efficiency.* The asymptotic covariance matrix of a maximum likelihood estimator is equal to the CRLB. In this sense, the maximum likelihood estimator is most precise.

More details about this method can be found in [van den Bos and den Dekker, 2001, van den Bos, 2007].

3.6 Conclusions

In this chapter, the basic principles of statistical parameter estimation theory have been described for two purposes that will be applied in the next chapters. First, these principles were used to find an expression to compute the CRLB following from the concept of the Fisher information matrix. Second, using the CRLB, a STEM experiment can be designed and optimized in terms of their attainable precision of the unknown parameters.

Chapter 4

Comparison of frozen phonon and absorptive potential model for HAADF STEM image simulation

4.1 Introduction

Material properties are strongly connected to the electronic structure, which in turn is critically dependent on the atom positions [Wolf and Yip, 1992, Van Aert et al., 2002c]. It is well known that extremely small changes in the local atomic structure may result into significant changes in their properties [Qi et al., 2010, Alem et al., 2011, Tang et al., 2014]. Therefore, development of quantitative techniques to measure the atomic arrangement of projected atomic columns or individual atoms with sub-picometre precision is required. The enormous progress in hardware and software in scanning transmission electron microscopy (STEM) makes it a powerful tool that enables structure characterization and chemical mapping at the atomic scale with high precision [Van Aert et al., 2009, Grieb et al., 2013]. A key imaging mode is high angular annular dark field (HAADF) STEM, where, the collected signal is sensitive to both the structural and chemical composition.

Although modern STEM is capable of reaching sub-Angstrom resolution, quantitative structure determination requires a) accurate image simulations and b) statistical parameter estimation. Both topics have been discussed in chapters 2 and 3, respectively. Summarizing, the simulations are needed in order to understand the quantum-mechanical nature of the electron-specimen interaction, and parameter estimation is needed to quantify or more correct to estimate the structural parameters from the STEM images. As mentioned in section 1.3, high-angle scattering is mainly dominated by Rutherford and thermal diffuse scattering (TDS) in HAADF STEM imaging. This diffuse intensity resulting from phonon scattering is well described by the inclusion of the frozen phonon

(FP) model explained in section 2.6.1 in the multislice (MS) method. However, computation of the image intensity for a large number of configurations requires an enormous amount of computer power and is time-consuming, especially for STEM images where the image is built up pixel by pixel. Therefore, in order to reduce this computation time, the absorptive potential method (AP) explained in section 2.6.2 can be used as an alternative method [Watanabe et al., 2001, Ishizuka, 2002, Croitoru et al., 2006, Rosenauer et al., 2008].

In this chapter, we will investigate the difference in intensities between the FP and the AP models for HAADF STEM images. First, we will compare the total integrated intensity scattered on the annular STEM detector of an isolated atomic column and an atomic column of an FCC structure. Next, the theoretical limit with which an atomic column can be located in two dimensions (2D) based on HAADF STEM images is explored. This study has been done for three different atom types, selected as a function of their scattering factor amplitude: weakly scattering atoms, e.g. copper (Cu); medium scattering atoms, e.g. silver (Ag); and strongly scattering atoms, e.g. gold (Au). The calculation of the theoretical limit for the precision is based on the concept of the Fisher information matrix and expresses the lower bound of the attainable variance. It is important to mention that this criterion is independent of the method used to estimate the atomic positions. In this manner we will be able to compare the attainable precision when using the AP and FP models for the precision for atoms with different scattering factors in HAADF STEM images.

The organisation of this chapter is as follow. In section 4.2, the parameters used for the STEM simulations are summarized. In Section 4.3, the numerical results for the integrated intensity of an isolated atomic column and a column of an FCC structure is discussed. In section 4.4, the attainable precision with which an atomic column can be located from a 2D STEM image is quantified. Finally, in Section 4.5, conclusions are drawn.

4.2 Simulation parameters

In this chapter, simulations of STEM images with the inclusion of the FP model and the AP model are performed using the MULTEM and STEMSIM programs, respectively. The description of these programs are detailed in section 2.8. Simulations have been performed for isolated atomic columns and FCC structures of Cu, Ag, and Au atoms with a lattice parameter of 3.615 Å, 4.0853 Å and 4.078 Å, respectively. For the isolated columns the distance between atoms in the column is chosen equal to the lattice parameter of their respective FCC structure.

In order to study the annular dependence, simulations are performed for which the detector cover the range from 40 to 160 mrad in steps of 2 mrad. Moreover, simulations are performed using three detectors [40 - 80] mrad, [80 - 120] mrad and [120-160] mrad as shown in table 4.1. The Debye-Waller factor for the three atom types has been calculated [Gao and Peng, 1999] at a temperature of 300 K, an acceleration voltage 300 kV, and the defocus has been adjusted to the Scherzer conditions. The other parameters are shown in table 4.1. For the FP simulations, 200 uncorrelated phonon configurations have been computed using the Einstein model.

This study was carried out assuming symmetric and concentric annular detectors, and considering an ideal detector sensitivity.

Table 4.1: Parameters for the MS simulation

Parameter	Symbol	Value
Annular detector 1	D_1 (mrad)	40-80
Annular detector 2	D_2 (mrad)	80-120
Annular detector 3	D_3 (mrad)	120-160
Debye-Waller factor Cu	(\AA^2)	0.5747
Debye-Waller factor Ag	(\AA^2)	0.7612
Debye-Waller factor Au	(\AA^2)	0.7003
Acceleration voltage	E_0 (kV)	300
Defocus	Δf (\AA)	-14.03
FWHM of the source image	(\AA)	0.8
Spherical aberration of 3rd order	C_3 (mm)	0.001
Spherical aberration of 5th order	C_5 (mm)	0.0
Convergence angle	α_0 (mrad)	21.00
Pixel size to sample atomic potential	(\AA)	0.0195

4.3 Integrated intensity

In this section, both the FP and the AP models will be compared in terms of the integrated intensity that is produced by an atomic column. This integrated intensity can also be interpreted as the so-called scattering cross section [De Backer et al., 2015b], that has been shown to be a very successful performance measure to count the number of atoms in an atomic column from a single STEM image [Retsky, 1974, Singhal et al., 1997, Van Aert et al., 2009, Van Aert et al., 2013, De Backer et al., 2013] and will be defined as the total scattered intensity integrated over the scanned area. Furthermore, the scanned area will be selected in such a way that the atomic column will be placed in the centre in order to collect most of the scattered intensity [MacArthur et al., 2014, Rosenauer et al.,

2009]. In STEM images the intensity for each pixel can be calculated using equation (2.42) for both the FP or the AP models. Following this definition, the integrated intensity can be defined as

$$I_{int} = \sum_k^K \sum_l^L f_{kl} \Delta x \Delta y, \quad (4.1)$$

with f_{kl} the fraction of electrons expected to be recorded by the detector at pixel (k,l) in a 2D STEM image with $K \times L$ pixels, Δx and Δy is the pixel size along the x - and y -axis, respectively (usually $\Delta x = \Delta y$).

The total intensity, calculated with the FP model is obtained by averaging the intensity of different configurations given by equation (2.32). Here, the MS method treats the interaction between the electron and the rigorously displaced atoms as an elastic (coherent) scattering process in which the scattered wave still interferes with the unscattered wave [Van Dyck, 2011]. On the other hand, the AP model describes the TDS intensity by including absorption in the dynamical equation of the electron diffraction using a complex lattice potential, and calculates this intensity following equation (2.41). In order to make a comparison between both methods, the integrated intensity for three atom types (Cu, Ag and Au) will be investigated in three ways: first, analysing how both methods distribute the integrated intensity over the annular detectors as a function of thickness; second, quantifying the integrated intensity for three detector ranges of an isolated column; and third, quantifying the integrated intensity of a column of an FCC structure in the same way as the second part.

4.3.1 Distribution over the annular detector

Using equation (4.1), the integrated intensity produced by an isolated atomic column has been calculated as a function of thickness. Therefore, STEM images have been simulated with a pixel size of 0.15 \AA , over a square region with a side length of 20 \AA . The atomic column with thickness up to 20 nm was placed in the centre of the scanned region. The annular detector cover a range from 40 to 160 mrad in steps of 2 mrad . For each ring (annular detector of 2 mrad), the integrated intensity was computed as a function of thickness. In this manner, it can be investigated how both methods distribute the intensity over the annular detector range for atoms with different scattering factors. The results of these distributions are shown in figure 4.1. The comparison of both methods has been done in the detector range of 40 to 160 mrad , therefore, when we refer to low angles it means the lower values of this range.

Figures 4.1a-c and 4.1d-f show the results of the distribution of the integrated intensity computed from simulations performed using the FP and the AP models, respectively. From these figures, with equal scale-bar for the intensity, we

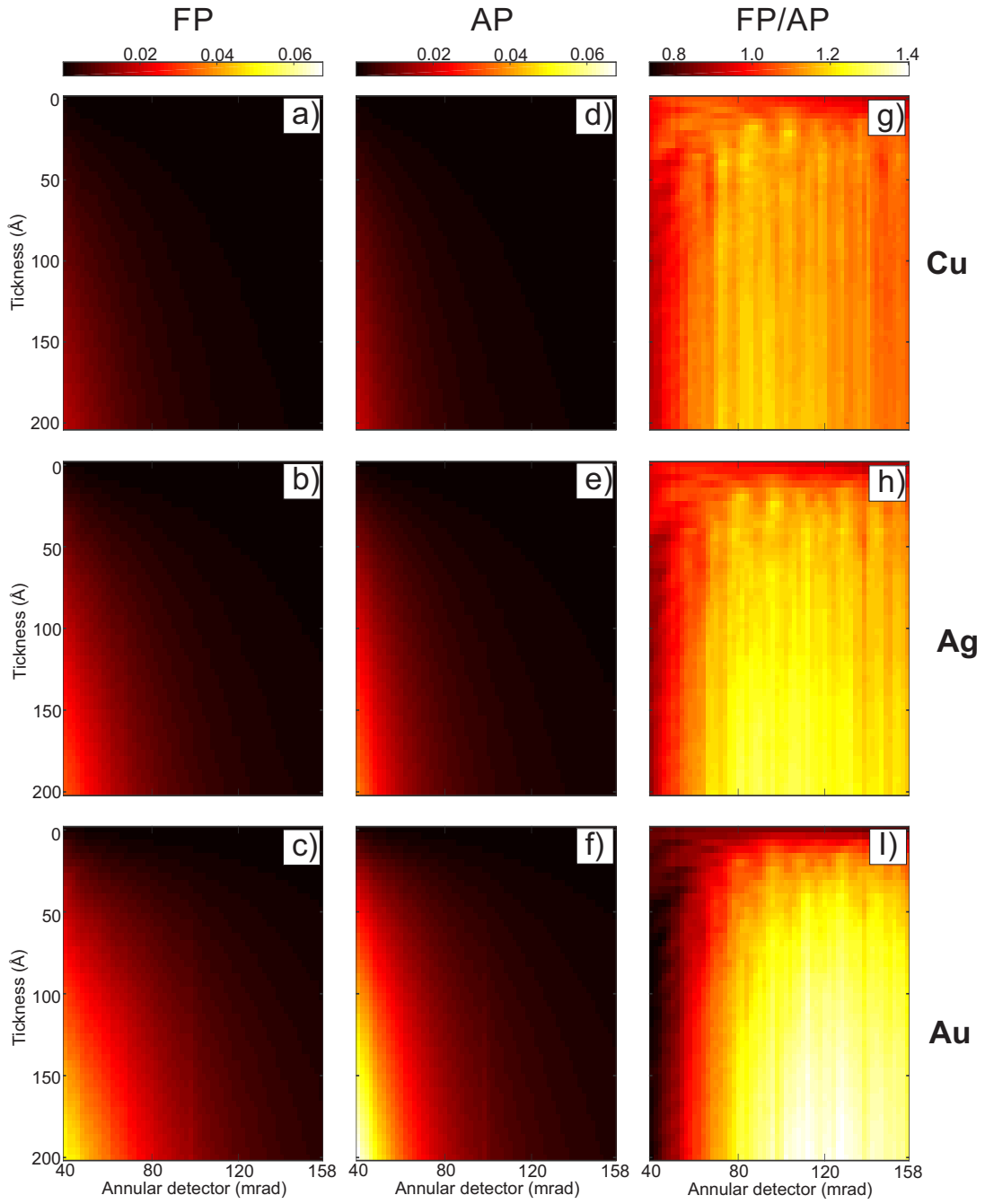


Figure 4.1: Distribution of the integrated intensity over the detector range as a function of thickness and inner angle of an annular detector of width 2 mrad for isolated columns of Cu, Ag, and Au atoms. Figures (a-c) show the results using the FP model, figures (d-f) show the results using the AP model, and figures (g-i) show the ratio between the FP and AP models (FP/AP).

can observe that the amount of intensity produced for both methods are different. This difference seems to change as a function of: a) thickness, b) detector range, and c) atom type. The ratio between both methods (FP/AP) illustrated in Figures 4.1g-i, shows in more detail the difference between both models. In these figures, for most detector angles and thickness values, the FP model results into higher intensities as compared to the AP model. Only for a small part of the detector range (low angles), the AP model has equal or higher intensity as compared to the FP model. In these figures, we can see more clearly how the ratio between both methods also depends on the atom type suggesting that this ratio increases as a function of the scattering factor. For example, the ratio of the intensity for Au atoms (strong scattering factor) is larger as compared to the intensities for atoms such as Ag (medium scattering factor) and Cu (weak scattering factor).

More particularly, after comparing both methods for the three atom types, we observe the following:

- *For atoms of Cu*, figures 4.1a,d show that both methods have a similar distribution of the scattered intensity. however, the ratio between both methods is not linear as we can see more clearly in figure 4.1g where larger differences between both methods are observed in the range between 70 to 120 mrad. For this atom type, the ratio between both models oscillates in the range of 0.9 to 1.2.
- *For atoms of Ag*, figures 4.1b,e show that the AP model produces more scattering than the FP model for low angles (lower than 50 mrad). For higher angles, the difference between both methods starts to increase, especially in the range of 80 to 120 mrad where the FP model results into higher intensities as compared to the AP model. This is shown in figure 4.1h. For this atom type, the ratio between both models oscillates in the range of 0.9 to 1.3.
- *For atoms of Au*, figures 4.1c,f show a similar behaviour for atoms of Ag although even with larger ratios between both methods. Figure 4.1i shows this behaviour more clearly. In this figure, we can see that the detector range, where the AP model results into larger intensity values than the FP models increases with respect to atoms of Ag and Cu. The highest difference between both methods is found in the range of 100 to 150 mrad and for thicknesses larger than 100 Å. The ratio between both models oscillates in the range of 0.7 to 1.4.

Based on this comparison, we can conclude that both models are only in good agreement in a very small detector range. This range depends on the atom type. Furthermore, the comparison shows that the AP model results into larger intensity values than the FP model for low angles. The range of angles depends

on the atom type. For larger angles the FP models results into more scattering more intensity than the AP model. This distribution suggest that the integrated intensity depends on the collected detector range. For example, if we compute the integrated intensity for Au atoms with the intensity using a detector range in between 40 and 80 mrad, both will show similar result because de difference in low angles will be compensate with the difference observed for higher angles.

4.3.2 Isolated column

In the previous subsection, the distribution of the integrated intensity as a function of detector angle and thickness has been computed for both models. In order to quantify the difference of the integrated intensity between both models for realistic detector settings, we proceed in the same way as in the previous subsection. We use the detectors [40 - 80] mrad, [80 - 120] mrad and [120-160] mrad and all other parameters have been kept constant. The results are shown in figure 4.2, where the integrated intensity is plotted as a function of thickness for an atomic column consisting of Cu, Ag, and Au atoms. From these figures, we conclude that:

- for detector D_1 (first column of figure 4.2), both methods are in good agreement for small thicknesses with values around 14 nm, 10nm, and 2nm for atoms of Cu, Ag, and Au, respectively. For larger thicknesses, the FP model produces more intensity than the AP model for Cu and Ag, whereas for Au, the effect is opposite.
- for detector D_2 (second column of figure 4.2), both methods are in good agreement up to thicknesses around 2 nm for the three atom types. For larger thicknesses, the FP model produces more intensity than the AP model. The difference between both methods scales with the thickness and the scattering factor.
- for detector D_3 (third column of figure 4.2), both methods show the same behaviour as for detector D_2 .

Assuming the FP as the most accurate model, we can conclude from the results shown in figure 4.2 that for the first detector (D_1) the AP model underestimates the integrated intensity for Cu and Ag, whereas it overestimates for Au. For the second (D_2) and third (D_3) detector, the integrated intensity behaves similarly. For both detectors, the AP model underestimates the intensity. This effect seems to increase as a function of thickness and also as a function of the scattering factor. The fact that both methods show similar results for detector D_1 does not mean that both methods are distributing the intensity in the same way as shown in figures 4.1g-i. In this detector range, there is a compensation of the intensity. For angles close to 40 mrad, the AP model scatters more intensity

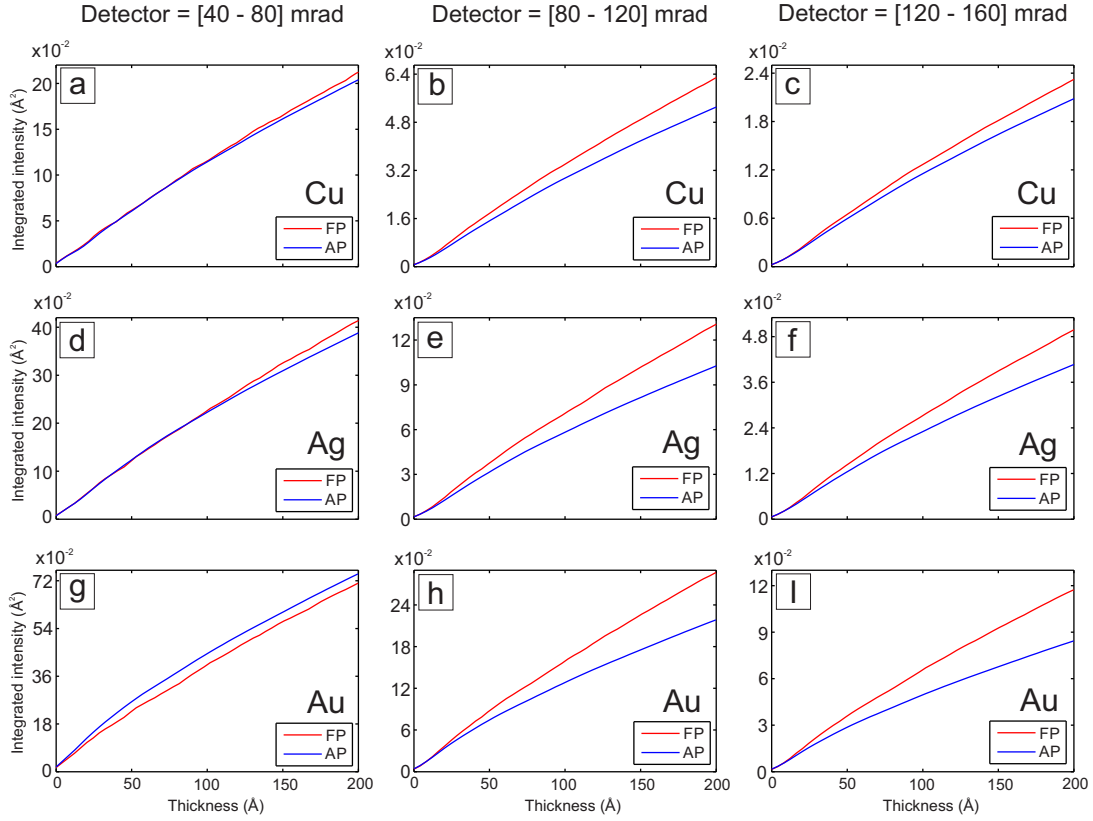


Figure 4.2: Integrated intensity as a function of thickness for an isolated column of atoms of Cu, Ag, and Au. The integrated intensity was calculated from simulations performed using the MS algorithm with the inclusion of the FP (red line) and AP (blue line) model. Figures (a,d,g) correspond to the detector of 40 to 80 mrad; figures (b,e,h) correspond to the detector of 80 to 120 mrad; and figures (c,f,i) correspond to the detector of 120 to 160 mrad.

and for angles close to 80 mrad the FP model scatters more intensity.

The impact of the observed differences in intensity between both models will depend on the purpose for which the intensity are used. For example, if one wants to quantify the location of atomic columns from 2D STEM images, the difference in intensity between both methods is perhaps not important. However, but if the analysis is focused on the quantification of the number of atoms or atom type, this difference can introduce wrong values. From equation (2.36) we can see that the intensity is related to the scattering factor amplitude of the atom type. From the results, we can observe that atoms with high scattering factor scatter more intensity in higher angles as compared with atoms with weak scattering factor. One should realize that this study is based on an isolated column and does not take into account the effect caused by cross-talk produced by the neighbouring columns. Therefore, in the next subsection we will analyse

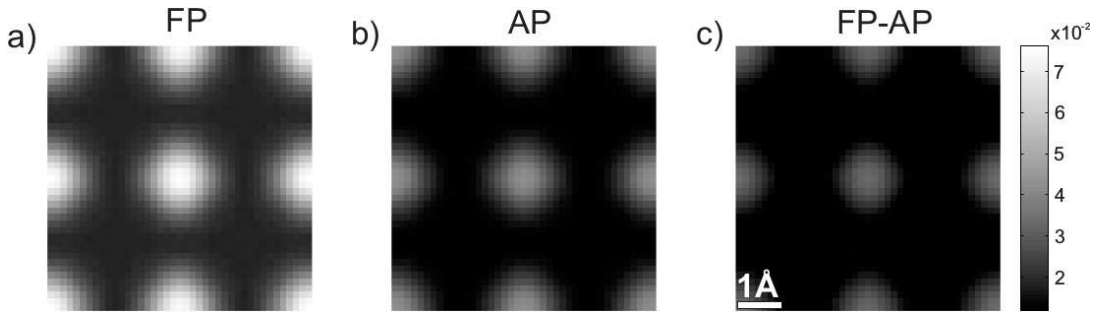


Figure 4.3: Simulated STEM images of an FCC structure of Au atoms along the [001] zone-axis for a 20 nm thick crystal and a detector range of 120 to 160 mrad, using the MS algorithm with the inclusion of: a) the frozen phonon model, and b) the absorptive potential approximation. Figure (c) is the difference between the frozen phonon and the absorptive potential. All the images are plotted on the same scale.

this effect for more realistic specimens.

4.3.3 FCC structure

To compare the integrated intensity between both models for more realistic specimens, where the cross-talk produced by neighbouring columns is taken into account, an FCC structure of Cu, Ag, and Au atoms with lattice parameters of 3.615 Å, 4.0853 Å, and 4.078 Å, respectively, were assumed. The simulations were performed using the same detectors (D_1 , D_2 , and D_3) and the parameters mentioned in table 4.1. The integrated intensity was computed over a scanned area equivalent to one unit cell with a pixel size of 0.145 Å, along the [001] zone-axis as is shown in figure 4.3. In order to compare the integrated intensity with respect to one atomic column, the integrated intensity of one unit cell is divided by the number of projected atomic columns in one projected unit cell, which in this case is 4. Using this criterion the integrated intensity was computed as a function of thickness. The first, second and third column of figure 4.4, show the results of the integrated intensity for the three atom types for detectors D_1 , D_2 and D_3 , respectively, as a function of thickness.

The results of the integrated intensity computed as a function of thickness for a column of an FCC structure shown in figure 4.4, show similar results as compared with the integrated intensity computed for an isolated column shown in figure 4.2. The difference are very small, but the behaviour (trend of the curve) in general is the same for the three detectors (D_1 , D_2 and D_3) and three atom-types. This means that neighbouring columns do not cause larger deviations in the integrated intensity.

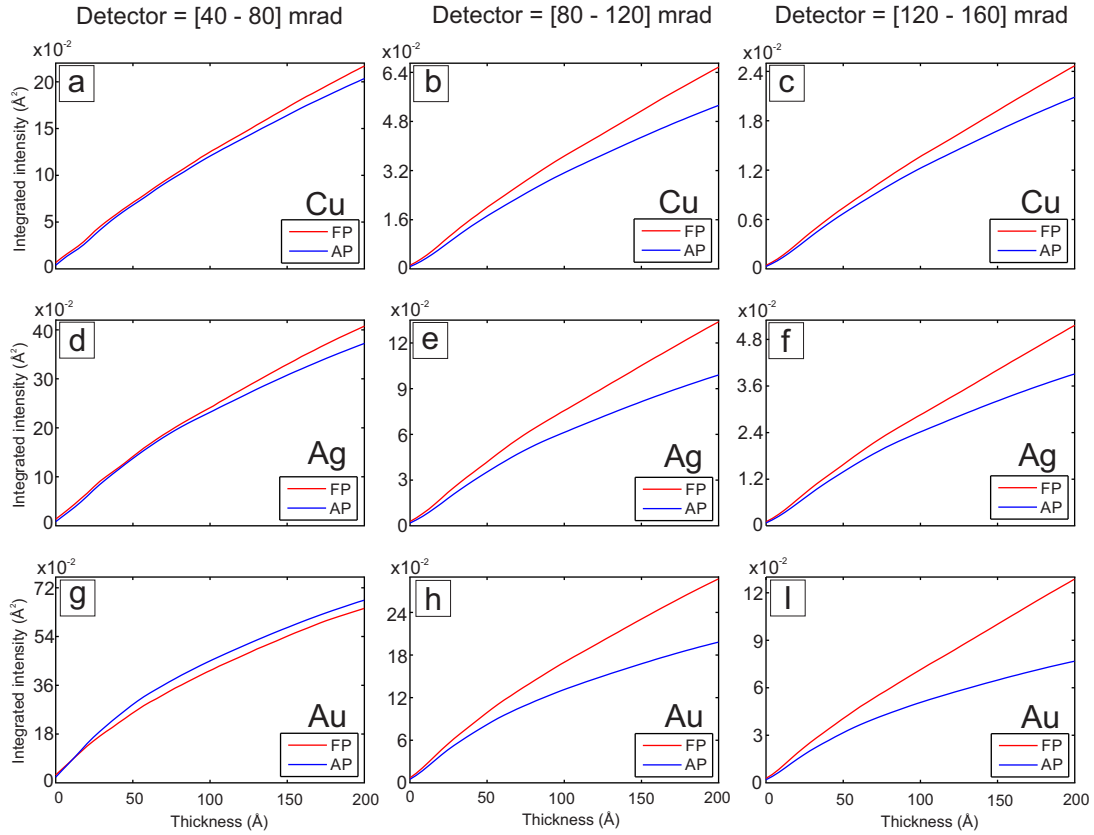


Figure 4.4: Integrated intensity as a function of thickness for an atomic column of FCC structure of atoms of Cu, Ag, and Au. The integrated intensity was calculated from simulations performed by using the MS algorithm with the inclusion of the FP (red line) and AP (blue line). Figures (a,d,g) correspond to the detector of 40 to 80 mrad; figures (b,e,h) correspond to the detector of 80 to 120 mrad; and figures (c,f,i) correspond to the detector of 120 to 160 mrad.

This study has also been performed for Au atoms with acceleration voltages of 80 kV and 200 kV keeping the same input parameters and using the same equivalent semi-aperture angle used for 300 kV. The results for these voltages are shown in figure 4.5. From this figure we can observe that for the detector ranging from 40-80 mrad for both voltages the behaviour is the same, but the difference between both models increase. For the detectors ranging from 80-120 mrad and 120-160 mrad the FP model present higher slope as compared to the AP model, for thickness up to about 10 nm the AP is higher than the FP model, after that, the FP is higher and the difference scales with thickness. These results show that for these acceleration voltages both models have higher differences between them.

The results show that the AP model leads to considerable differences especially

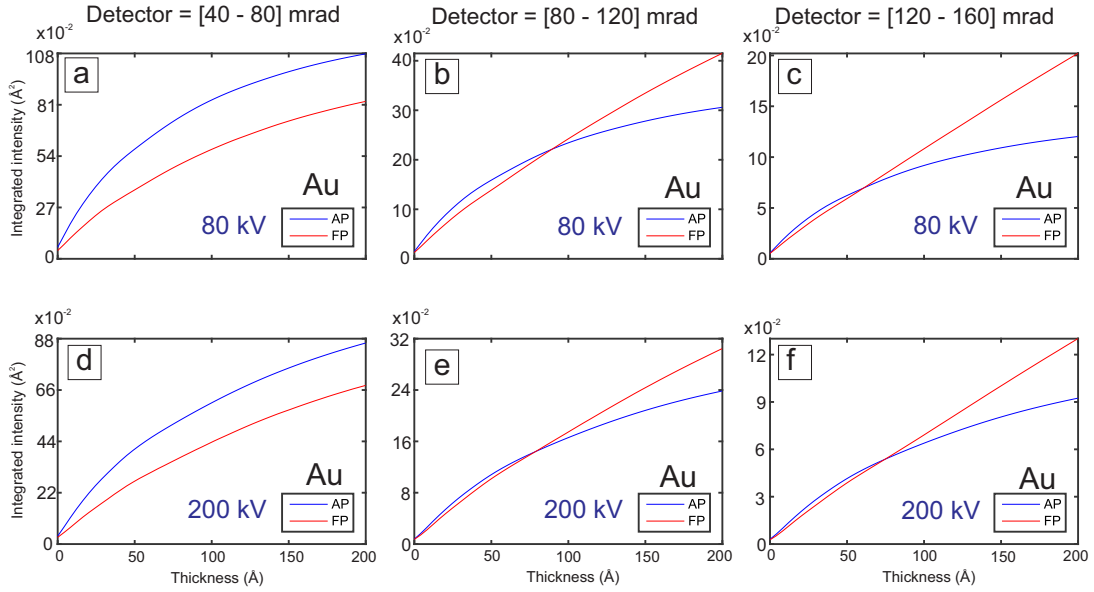


Figure 4.5: Integrated intensity as a function of thickness for an atomic column of FCC structure of Au atoms. The integrated intensity was calculated from simulations performed by using the MS algorithm with the inclusion of the FP (red line) and AP (blue line). Figures (a-c) correspond to 80 kV; figures (e-g) correspond to 200 kV. For both acceleration voltages the detector were ranging from 40-80 mrad, 80-120 mrad, and 120-160 mrad.

for detectors D_2 and D_3 , here the intensity is underestimated as a function of thickness and atom type. These results suggest that we need to be careful when using the AP model for a quantitative analysis of the number of atoms or atom type. It is also important to mention that this result cannot be generalized for all atom types. Table 4.2 shows the maximum number of atoms for which both methods differ, from each other up to a thickness of 20 nm. Figure 4.4 shows that the AP model underestimates the number of atoms with respect to the FP model with only one exception for the detector D_1 of Au atoms, where in this case the intensity is overestimated.

Table 4.2: Maximum difference of number of atoms per detector between the FP and the AP model up to thickness of 20nm.

	D_1	D_2	D_3
Cu	4	12	10
Ag	5	14	14
Au	5	17	22

4.4 The ultimate precision to locate atoms

In this section, both the FP and AP models will be compared in terms of the ultimate precision with which an atomic column can be located in 2D [Van Aert et al., 2002b, Gonnissen et al., 2016] from images acquired using HAADF STEM. The ultimate precision, i.e. the lower bound on the standard deviation, is given by the elements of the diagonal of the inverse of the Fisher information matrix F , given by equation (3.14). From this equation, it is clear that the elements of the Fisher information matrix have to be calculated using the derivatives of the parametric model of the intensity observations λ_{kl} given by equation (3.5) with respect to the position coordinates of the projected atomic columns. In this study, the parametric model for the intensity observations λ_{kl} is simulated using MS method.

As mentioned in chapter 2.5, the MS method is a numerical solution of the Schrödinger equation. In order to calculate the partial derivatives, additional sets of MS simulations are required in which a single atomic column is shifted along an axis. For example, for the derivative of an atomic column with respect to the x -coordinate, this column is displaced along the x -axis. The partial derivatives are then approximated using equation (3.15) where in this case h is the shift of the entire atomic column from its regular position along the x -axis. Similarly, the derivatives with respect to the y -axis, and other columns can be calculated.

The comparison between the FP and the AP models will be done in two ways: a) comparing the ultimate precision to locate an isolated column of Au atoms from 2D STEM images, b) comparing the ultimate precision to locate a column of FCC structures from 2D STEM images. The objectives are to evaluate how the ultimate precision computed for an isolated column changes with respect to and FCC structure. Next, it will be compared if both the FP and AP models have the same results for the ultimate precision. For these calculations, the convergence of the derivatives was analysed as a function of the displacement h of equation (3.15), the number of configurations in the FP model, and the pixel size of the images. The values which are found in this manner are: $h = 2$ pm, 200 FP configurations, and a pixel size of 0.35 \AA .

4.4.1 Isolated column

From equation (3.14), it can be seen that the calculation of the Fisher information matrix requires the derivatives of the expectation model λ_{kl} with respect to the unknown parameters, in this case, the unknown parameters are the projected coordinates x and y of an isolated atomic column given by the vector

$$\boldsymbol{\beta} = (\beta_x, \beta_y). \quad (4.2)$$

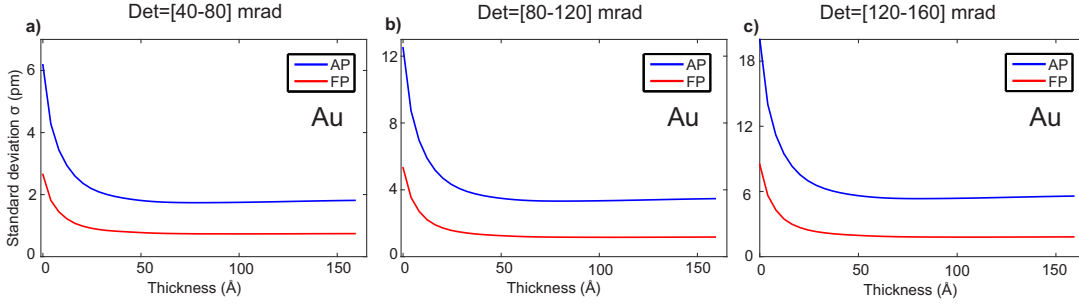


Figure 4.6: The ultimate precision σ to locate an isolated column of Au atoms as a function of the thickness from simulated STEM images performed by the MS algorithm with the inclusion of the FP model (red-line), and the AP (blue-line), for three detectors: a) [40-80] mrad, b) [80-120] mrad, and c) [120-160] mrad.

Due to the cylindrical symmetry of the intensity distribution of the image of the atomic column, the information obtained from the derivatives with respect to the x - and y -axis are the same. Therefore, the Fisher information matrix simplifies to:

$$F = \begin{bmatrix} F(1,1) & F(1,2) \\ F(1,2) & F(2,2) \end{bmatrix}. \quad (4.3)$$

From equation (3.12), it follows that the CRLB on the variance $\sigma_{\beta_x}^2$ or $\sigma_{\beta_y}^2$ is given by the corresponding diagonal element of F^{-1} :

$$\sigma_{\beta_x}^2 = \sigma_{\beta_y}^2 = F^{-1}(1,1). \quad (4.4)$$

The square root of the values of equation (4.4) give us the standard deviation σ with respect of the x - and y -axis, which in this case are equal.

The CRLB has been computed for the FP and AP model using a square region of 12.234 \AA with a pixel size of 0.3398 \AA , for the atomic column at the centre of this region. An incident electron dose of $21652 e^-/\text{\AA}^2$ was used, which corresponds to a beam current of 40 pA and a pixel dwell time $\tau = 10 \mu\text{s}$. The results for the precision are shown in figure 4.6 as a function of thickness. From this figure, we can observe that the ultimate precision has the same behaviour for both methods for the three detectors. The precision improves as a function of thickness but beyond a certain value, the gain in precision is marginal. The behaviour is the same for different detectors. For higher angles, the precision decreases i.e. the standard deviation increases. However, when comparing the results of both methods, the FP model shows a better precision for the three detectors as compared to the AP model. The difference between both methods is approximately constant with thickness. It is important to note that the precision is different for both methods even for the detector D_1 which shows similar results for the integrated intensities. Figure 4.2(g) also shows that the

AP model scatters more intensity than the FP model, but in terms of precision the FP predicts better precision as is shown in figure 4.6(a). This means that the distribution of the intensity over the detectors is also different for both methods.

4.4.2 FCC structure

In subsection 4.4.1, the ultimate precision to locate an atomic column in 2D was computed for an isolated column. In order to compute this theoretical limit on the precision for an atomic column where its intensity is affected by the crosstalk of the neighbouring columns, an FCC structure was assumed. The precision also depends on the atom types. Calculations were performed for both the AP and the FP models using the same settings used for the integrated intensity in section 4.3.3.

Figure 4.7 shows the result of the ultimate precision as a function of the thickness for the three atoms types. From this figure, the precision of the atoms of Cu shows a similar behaviour for both methods. The precision improves as a function of thickness. However, beyond a certain value this gain is only marginal. For Ag and Au, the precision first improves as function of thickness and beyond a certain value the precision starts to decrease. This behaviour is more pronounced for the Au than for the Ag atoms.

These results show that the behaviour of the ultimate precision to locate an atomic column from 2D STEM images for the three atom types are strongly related to their scattering factor amplitude. For atoms with a small scattering factor amplitude such as Cu, the intensity is scattered close to the location of the atomic column position and therefore the contribution due to crosstalk is small. For atoms with a medium scattering factor such as Ag, the effect of crosstalk starts to make an influence on the calculation of the precision. For atoms with a strong or high scattering factor amplitude, such as Au, the influence of crosstalk is even more pronounced in the calculation of the precision.

From figure 4.7 it may also be observed that the precision differs for both models. For atoms of Cu, the AP shows better precision as compared to the FP model for thicknesses larger than 1 nm for the three detector ranges. This difference increases as a function of the angles, i.e. detectors with higher angles results into a larger difference for the precision. For atoms of Ag, the same behaviour is presented for the detector ranging from 40-80 mrad. For the other two detectors, the FP presents a better precision as compared to the AP model for all thicknesses. For atoms of Au, the behaviour of the precision for the detector ranging from 40-80 mrad is the same as presented for atoms of Cu. For the other two detectors the AP shows a better precision for small thicknesses, and the FP for higher thicknesses.

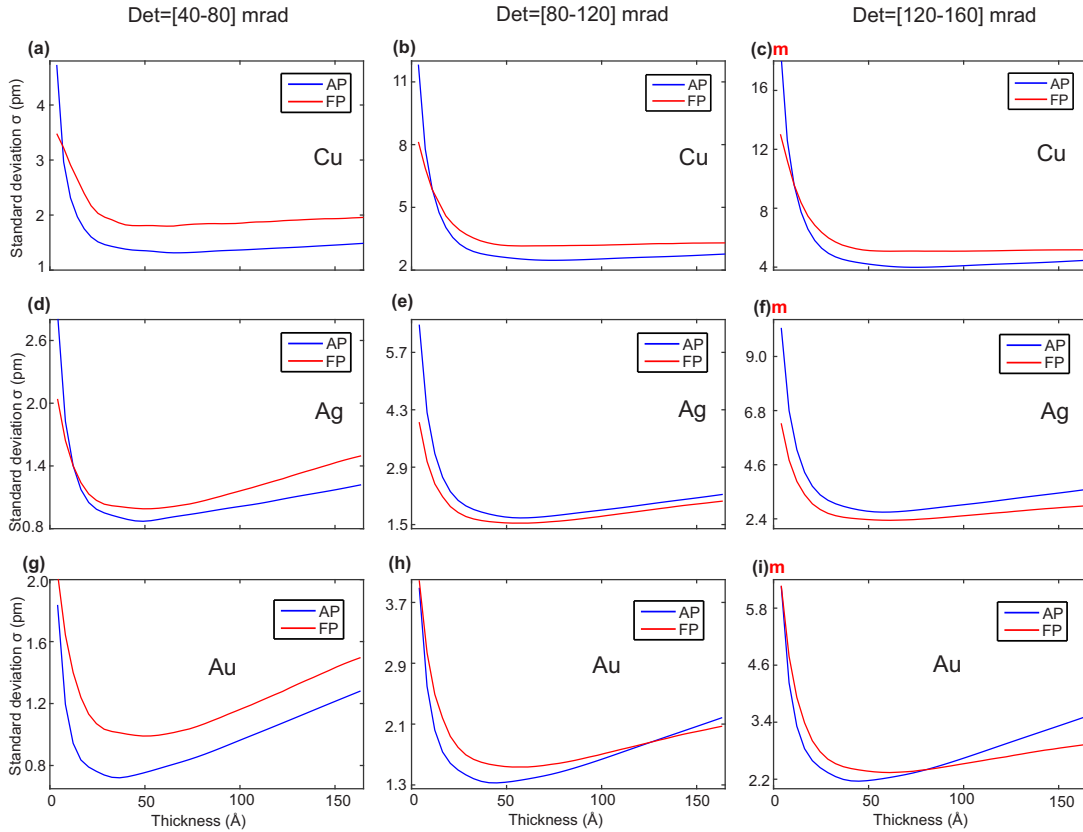


Figure 4.7: The ultimate precision to locate the central atomic column of Cu, Ag, and Au atoms, in an FCC structure using the collected intensity of three detectors: (a,d,g) [40-80] mrad. (b,e,h) [80-120] mrad. (c,f,i) [120-160] mrad. This precision was computed from simulated STEM images performed using the MS algorithm with the inclusion of the FP (red-line) and AP model (blue-line).

4.5 Conclusions

In this work, two of the most popular methods used to simulate STEM images, the frozen phonon and the absorptive potential model, were compared in terms of the integrated intensity and the theoretical limits with which an atomic column can be located in 2D based on the acquisition of HAADF STEM images.

The integrated intensity was computed by integrating the total scattered intensity over the scanned area. The results shows a similar trend of the intensity as a function of thickness, but with different values for both models in the cases of an isolated atomic column and an atomic column of FCC structure. For the detector ranging from 40 to 80 mrad the difference of the integrated intensity between both models is small especially for small thickness. For the detectors ranging from 80 to 120 mrad and 120 to 160 mrad, this difference increases as a

function of thickness and atom type. It means that atoms with strong scattering factor present more difference in the integrated intensity. From this comparison the results suggest that we need to be careful when using the absorptive potential model for quantification using the integrated intensity because for high angles and large thickness this model is underestimating the integrated intensity.

Using the concept of the Cramér-Rao lower bound, the ultimate precision with which an atomic column can be located from 2D HAADF STEM images has been computed for an isolated column of Au atoms and for an atomic column of an FCC structure of Cu, Ag, and Au atoms. For an isolated atomic column of Au atoms, the precision improves as a function of thickness, but beyond a certain value, the gain in precision is marginal in both methods. However in all the thickness the frozen phonon present better precision with respect to the absorptive potential model. For the atomic column of the FCC structure, the ultimate precision depends on the atom type and detector range. For the detector ranging from 40 to 80 mrad, the absorptive potential shows a better precision with respect to the frozen phonon model for the three atom types. For the detectors ranging from 80 to 120 mrad, the results for both methods are quite similar with small changes in the trend of the curve of the precision for the Au atoms cross each other. The difference between both methods are in the picometre scale for the simulations settings used in this chapter.

Chapter 5

Ultimate precision of locating atoms of a nanocluster in 3D from a tilt series of STEM images

5.1 Introduction

Following the definition in section 1.2, nanoclusters, also known as atomic-cluster or super-atom [Schmid and Fenske, 2010, Wang, 2014, Deepak et al., 2015], are aggregates of atoms with a diameter size below about 2 nm [Schmid and Fenske, 2010, Wang, 2014]. The reason to separate nanoclusters from nanoparticles is that nanoclusters show typical quantum size behaviour [Schmid and Fenske, 2010, Wang, 2014]. Due to their unique physical and chemical properties, nanoclusters play key roles in a wide range of materials and devices [Alonso, 2011, Al Dosari and Ayes, 2013]. These properties are determined by the specific three-dimensional (3D) morphology, structure and composition [Olson, 2000] and can vary greatly with every addition or subtraction of an atom. It is well known that extremely small changes in their local structure may result into significant changes of their properties [Tang et al., 2014, Alem et al., 2011, Qi et al., 2010]. Therefore, development of techniques to measure the atomic arrangement of individual atoms down to (sub)-picometre precision will allow one to fully understand and greatly enhance the properties of the resulting materials, increasing the number of applications.

As mentioned in section 1.4, electron tomography using aberration-corrected scanning transmission electron microscopy (STEM) can achieve atomic resolution in three dimensions. High-angle annular dark field (HAADF) STEM has become a popular technique for materials characterisation in 3D because the collected signal increases proportional with the atomic number Z and the specimen thickness.

For many years, the ultimate goal has been to achieve electron tomography with atomic resolution. Although this is not yet a standard possibility for all structures, significant progress has recently been achieved using different approaches [Van Aert et al., 2011, Bals et al., 2011, Goris et al., 2012]. Once the atoms can be resolved in 3D, the next challenge is to refine the atom positions in a quantitative manner [Goris et al., 2015, Xu et al., 2015]. However, the answer to the question how precise these measurements are, is still open.

The ultimate aim in materials science is to obtain a precision in the (sub)-picometre range. Therefore, the subject of this chapter is to investigate if this goal is within reach. In this chapter, we investigate the theoretical limits with which atoms of a nanocluster can be located in 3D based on the acquisition of a tilt series of annular dark field (ADF) STEM images. Since we are interested in the theoretical limits, we assume an ideal experimental setup for the computation of the ultimate precision. This means that we assume that scan noise and alignment errors can be avoided or can be corrected for [Jones and Nellist, 2013, Yankovich et al., 2014, Jones et al., 2015] and that the sample is a perfect free-standing nanocluster. Therefore, beam damage, the re-arrangement of the nanocluster, and the effect of a sample support for the nanocluster are not considered in this theoretical study. Ultimately, the reliability with which one can measure the atom positions is limited by the unavoidable presence of electron counting noise in the acquired projection images, which is the so-called Poisson noise or shot noise. This sets fundamental limits to the precision that can be obtained. Use of the concept of Fisher information allows us to determine an expression for the highest attainable precision with which positions of atoms can be located in 3D, or equivalently, an expression for the lower bound on the attainable variance. This is the Cramér-Rao lower bound (CRLB), it is essential to remark that this lower bound is independent of the estimation method used. In this context, it means that the CRLB is independent of the tomographic reconstruction algorithm. The expression for the lower bound on the variance not only helps to compute the precision that can ultimately be achieved but also to determine the optimal angular tilt range, required electron dose, optimal detector angles, and number of projection images.

Furthermore, it is important to note that this concept of precision is different from the well-known concept of resolution, expressing the possibility of perceiving separately two point sources. Resolution is interpreted in many ways since it is not unambiguously defined. Therefore, several resolution criteria, including Rayleigh's [Rayleigh, 1879] have been proposed in the past. Such classical resolution criteria are concerned with calculated images, that is, noise-free images exactly described by a known parametrised model. However, these criteria do not take the signal-to-noise ratio into account and disregard the possibility of using this prior knowledge about the image intensity distribution to extract

numerical results from the observations by model fitting using parameter estimation methods. For experimentally acquired images, model fitting never results in a perfect match in the presence of noise such that the component locations can only be estimated with limited statistical precision [Bettens et al., 1999, Van Aert et al., 2002b]. This statistical precision will be quantified in this chapter for the coordinates of the central atom of a nanocluster.

This chapter is organised as follows. In section 5.2, the parametric models for the intensity observations are described. In section 5.3, an expression is derived for the attainable precision with which atoms can be located in 3D. Section 5.4 describes how images of gold nanoclusters have been simulated and the approximations that have been made. In section 5.5, the dependence of the attainable precision on the choice of experimental settings is studied. In section 5.6, conclusions are drawn.

5.2 Parametric model for the intensity observations

In chapter 3, an expression for the attainable precision was derived using a parametric model, which is based on the multislice (MS) method explained in chapter 2. Although the MS method is more accurate to describe the electron-object interaction, it is very time-consuming, especially when simulating a tilt series of images. Therefore, also the Gaussian approximation model proposed by Curley et al. [Curley et al., 2007] will be used in order to perform fast, albeit approximate, simulations. This will allow us to get insight into the precision that can be attained to locate atoms in 3D.

5.2.1 Rotation of a nanocluster

A tilt series of ADF STEM images of a nanocluster needs to be modelled, where the positions of the N atoms correspond to the elements of the parameter vector $\boldsymbol{\beta} = (\beta_{x1}, \beta_{y1}, \beta_{z1}, \dots, \beta_{xN}, \beta_{yN}, \beta_{zN})$. In the reference coordinate system, we assume that the origin is located at the position of the central atom of the nanocluster. In this study, single-axis tomography is assumed in which two-dimensional (2D) images are obtained when tilting a nanocluster around a fixed tilt axis. The tilt axis corresponds to the y -axis and the electron beam is assumed to be parallel to the z -axis as indicated in Figure 5.1. For a rotation over $[-90, 90]$ degrees, the x - and z -axis become equivalent for a symmetric structure around the rotation axis y . Furthermore, the tilt angles θ^j , $j = 1, \dots, J$ are equidistantly sampled in the interval $[-\alpha, +\alpha]$ corresponding to a full angular tilt range if $\alpha = \pi/2$. At each tilt angle θ^j , the locations of the N atoms $\boldsymbol{\beta}^j = (\beta_{x1}^j, \beta_{y1}^j, \beta_{z1}^j, \dots, \beta_{xN}^j, \beta_{yN}^j, \beta_{zN}^j)$

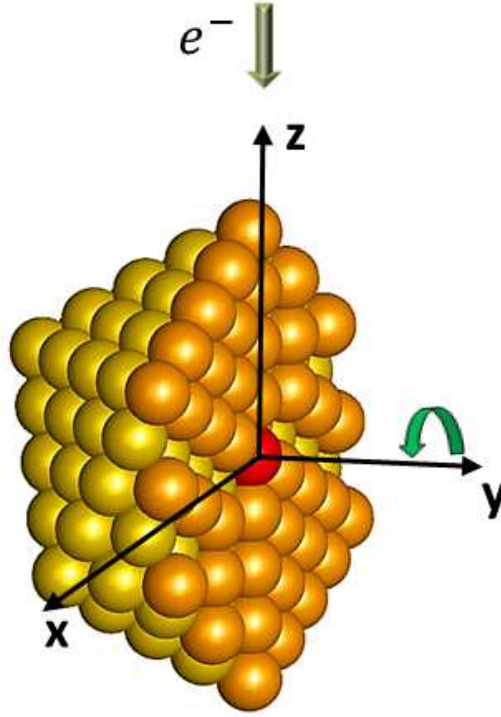


Figure 5.1: Cross-section of a nanocluster indicating the x -, y - and z -axis, the central atom (red atom), and the atoms of the central plane (orange atoms).

with respect to the reference coordinates system are then given by (see appendix B.1):

$$\begin{bmatrix} \beta_{xi}^j \\ \beta_{yi}^j \\ \beta_{zi}^j \end{bmatrix} = \begin{bmatrix} \cos\theta^j & 0 & \sin\theta^j \\ 0 & 1 & 0 \\ \sin\theta^j & 0 & -\cos\theta^j \end{bmatrix} \begin{bmatrix} \beta_{xi} \\ \beta_{yi} \\ \beta_{zi} \end{bmatrix} \quad (5.1)$$

In the following subsections, the Gaussian approximation model and the MS method (explained in section 2.5) will be used in order to simulate images for each tilt angle θ^j .

5.2.2 The Gaussian approximation model

The Gaussian approximation model (GAM) is based on the assumption of kinematic scattering of electrons and has been proposed by Curley et al. for mono metallic systems [Curley et al., 2007]. In this model, the ADF STEM image intensity of a nanocluster is described as a linear combination of image contributions of all atoms constituting the object under study. When assuming a 3D Gaussian function for each atom, the contribution of atom i to a projection

image is given by [Logsdail, 2013]:

$$(f_{kl}^j)^i = Z_i^\zeta \exp\left(-\gamma \frac{(x_k - \beta_{xi}^j)^2 + (y_l - \beta_{yi}^j)^2}{r_i^2}\right) \quad (5.2)$$

where (x_k, y_l) is the position of the probe and $(\beta_{xi}^j, \beta_{yi}^j)$ is the position of the i th atom in projection at tilt angle θ^j . Furthermore, γ is an atom type dependent constant, determining the decay of the electron scattering as a function of the distance to the centre of the projected atom, Z_i and r_i are the atomic number and atomic radius of the i th atom, respectively, and ζ is a scattering constant depending on the collection angle of the detector. Realistic values for the parameters ζ and γ can be obtained by fitting the model given by equation (5.2) to an image of a single atom obtained by averaging and rescaling MS simulations for an appropriate range of thickness. For all atoms of the nanocluster contributing to the image, the intensity at the pixel (x_k, y_l) at tilt angle θ^j is then given by:

$$f_{kl}^j = \sum_{i=1}^N (f_{kl}^j)^i \quad (5.3)$$

5.3 Statistical measurement precision

In order to derive an expression for the attainable precision of a set of images acquired with ADF STEM, we will proceed in the same way as the derivation shown in section 3.3. For that, consider a set of stochastic observations w_{kl}^j , $k = 1, \dots, K$, $l = 1, \dots, L$, and $j = 1, \dots, J$. Then the vector \mathbf{w} defined as

$$\mathbf{w} = (w_{11}^1, \dots, w_{KL}^J)^T \quad (5.4)$$

represents the column vector of these observations of dimension $K \times L \times J$, where $K \times L$ correspond to the dimension of each projection image and J corresponds to the number of images in the tilt series. Assuming that the observations are statistically independent and have a Poisson distribution, the probability that the observation w_{kl}^j is equal to ω_{kl}^j is given by

$$\frac{(\lambda_{kl}^j)^{\omega_{kl}^j}}{\omega_{kl}^j!} \exp(-\lambda_{kl}^j) \quad (5.5)$$

with λ_{kl}^j the expected number of detected electrons at pixel (k, l) at tilt angle θ^j for which an expression is given by equation (3.5), where, f_{kl}^j is given by equations (2.42) and (5.3) for the MS and Gaussian methods respectively. When assuming statistically independent observations, the probability $P(\boldsymbol{\omega}; \boldsymbol{\beta})$ that a set of observations is equal to $\boldsymbol{\omega} = (\omega_{11}^1, \dots, \omega_{KL}^J)^T$ is the product of all the

probabilities described by equation (5.5):

$$P(\boldsymbol{\omega};\boldsymbol{\beta}) = \prod_{j=1}^J \prod_{k=1}^K \prod_{l=1}^L \frac{(\lambda_{kl}^j)^{\omega_{kl}^j}}{\omega_{kl}^j!} \exp(-\lambda_{kl}^j). \quad (5.6)$$

This function is the joint probability function of the observations. Since the expectation values depend on the choice of the structure of the object under study, the unknown structure parameters $\boldsymbol{\beta}$ enter $P(\boldsymbol{\omega};\boldsymbol{\beta})$ via λ_{kl}^j .

Suppose that an experiment wants to measure the position parameters $\boldsymbol{\beta} = (\beta_{x1}, \beta_{y1}, \beta_{z1}, \dots, \beta_{xN}, \beta_{yN}, \beta_{zN})$ of a set of N atoms of a nanocluster in a quantitative manner from a set of projection images acquired using tomography experiment. An expression for the elements of the Fisher information matrix $F(p,q)$ can be derived using equations (5.6), (3.9), (3.10), and (3.11)

$$F(p,q) = \sum_{k=1}^K \sum_{l=1}^L \sum_{j=1}^J \frac{1}{\lambda_{kl}^j} \frac{\partial \lambda_{kl}^j}{\partial \beta_p} \frac{\partial \lambda_{kl}^j}{\partial \beta_q}. \quad (5.7)$$

The latter equation (5.7) is derived from the definition of the Fisher information matrix given by equation (3.9) using the knowledge of the joint probability density function of the observations. This joint probability density function and the expectation values of the observations are the only requirements to be able to compute the ultimate precision for locating the atoms in 3D. The derivative of λ_{kl}^j with respect to $\boldsymbol{\beta}$ in equation (5.7) may be calculated from the parametric model of the intensity observations described in sections 3.2 and 5.2. For the MS method, this derivative needs to be computed numerically, as was discussed in section 3.3.2.2. Unlike the MS method, the derivatives can be calculated analytically for the GAM (see appendix B.2) leading to analytical expression that can be used as a rule of thumb. Following the approach of [Van Aert et al., 2002b], it can be demonstrated (see appendix B.3) using equations (5.1), (5.2), and (5.7) that the attainable precision of the x -, y -, and z -coordinate of a single atom modelled as a Gaussian function equals:

$$\begin{aligned} \sigma_{x0}^2 = \sigma_{z0}^2 &\approx \frac{r^2}{\gamma N_p} \\ \sigma_{y0}^2 &\approx \frac{r^2}{2\gamma N_p} \end{aligned} \quad (5.8)$$

where $\left(\frac{r^2}{2\gamma}\right)^{1/2}$ corresponds to the Gaussian width of equation 5.2, r equals the atomic radius, γ is a constant dependent on the atom type, and N_p is the total

number of detected electrons dose. This total electron dose equals:

$$N_p = \pi J \frac{Z^\zeta \gamma^2}{\gamma \Delta x \Delta y}$$

where J denotes the number of projections, Z the atomic number, ζ a scattering constant depending on the collection angle of the detector, and Δx and Δy the pixel size in x - and y -direction. For larger clusters, the attainable precision σ of the central atom along the x -, y -, and z -coordinate can be predicted as a function of the precision for one atom given by equation (5.8). This predicted precision can be calculated as follows (for demonstration, see appendix B.3):

$$\begin{aligned} \sigma_x &= \kappa_x d^{\xi_x} + \sigma_{x0} \\ \sigma_y &= \kappa_y d^{\xi_y} + \sigma_{y0} \\ \sigma_z &= \kappa_z d^{\xi_z} + \sigma_{z0} \end{aligned} \quad (5.9)$$

where σ_{x0} , σ_{y0} , and σ_{z0} are the precision of the x -, y -, and z -coordinate of one single atom (cluster diameter equal zero) given by equation (5.8); d correspond to the cluster diameter; and the constant values $\kappa_x = 0.1831$, $\kappa_y = 0.09425$, $\kappa_z = 0.1486$, $\xi_x = 0.6328$, $\xi_y = 0.6628$, and $\xi_z = 0.6637$ were obtained by fitting equation 5.9 to the results of the GAM show in figure 5.2.

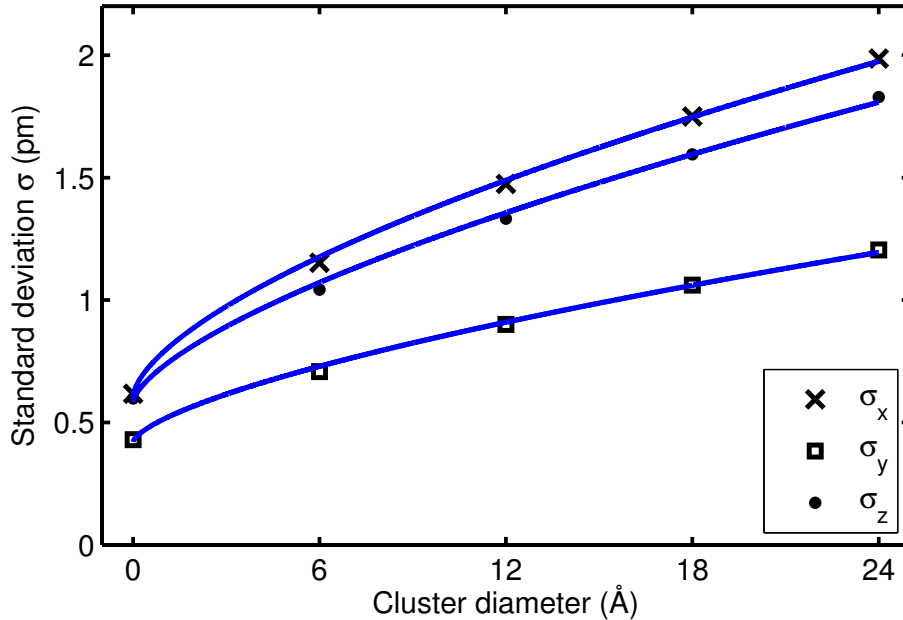


Figure 5.2: The precision σ of the x -, y -, and z -coordinate for locating the central atom in a nanocluster as a function of the cluster diameter using equation 5.9.

Table 5.1: Overview of simulation settings.

Parameter	Symbol	Value
Slice thickness	ε (Å)	2.0
Debye-Waller factor	DWf (Å ²)	0.63
Acceleration voltage	E_0 (kV)	300
Defocus	Δf (Å)	-88.74
Spherical aberration	C_3 (mm)	0.04
Convergence angle	α_0 (mrad)	21.06
FWHM of the source image	(Å)	0.7
Pixel size (STEM image)	Δx (Å)	0.15
Pixel size to sample atomic potential	(Å)	0.032
Beam current	I (pA)	10
Dwell time	τ (μ s)	2
Incident electron dose	($e^-/\text{Å}^2$)	5555

5.4 Simulation settings

Simulations for four gold nanoclusters of different sizes have been performed as illustrated in Figure 5.3. The bulk structure of gold is an FCC structure. However, for small nanoclusters, the atomic structure deviates from this ideal FCC lattice. In this chapter, nanoclusters with a Mackay icosahedral morphology have been considered [Mackay, 1962]. The interatomic distance in these nanoclusters equals 3.0 Å. As discussed in section 5.2, both the MS method and a GAM have been used to simulate tilt series of images. The expression of the GAM is given by equation (5.3), where an expression for the fractional intensities f_{kl}^j of single atoms is given by equation (5.2). Numbers for the parameters ζ and γ are obtained by fitting this expression to an image of a single atom inferred from averaging and rescaling the MS simulated images of the central column of the four clusters along the [001] zone axis. Use has been made of the STEMSIM program [Rosenauer and Schowalter, 2008, Rosenauer et al., 2008] to perform MS calculations under the absorptive potential approximation. Furthermore, the finite source size is modelled by convolving the resulting image with a Gaussian distribution. The settings used for the MS simulations are summarised in table 5.1; where the Scherzer settings have been chosen for the spherical aberration and defocus [Scherzer, 1949, Weyland and Muller, 2005].

For each simulated image of the electron tomography tilt series, a super cell is created of which the dimension in the x - and y -direction equals the diameter of the nanocluster under consideration plus 10 Å extra to avoid wrapping around effects. The dimension in the z -direction equals the diameter of the cluster.

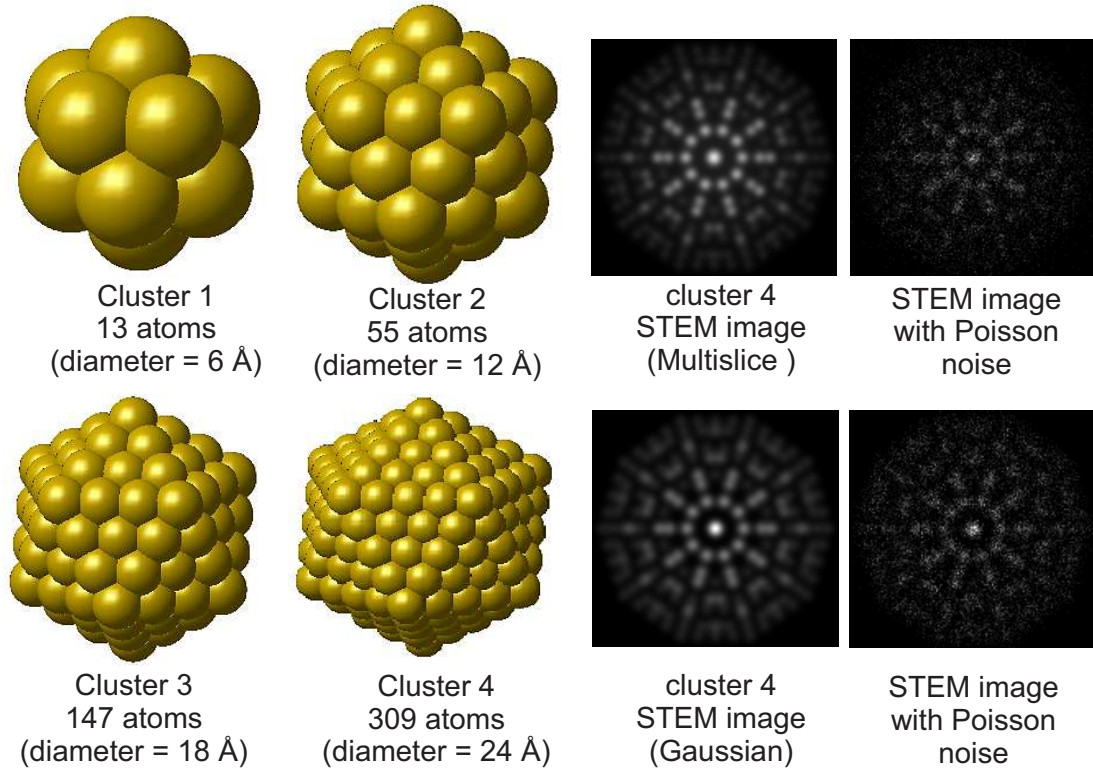


Figure 5.3: The four smallest gold nanoclusters with icosahedral structure and a comparison between the GAM and MS simulation without and with Poisson noise.

5.5 Results and discussion

5.5.1 Calculation of the attainable precision

In this subsection, we will discuss and describe the steps followed to quantify the attainable precision of the 3D atomic position coordinates of the central atom inside a gold nanocluster. The attainable precision, i.e the lower bound on the standard deviation σ , is given by the diagonal elements of the inverse Fisher information matrix F , given by equation (5.7). From this expression, it is clear that the elements of the Fisher information matrix have to be calculated by using the derivatives of the parametric models for the intensity observations λ_{kl}^j with respect to the 3D atomic coordinates. The parametric models for the intensity observations λ_{kl}^j are given by the simulated 2D projection images using either the GAM or the MS simulations. For the GAM, these derivatives can be calculated analytically, since this model is parametric in the atomic coordinates. However, for the MS simulations, the derivative cannot be calculated analytically, since the simulation results from a numerical solution of the high energy Schrödinger equation. In order to calculate the partial derivative for the MS

method, equation (3.15) has to be used. The calculation of all the derivatives for a nanocluster of N atoms for J tilt angles thus requires $J(3N+1)$ simulations.

In order to test if the number of simulations needed for the calculation of the Fisher information matrix can be reduced, the GAM will be used. This will be discussed in subsection 5.5.2. Furthermore, the optimal tilt range and the optimal number of projections will be evaluated for the GAM in subsections 5.5.3 and 5.5.4. Next, in subsections 5.5.5 and 5.5.6, MS simulations will be used in order to determine the optimal detector angles of the annular STEM detector and the attainable precision for locating the central atom of the four nanoclusters. After that, in subsection 5.5.7, the method is applied for the determination of the minimally required electron dose in order to attain a pre-specified precision to locate the atoms in 3D. Finally, the effect of the source size and the Debye-Waller factor on the precision will be studied in subsections 5.5.8 and 5.5.9 respectively.

5.5.2 Determination of the number of simulations for the computation of the attainable precision

In this subsection, the attainable precision for locating atoms of a nanocluster in 3D is evaluated as a function of the number of parameters that is included in the calculation of the Fisher information matrix. From equation (5.7), it can be seen that the calculation of the Fisher information matrix requires the derivatives of the expectation model λ_{kl}^j with respect to all the position coordinates of the atoms of the nanocluster, i.e. $\boldsymbol{\beta} = (\beta_{x1}, \beta_{y1}, \beta_{z1}, \dots, \beta_{xN}, \beta_{yN}, \beta_{zN})$. The number of derivatives therefore equals $J(3N+1)$ where N denotes the number of atoms in the cluster. Here, we investigate if the attainable precision is affected when the number of parameters is reduced. It is important to note that the inverse of the Fisher information matrix does not equal the inverse of the elements of the Fisher information matrix, especially in the presence of significant correlations between the parameters. This means that the attainable precision of e.g. the central atom is influenced by the presence of neighbouring atoms. In practice, this means that e.g. the precision of the central atom will be lower when the exact location of the other atoms is unknown and should be estimated simultaneously. In order to investigate the importance of the number of parameters for the attainable precision for locating the central atom of a nanocluster, the attainable precision will be computed using three different approaches:

1. using all the atoms: the derivatives with respect to all the position coordinates as described by equation (5.7) are calculated,
2. using the atoms of the central plane (orange atoms in figure 5.1): the derivatives with respect to the position coordinates of the atoms of the

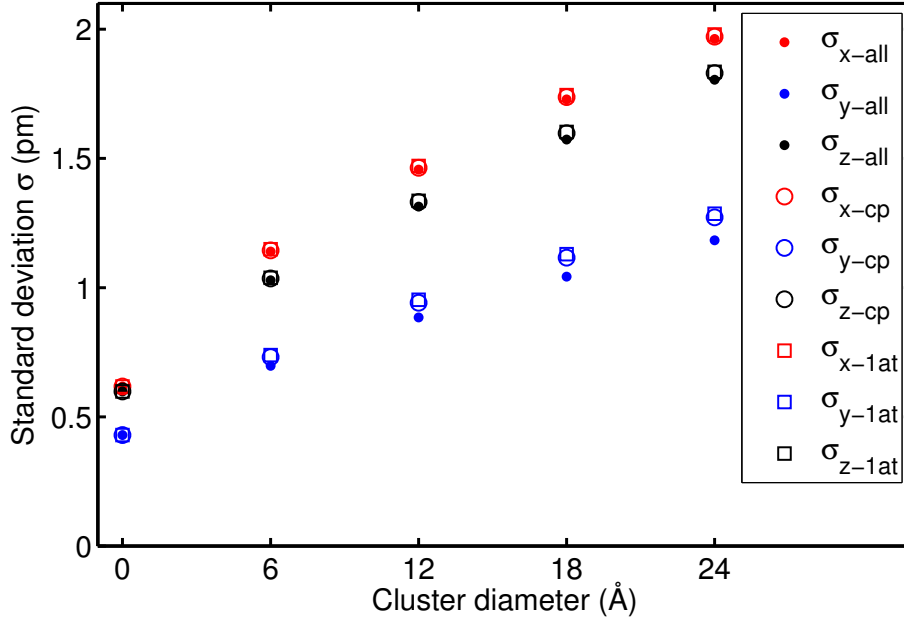


Figure 5.4: The precision σ of the x -, y -, and z -coordinate for locating the central atom in a nanocluster as a function of the cluster diameter using all the atoms (all), the atoms of the central plane (cp), or the central atom only (1at) based on simulations using the GAM for 31 projection images over a tilt range of $[-90,90]$ degrees, and an electron dose of $5555 e^-/\text{\AA}^2$ per image.

central plane, i.e. parallel to the incident beam and perpendicular to the rotation axis, are calculated,

3. using the central atom only (red atom in figure 5.1): the derivatives with respect to the x -, y -, and z -coordinate of the central atom are computed.

The CRLB has been computed for these three different approaches using the GAM for 31 projection images over a tilt range of $[-90,90]$ degrees. An incident electron dose of $5555 e^-/\text{\AA}^2$ per image will be used, which corresponds to a beam current of 10 pA, a pixel dwell time of $2 \mu s$, and a pixel size of 0.15\AA . The results for the precision are shown in figure 5.4 as a function of the cluster diameter. Note that the values for the precision for 1 atom (cluster diameter equal to 0) in this figure can be approximated by the rule of thumb given by equation (5.8) and that the precision as a function of the cluster diameter can be approximated by equation (5.9). From this figure, it can be seen that the precision is not significantly affected when reducing the number of parameters for the calculation of the Fisher information matrix. Therefore, it is allowed to use only the central atom, i.e. the derivatives with respect to the position coordinates of the central atom, in order to evaluate the attainable precision. Throughout the rest of this chapter, the precision will therefore be calculated

using the derivatives with respect to the position coordinates of the central atom only. This means that the number of simulations needed for the numerical approximation of the derivatives of the Fisher information matrix when computing the precision for the MS simulations can be reduced drastically from $J(3N + 1)$ to $4J$.

5.5.3 The optimal angular tilt range

In this subsection, the lower bound on the standard deviation for locating the central atom of a nanocluster in 3D is evaluated for different tilt ranges for a fixed number of projection images, such that the total electron dose is kept constant. Due to the rotation of the nanocluster, the precision with which the atoms can be located in the z -direction will improve. Therefore, it is important to evaluate the attainable precision as a function of the tilt range of the nanocluster. In figure 5.5, the precision σ of the x -, y -, and z -coordinate for locating the central atom is shown as a function of the angular tilt range for a fixed number of 31 projection images and an incident electron dose of $5555 e^-/\text{\AA}^2$ per image. From this figure, we can see that the precision for locating the atoms in the z -direction improves significantly when increasing the angular tilt range. As expected, the precision for locating the atoms in the y -direction does not change significantly when increasing the angular tilt range. For the precision for locating the atoms in the x -direction, a small decrease in precision is observed, i.e. the standard deviation increases, when increasing the tilt range. This can be derived from the fact that when rotating the cluster around the y -axis, information on the z -coordinate will be gained, but some information on the x -coordinate will be lost when keeping a fixed number of projection images. This can be understood better as follows. If you have included in this tilt series of 31 images, the projection images from the structure tilted over -90 and $+90$ degrees, there is no information on the x -coordinate available in these 2 projection images. Therefore, the precision with which the x -coordinate can be measured from the whole tilt series decreases as compared to a tilt series with the same number of projection images and a smaller tilt range. Based on the results of the analysis presented in figure 5.5, an angular tilt range of at least $[-70,70]$ degrees can be suggested. This corresponds to the standard tilt range for conventional tomography experiments.

5.5.4 The optimal number of projection images

In this subsection, the lower bound on the standard deviation for locating the central atom of a nanocluster in 3D is evaluated as a function of the number of projections. In figure 5.6, the result is shown for a nanocluster with 309 atoms using a tilt range of $[-90,90]$ degrees. The nanocluster was tilted in this range with a constant tilt increment for each number of projection images. An electron

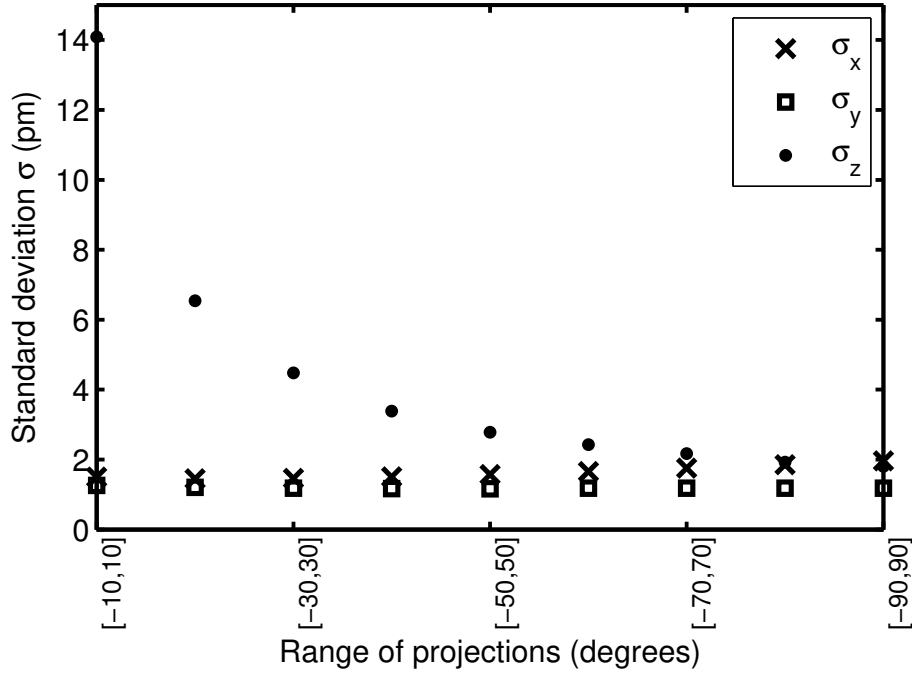


Figure 5.5: The precision σ of the x-, y-, and z-coordinate as a function of the angular tilt range for locating the central atom of a nanocluster with 309 atoms based on simulations using the GAM using a fixed number of 31 projection images for an incident electron dose of $5555 e^-/\text{\AA}^2$ per image.

dose of $5555 e^-/\text{\AA}^2$ per image has been used for the tilt series of 31 images corresponding to the electron dose that has been used in the previous subsections. For the computation of the precision as a function of the number of projection images, the total incident electron dose has been kept constant, and the electron dose has been rescaled corresponding to the number of projection images. As expected, figure 5.6 shows that the precision improves when increasing the number of projection images. Beyond a certain value, the gain in precision is marginal. Therefore, more than 20 projection images can be suggested as an appropriate values.

5.5.5 The optimal detector range

Using the expression for the CRLB, some settings of the STEM experiment for locating the central atom of a nanocluster in 3D can also be optimised, such as the inner and outer angle of an annular STEM detector [Van Aert et al., 2002b, Gonnissen et al., 2014, De Backer et al., 2015a, Gonnissen et al., 2016]. In order to evaluate the precision as a function of the detector angles of the annular STEM detector, MS simulations have been performed with varying detector angles. From the evaluation of the precision as a function of the outer angle, it

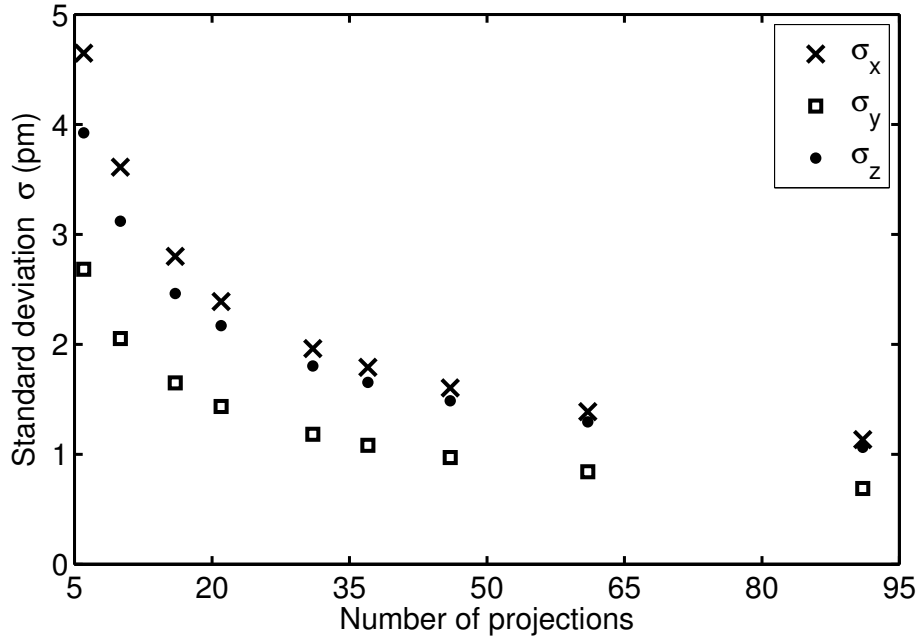


Figure 5.6: The precision σ of the x-, y-, and z-coordinate as a function of the number of projection images for locating the central atom of a nanocluster with 309 atoms based on simulations using the GAM with a tilt range of $[-90,90]$ degrees and a fixed total electron dose.

follows that the optimal outer detector radius should be as large as possible in the experiment. The inner angle has been varied between 15 mrad and 90 mrad. Figure 5.7 shows the precision as a function of the inner detector radius using the MS simulations using 31 projection images, a tilt range of $[-90,90]$ degrees and an electron dose of $5555 e^-/\text{\AA}^2$ per image. The optimal inner angle equals 21 mrad which equals the convergence angle used in the simulations. In this manner, dark field images can be acquired with the highest possible detected dose resulting in the highest attainable precision. It is important to note here that the optimal settings for which the precision is optimal does not necessarily correspond to the experimental settings leading to the highest signal-to-noise ratio or the best image contrast. Here, the evaluation of the precision as a function of the inner detector radius suggests low angle annular dark field STEM imaging. Since in this imaging mode also coherent scattering contributes to the detected signal, this signal will be more sensitive for strain and defects. The here-presented analysis can also be applied to structures including defects and strain as this may have an influence on the choice of the proposed detector settings. Nevertheless, this result, where the optimal inner detector radius is equal to the convergence angle, gives a general guideline for the choice of the inner detector radius.

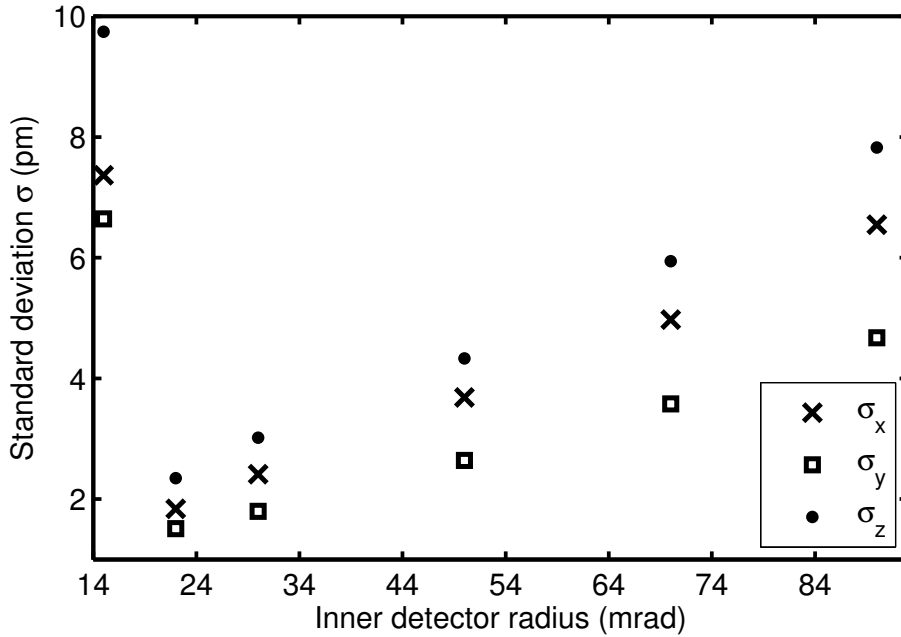


Figure 5.7: The precision σ of the x -, y -, and z -coordinate as a function of the inner detector radius for locating the central atom of a nanocluster with 309 atoms based on MS simulations using 31 projection images, a tilt range of $[-90,90]$ degrees and an incident electron dose of $5555 e^-/\text{\AA}^2$ per image.

5.5.6 The attainable precision for locating the central atom

In order to quantify the attainable precision for a set of realistic experimental settings, we used the suggested values obtained in the previous subsections, i.e. a tilt range of $[-72,72]$ degrees, 25 projection images, an inner detector radius of 21 mrad, and an incident electron dose of $5555 e^-/\text{\AA}^2$ per image. For these settings, MS simulations have been performed for the four gold nanoclusters. These simulations take into account the channelling effects. These channelling effects start to play an important role for the largest clusters and influence the derivatives which are needed for the calculation of the attainable precision. Therefore, using the MS simulations the results for the attainable precision will be more realistic. In figure 5.8, the attainable precision of the x -, y -, and z -coordinate for locating the central atom of a nanocluster in 3D is shown for the experimental settings as a function of the cluster diameter for both the MS simulations and the GAM. From this figure, it is clear that the central atom of a small nanocluster can be located more precisely in 3D than the central atom of a larger nanocluster. Furthermore, it is shown that a precision of a few picometres is feasible in the presence of electron counting noise only. In addition, by comparing the values from the MS simulations and the GAM, it can be concluded that the GAM is a reliable model for evaluating the attainable precision, since the calculated values for the attainable precision based on the GAM and the MS

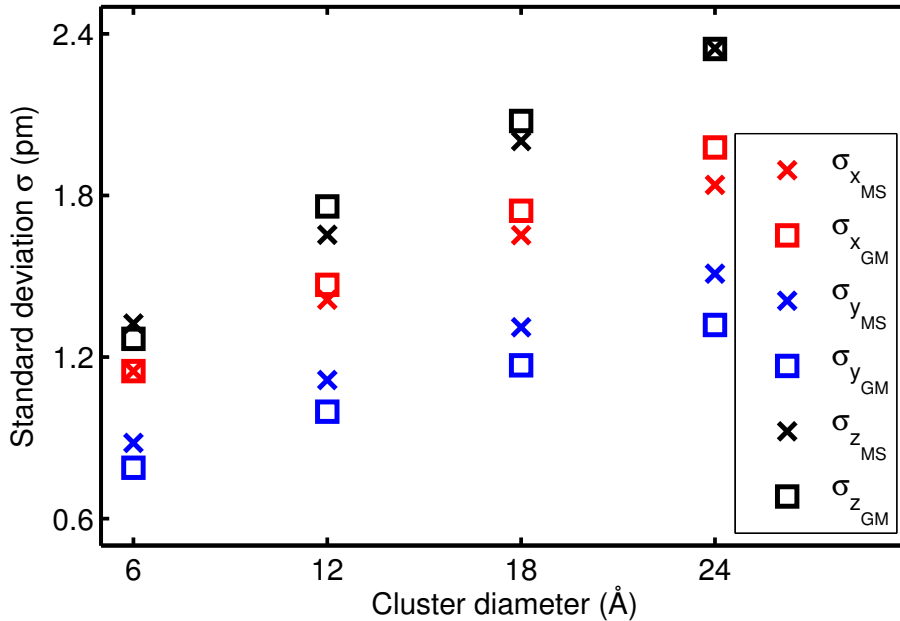


Figure 5.8: The attainable precision σ of the x-, y-, and z-coordinate as a function of the cluster diameter based on realistic MS simulations and the GAM using the suggested experimental settings with 25 projection images over a tilt range of $[-72, 72]$ degrees. A precision of a few picometres is feasible.

method are very comparable. Experimentally, atomic resolution reconstructions have recently been obtained [Van Aert et al., 2011, Bals et al., 2011, Goris et al., 2012, Goris et al., 2015, Xu et al., 2015]. The precision with which the 3D atom coordinates can be measured from these reconstructions is still an open question. In [Xu et al., 2015], it is mentioned that the 3D coordinates of the atoms have been determined with a precision of ≈ 19 pm. Obviously, scan noise, alignment errors, the effect of a sample support, the rearrangement of surface atoms, and others will significantly deteriorate the attainable precision, explaining the lower experimentally obtained precision. However, in this study, the purpose is to investigate the ultimate precision that can be attained. Therefore, it is assumed that scan noise and alignment errors can be avoided or can be corrected for in this analysis [Jones and Nellist, 2013, Yankovich et al., 2014, Jones et al., 2015] and an ideal sample is assumed.

5.5.7 The precision as a function of the incident electron dose

The actual value of the precision does not only depend on the choice of the tilt range, the number of projection images, or the annular STEM detector range, but also on the incident electron dose. In a STEM experiment the number of

electrons per pixel is determined by equation (3.1). In figure 5.9, the precision of the x -, y -, and z -coordinate for locating the central atom of a nanocluster in 3D is shown as a function of the incident electron dose when using 25 projection images over a tilt range of $[-72,72]$ degrees for a nanocluster of 309 atoms based on realistic MS simulations. It is clear from this figure that, as one could expect, the precision increases, i.e. the standard deviation σ decreases, for an increasing electron dose. The precision is proportional to the square root of the incident electron dose ($\sqrt{N_p}$). If a precision of a few picometres is desired, then an electron dose of at least $10^3 \text{ e}^-/\text{\AA}^2$ per image would be necessary. This evaluation can be of great importance if one wants to reduce beam damage but at the same time still obtain an acceptable precision to locate the atoms in 3D.

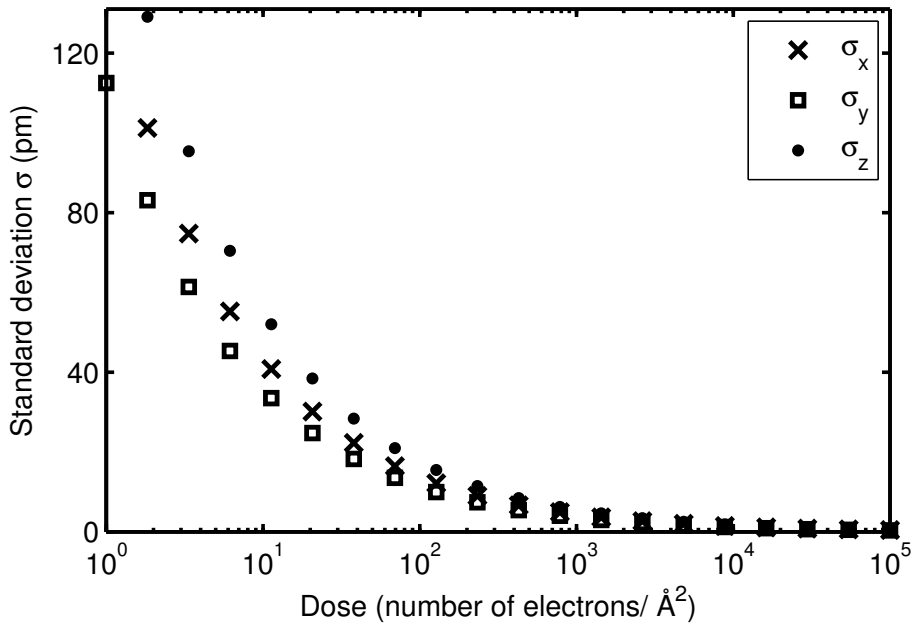


Figure 5.9: The precision σ of the x -, y -, and z -coordinate as a function of the dose per image (number of electrons/ \AA^2) for locating the central atom of a nanocluster with 309 atoms based on realistic MS simulations with 25 projection images over a tilt range of $[-72,72]$ degrees.

5.5.8 The effect of the finite size of the source on the precision

In realistic STEM simulations, the finite size of the source is taken into account by a two-dimensional convolution with the intensity distribution of the source image. This intensity is often modelled as a Gaussian distribution with a FWHM of around 0.7 \AA for an aberration corrected transmission electron microscope [LeBeau et al., 2008, Dwyer et al., 2008]. However, it is known that the shape

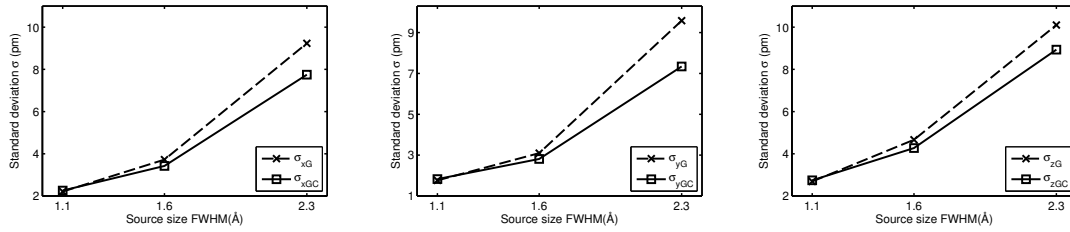


Figure 5.10: The precision σ of the x-, y-, and z-coordinate (from left to right) as a function of FWHM of the source size profile for two different shapes of the source size for locating the central atom of a nanocluster with 13 atoms based on MS simulations using 31 projection images, a tilt range of $[-90,90]$ degrees, an inner detector radius of 21 mrad, and an incident electron dose of $5555 e^-/\text{\AA}^2$ per image. The subscripts G and GC refer to a simple Gaussian distribution and a linear combination of Gaussian and bivariate Lorentzian/Cauchy distribution, respectively, for the source size broadening profile.

of the source image deviates significantly from a Gaussian profile [Dwyer et al., 2010, Verbeeck et al., 2012]. Measurements of the exact shape of the source size distribution show considerable longer tails as compared to a simple Gaussian profile. In order to study the effect of the shape of the source size distribution, the precision has been evaluated for 3 different values of the FWHM taken from Ref. [Verbeeck et al., 2012]. The precision when using a simple Gaussian profile for taking into account source size broadening has been compared with the precision when using a linear combination of a Gaussian and a bivariate Lorentzian/Cauchy distribution. The precision for locating the central atom has been evaluated for a nanocluster of 13 atoms based on realistic MS simulations using 31 projection images, a tilt range of $[-90,90]$ degrees, an inner detector radius of 21 mrad, and an incident electron dose of $5555 e^-/\text{\AA}^2$ per image. As expected, figure 5.10 shows that the precision improves when decreasing the FWHM of the source size. Moreover, this figure shows that when the FWHM of the source size is small that the Gaussian profile is a good approximation for taking into account source size broadening when computing the precision of the central atom of the nanocluster. The source size used in this chapter has a FWHM of 0.7\AA . For this value, we expect that the difference between the two methods is negligible.

5.5.9 The effect of the Debye-Waller factor on the precision

In this section, it is investigated if the assumption of the same Debye-Waller factor for all the atoms of a nanocluster is reasonable while evaluating the precision of the three-dimensional coordinates of the central atom of this nanocluster. For this purpose, the precision of this approach has been compared with the preci-

sion calculated based on MS simulations using a different Debye-Waller factor for each atom. The smallest cluster has been chosen since for this cluster the effect would be the most pronounced. In order to obtain the Debye-Waller factors for each atom of the gold nanocluster with 13 atoms, molecular dynamic (MD) simulations were performed at $T = 300$ K. The simulation has been performed using the LAMMPS software [Plimpton, 1995] and a potential calculated by G. Grochola has been used [Grochola et al., 2005]. Using the root mean square atomic displacements obtained from this MD simulation, the following values for the Debye-Waller factor (\AA^2) could be calculated, where the first value corresponds to the central atom and the other to the surface atoms of this cluster:

	0.59		→ central atom
3.10	3.82	3.91	
3.81	3.29	3.90	→ surface atoms
3.77	3.26	3.82	
3.81	3.92	3.03	

Next, the precision based on the MS simulations with these different Debye-Waller factors for each atom has been calculated for the central atom of the cluster and compared with the precision obtained from the MS simulations with the same Debye-Waller factor (DWF) of 0.63 \AA^2 :

	different DWF	same DWF
σ_x (pm)	1.1801	1.1399
σ_y (pm)	0.7925	0.7735
σ_z (pm)	1.0898	1.0633

From these values it can be concluded that the difference in precision is very small since the Debye-Waller factor of the central atom does not change a lot with respect to the value which is used when using the same Debye-Waller factor for all atoms of the nanocluster.

5.6 Conclusions

In this chapter, the theoretical limits with which the atoms of a nanocluster can be located in 3D based on the acquisition of a tilt series of ADF STEM images was investigated. Using the concept of the CRLB, a theoretical lower bound on the variance, quantitative measurements were obtained for the precision of the x -, y -, and z -coordinate when locating the central atom of a nanocluster in 3D. Furthermore, the here-described method is put forward as a powerful tool that can be used to optimise the design of an experiment. For this goal, the precision

has been evaluated for locating the central atom of a gold cluster as a function of the incident electron dose, the angular tilt range, the number of projection images, the annular STEM detector range, and the cluster diameter. Obviously, the exact optimal experiment design and the exact values for the precision will depend on the material under study. Nevertheless, the conclusions from the study conducted in this chapter give some general guidelines on optimal experiment design for extracting the location of the atoms in 3D using a tilt series of STEM images.

Using approximate STEM simulations, based on a GAM, the calculation of the precision was optimised, since this approach allows a full analytical computation of the precision. This reduces drastically the required number of simulations for the computation of the precision for accurate MS simulations, where the precision is computed numerically. Using the GAM, suggestions for the angular tilt range and number of projection images could be obtained in an efficient and rapid manner. An angular tilt range of at least $[-70,70]$ degrees and a minimal number of 20 projection images was found. In addition, it was shown that the precision for locating the central atom of a nanocluster is better for small nanoclusters. The optimisation of the detector angles requires MS simulations. From this study, it could be concluded that an inner detector radius of the STEM detector equal to the convergence angle is optimal for locating the atoms of a nanocluster in 3D. Furthermore, simulations using the accurate MS method are most appropriate for quantifying the ultimate precision that can be attained. In this chapter, we demonstrated using accurate MS simulations that a precision in the picometre range for locating the atoms in 3D is feasible in the presence of electron counting noise only, assuming ideal experimental conditions. In addition, the general framework presented in this chapter to locate atoms in 3D from a tilt series of images can be applied to any structure of interest, such as more complex structures consisting of more than one atom type.

Chapter 6

Three-dimensional particle reconstruction by depth sectioning in High-Angle Annular Dark-Field Scanning Transmission Electron Microscopy

6.1 Introduction

Thanks to recent progress in aberration-corrected scanning transmission electron microscope (STEM), atomic resolution can nowadays be achieved on a routine basis in two dimensions (2D) in high angle annular dark field (HAADF) STEM enabling structure characterisation and chemical mapping at the atomic scale [Van Aert et al., 2009, Grieb et al., 2013]. However, one should never forget that these results are only 2D projections of a three-dimensional (3D) object. Therefore, electron tomography has evolved into a standard technique to investigate the morphology of nanomaterials. Recently, the resolution was pushed to the atomic level using different techniques. Most of the results were obtained by combining a limited number or a more elaborate tilt series with advanced reconstruction algorithms [Van Aert et al., 2011, Goris et al., 2012, Scott et al., 2012]. Although these approaches enable one to measure atom positions and the chemical nature in nanoparticles atom-by-atom, it is far from straightforward to obtain similar results for samples with a slab-like geometry such as thin films or 2D self-assembled structures. This is related to the increasing projected thickness of the sample when reaching tilt angles higher than e.g. 40° . An alternative technique to visualise the 3D atomic structure is the use of so-called depth sectioning or optical sectioning [van Benthem et al., 2005, van Benthem et al., 2006]. The development of aberration correctors in STEM has indeed led to a considerable reduction in the microscope depth of field, which may be

just a few nanometres. This benefit is explored in depth sectioning where a so-called through-focal series of images of the sample is acquired. Similar as in light microscopy [Wilson, 1990], 3D structural information can then directly be extracted from images recorded at different defocus values or use can be made of more advanced reconstruction algorithms [Van den Broek et al., 2010].

Depth sectioning has successfully been applied to detect individual dopant atoms [van Benthem et al., 2005, van Benthem et al., 2006] or to identify complex dislocations [Hirsch et al., 2013, Yang et al., 2015]. Unfortunately, the vertical probe of size or depth resolution is still the order of several nm. According to [Borisevich et al., 2006, Nellist et al., 2008] the depth resolution (Δz) of HAADF STEM depends on the electron wavelength divided by the square of the semi-aperture angle. This means that the depth resolution can be improved by decreasing the acceleration voltage or by increasing the aperture size. If the acceleration voltage is kept constant, the depth resolution improved as a function of the aperture size as shown in figure 6.1. Although the simulation shows that the depth resolution improves for large aperture sizes, these sizes are still limited to avoid the artifacts that can be created due to aberrations. This means that the depth resolution is still too large to visualise all individual atoms in a nanostructure when using this technique [van Benthem et al., 2006, Xin and Muller, 2009, Cosgriff et al., 2008]. Moreover, non-linear interactions complicate the interpretation [Cosgriff and Nellist, 2007]. However, we show in this chapter that the combination of depth sectioning in HAADF STEM and precise atom-counting [Van Aert et al., 2011, Van Aert et al., 2013, De Backer et al., 2013, De Backer et al., 2015a] can be used to reconstruct nanosized particles in 3D. Indeed, when the number of atoms is measured in each atomic column, the problem of reconstructing the 3D atomic structure can be reduced to determine the depth location of all atomic columns from a through-focal series. The depth locations are then considered as unknown structure parameters which can be determined from a focal series using model fitting. For experimentally acquired images, model fitting never results in a perfect match in the presence of noise and therefore puts a limit to the statistical precision with which the depth location can be estimated.

This chapter is organized as follows. In section 6.2, using the principles of statistical parameter estimation theory explained in chapter 3, an expression is derived for the attainable precision with which the depth location of atoms can be measured. In section 6.3, we will investigate how precise one could locate the individual atoms in 3D when using depth sectioning and what precision can be attained when measuring the depth location of an atomic column with known number of atoms. In section 6.4, a reconstruction algorithm is proposed that can be used to determine the 3D morphology from a focal series of HAADF STEM images. Moreover, a proof of concept is presented where we determine the morphology of a gold nanorod. These results are compared with 3D reconstructions

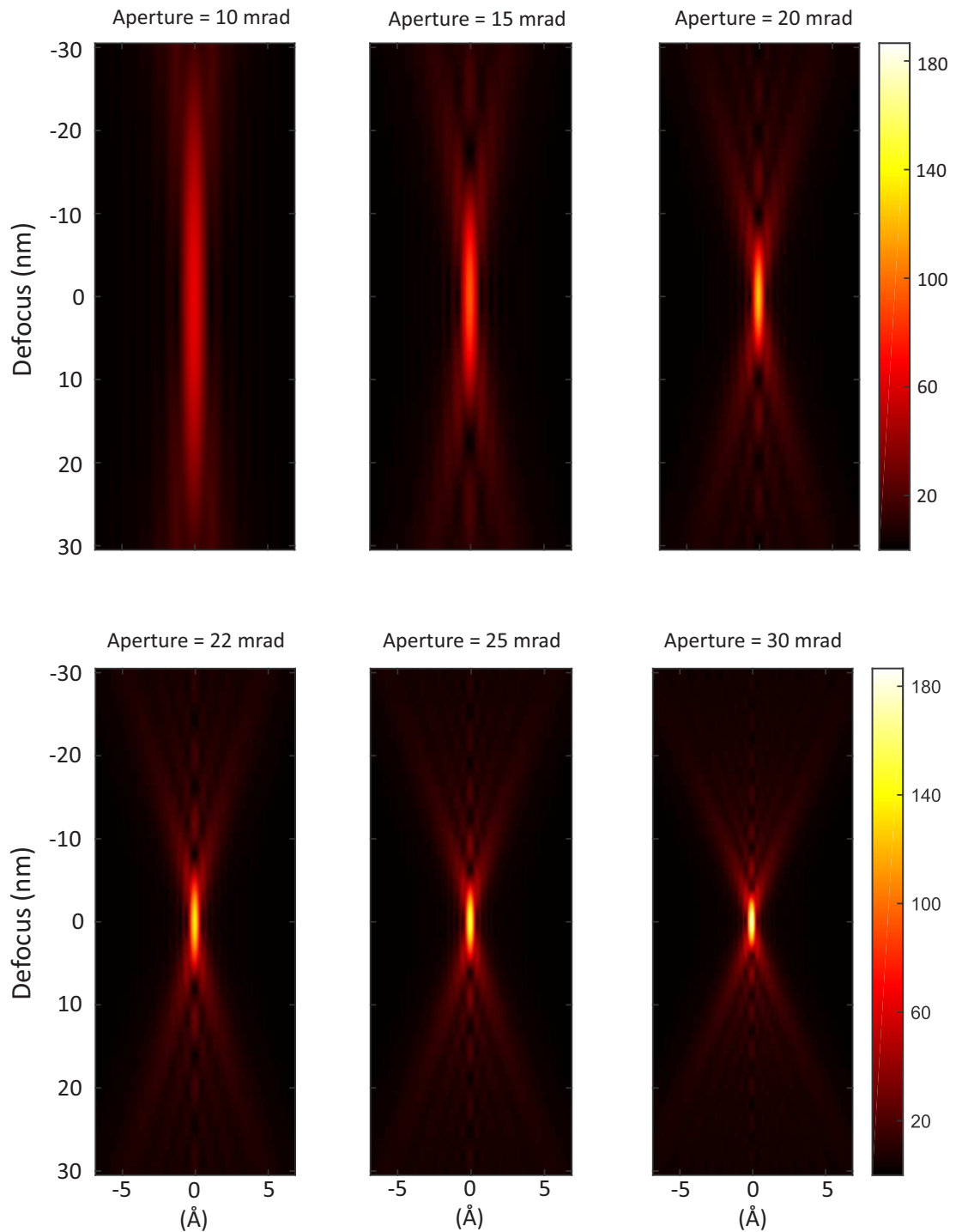


Figure 6.1: Probe intensity profiles as a function of defocus for six different aperture sizes. From this figure, is clear to visualize that the vertical probe size decrease as a function of the aperture-size.

based on projection images acquired along different tilt angles. Finally in section 6.5, conclusions are drawn.

6.2 Statistical measurement precision for the depth location

The mathematical expression for the attainable precision of the depth location, can be derived in the same way as for the tomography experiment explained in chapter 5.3. We consider a set of stochastic observations w_{kl}^j , $k = 1, \dots, K$, $l = 1, \dots, L$, and $j = 1, \dots, J$. The vector \mathbf{w} defined as

$$\mathbf{w} = (w_{11}^1, \dots, w_{KL}^J)^T, \quad (6.1)$$

represents the column vector of these observations of dimension $K \times L \times J$, where $K \times L$ correspond to the dimension of each projection image and J corresponds to the number of images in the focal series. Assuming that the observations are statistically independent and have a Poisson distribution, the probability that the observation w_{kl}^j is equal to ω_{kl}^j is given by

$$\frac{(\lambda_{kl}^j)^{\omega_{kl}^j}}{\omega_{kl}^j!} \exp(-\lambda_{kl}^j) \quad (6.2)$$

with λ_{kl}^j the expected number of detected electrons at pixel (k, l) at defocus Δf^j for which an expression is given by equation (3.5), where, f_{kl}^j is given by equations (2.42).

Suppose that one wants to measure the depth position parameters $\boldsymbol{\beta} = (\beta_{z1}, \dots, \beta_{zN})$ of a set of N atoms of an isolated column in a quantitative manner from a set of projection images acquired using depth sectioning. The elements $F(p, q)$ of the Fisher information matrix may be calculated in the same way as in equation (5.7)

$$F(p, q) = \sum_{k=1}^K \sum_{l=1}^L \sum_{j=1}^J \frac{1}{\lambda_{kl}^j} \frac{\partial \lambda_{kl}^j}{\partial \beta_p} \frac{\partial \lambda_{kl}^j}{\partial \beta_q}. \quad (6.3)$$

6.3 Numerical results

The expression for the CRLB given in chapter 3.3.2 enables one to predict the highest attainable precision with which the individual atoms within an atomic column or the depth location of an atomic column can be estimated. Based on realistic image simulations, one can compute the expectation values λ_{kl}^j and the derivatives with respect to the unknown structure parameters. In this manner,

Table 6.1: Overview of simulation settings.

Parameter	Symbol	Value
Slice thickness	$\varepsilon(\text{\AA})$	4.08
Debye-Waller factor	$DWf(\text{\AA}^2)$	0.63
Acceleration voltage	$E_0(\text{kV})$	300
Defocus range	(\AA)	[-200,200]
Defocus step	(\AA)	10
Number of focal images		41
Spherical aberration	$C_3(\text{mm})$	0
Convergence angle	α_0 (mrad)	21
Detector collection range	(mrad)	[48-180]
FWHM of the source image	(\AA)	0.7
Pixel size (STEM image)	$\Delta x(\text{\AA})$	0.1
Pixel size to sample atomic potential	(\AA)	0.0342
Incident electron dose per image	$(e^-/\text{\AA}^2)$	9612

the elements of the Fisher information matrix can be computed using equation (6.3). Next, the right-hand side of expression (3.13) defines the attainable precision with which the unknown parameters can be estimated.

In this study, the multislice algorithm [Kirkland, 1999] with the inclusion of the frozen phonon approach has been used to compute the expectation values λ_{kl}^j using the MULTEM software [Lobato and Van Dyck, 2015, Lobato et al., 2016]. An isolated column of 10 gold atoms has been assumed, which is aligned along the optical axis and where the distance between the atoms equals 4.08 \AA . The settings used for the multislice simulations are summarised in Table 6.1. Furthermore, the finite source size has been modelled by convolving the resulting image with a Gaussian distribution. Derivatives of λ_{kl}^j with respect to the position coordinates $\beta_{z1}, \dots, \beta_{zN}$ have been computed using the finite difference quotient of equation (3.15) by simulating images with the p -th atom shifted 10 pm ($h = 10$ pm) over and under the nominal position. Figure 6.2 shows (x, z) slices of these derivatives. The attainable precision can now be expressed in terms of the lower bound on the standard deviation $\sigma_{\beta_{zp}}$, which is defined by the square root of the right-hand side of expression (3.13). Table 6.2 summarises the results for each atom in the column. From these numbers, it follows that the standard deviation is only in the nanometre range and consequently the attainable precision is very low. In practice, this means that even under ideal conditions, precise estimates of the positions of individual atoms along the depth direction cannot be expected.

Although the results of Table 6.2 show that precise atomic scale measurements of the displacements of atoms in a nanoparticle in 3D (e.g. due to strain) are not within reach when using depth sectioning, *a priori* information can be introduced

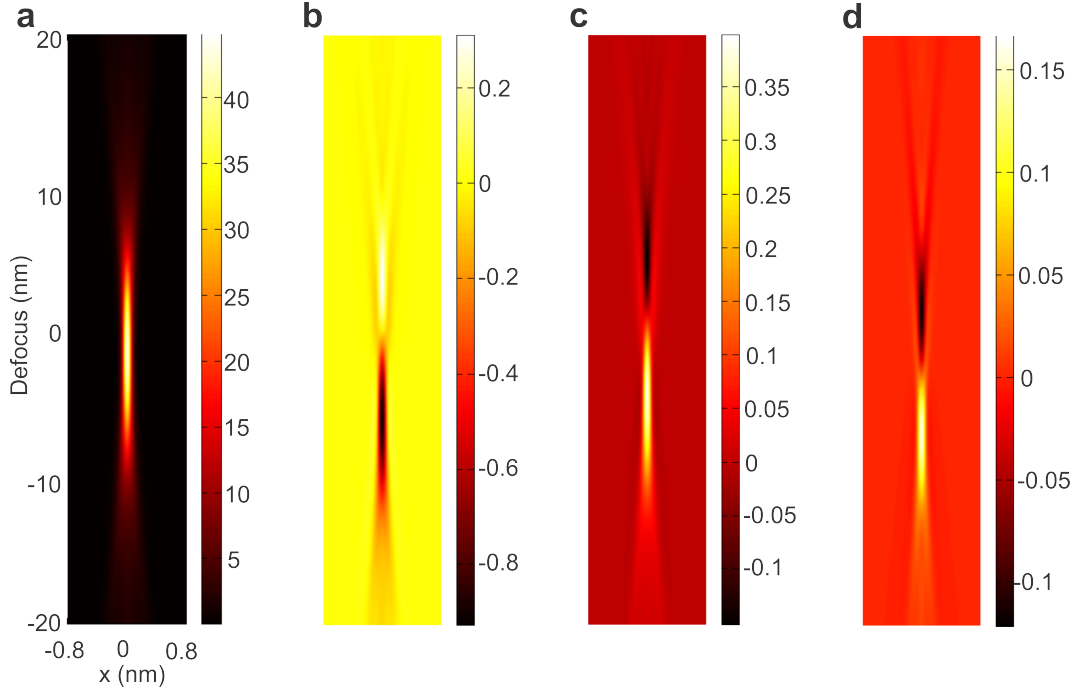


Figure 6.2: Two-dimensional (x,z) depth profile of a simulated focal series of a 10 atoms thick gold column and its derivatives. (a) Simulated focal series λ_{kl}^j . (b) Derivative $\partial\lambda_{kl}^j/\partial\beta_{z1}$ with respect to the first atom. (c) Derivative $\partial\lambda_{kl}^j/\partial\beta_{z2}$ with respect to the second atom. (d) Derivative $\partial\lambda_{kl}^j/\partial\beta_{z7}$ with respect to the seventh atom.

in the estimation problem. When the number of atoms in each atomic column is estimated and if the distance between the atoms is known, the number of unknown parameters is significantly reduced. In this manner, the unknown parameters to be estimated are the depth locations of all atomic columns. For an isolated column, the Fisher information matrix then reduces to a scalar. In a similar manner as before, the lower bound on the standard deviation σ_{β_d} with which the depth location can be estimated has been computed, which is defined by the square root of the right-hand side of expression (3.13). This has been done for an increasing number of gold atoms in a column. The results are shown in figure 6.3 demonstrating that the attainable precision with which the depth

atom number p	1	2	3	4	5	6	7	8	9	10
$\sigma_{\beta_{zp}}$ (nm)	4.10	4.42	4.48	3.70	4.46	4.25	5.81	3.42	5.48	3.06

Table 6.2: Lower bound on the standard deviation $\sigma_{\beta_{zp}}$ of the position coordinate β_{zp} along the depth direction of a 10 atoms thick gold column, where $p = 1$ and $p = 10$ correspond to the atom at the top and at the bottom of the column, respectively.

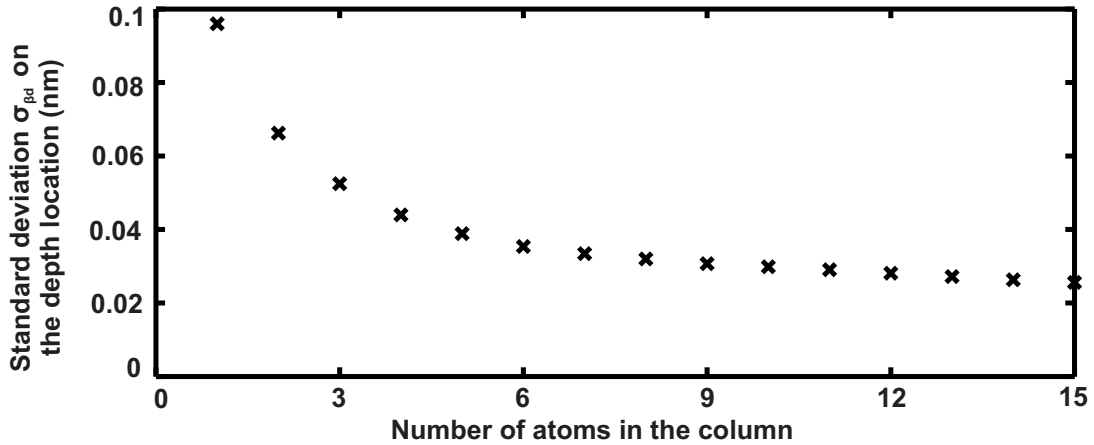


Figure 6.3: Lower bound on the standard deviation σ_{β_d} with which the depth location of an atomic column can be estimated for increasing number of gold atoms in an isolated column.

location of an atomic column can be estimated is in the sub-Å scale and improves with increasing number of atoms in the column.

6.4 3D atomic scale reconstruction of nanosized structures

The results shown in section 6.3 theoretically demonstrate that under realistic experimental conditions, the attainable precision with which individual atoms can be located using depth sectioning is very low. However, when incorporating *a priori* knowledge concerning the number of atoms and the inter-atomic distance, only the depth location needs to be estimated for which a precision in the sub-Å scale is predicted. In this section, an algorithm is presented to actually estimate the depth location of atomic columns for crystals consisting of a single type of element. In this manner, we will reconstruct the 3D morphology of a gold nanorod based on an experimental through-focal series of HAADF STEM images.

6.4.1 Reconstruction algorithm

The reconstruction algorithm can be divided into five steps:

1. A through-focal series of HAADF STEM images is acquired.
2. The images are corrected for drift using an iterative phase-correlation method [Alba et al., 2012]. This results in a corrected 3D stack of images

as shown in figure 6.4a, where the z -axis corresponds to the depth direction. Note that the atomic columns are not resolved in the top image, since this is an out-of-focus image.

3. The 2D x, y -position coordinates and the number of atoms are estimated for each atomic column using StatSTEM [Van Aert et al., 2011, Van Aert et al., 2013, De Backer et al., 2013, De Backer et al., 2015a, De Backer et al., 2016].
4. For each atomic column, the depth location is determined. Therefore, average intensities are first determined for each column as a function of defocus. This is demonstrated in figure 6.4b. Figure 6.4b shows the experimental intensities as a function of defocus averaged around a column position indicated by the red dot in figure 6.4a. This results in the blue crosses shown in figure 6.4b. Next, the peak location is determined by fitting the parameters of a 1-dimensional Gaussian function to these experimental values using the Gauss-Newton method for non-linear least-squares estimation. The estimated Gaussian function is shown in black in figure 6.4b. However, since the peak location does not correspond to the centre of mass of the column, a correction is applied in order to determine the depth location based on a simulated through-focal series using the MULTEM software [Lobato and Van Dyck, 2015, Lobato et al., 2016].
5. Finally, a 3D atomic reconstruction is obtained where the x, y, z -position coordinates of all atoms are relaxed to positions of a known crystallographic structure.

From the description of the reconstruction algorithm, it is clear that the experimental intensities are analysed on an atomic column-by-atomic column basis. It is therefore assumed that the focal series images can be described as a linear superposition of the images of the individual atomic columns. Although cross-talk is not taken into account in this manner, this approximation works well for thin enough samples [Martinez et al., 2014].

6.4.2 Experimental 3D reconstruction of a Au nanorod

Using depth sectioning, the edge of a Au nanorod has been reconstructed in 3D. The shape of the rod is expected to be close to cylindrical with a width of 17.5 nm and a length of 62.2 nm.

Figure 6.4a shows a through-focal series of HAADF STEM images of the tip of the Au nanorod along the $[100]$ zone-axis, which has been acquired using a double aberration corrected cubed FEI Titan electron microscope operated at 300 kV. The experimental settings are as follows: dwell time 10 μ s, pixel size 51 pm, defocus step 1 nm, probe semi-convergence angle 21 mrad, 48-180 mrad

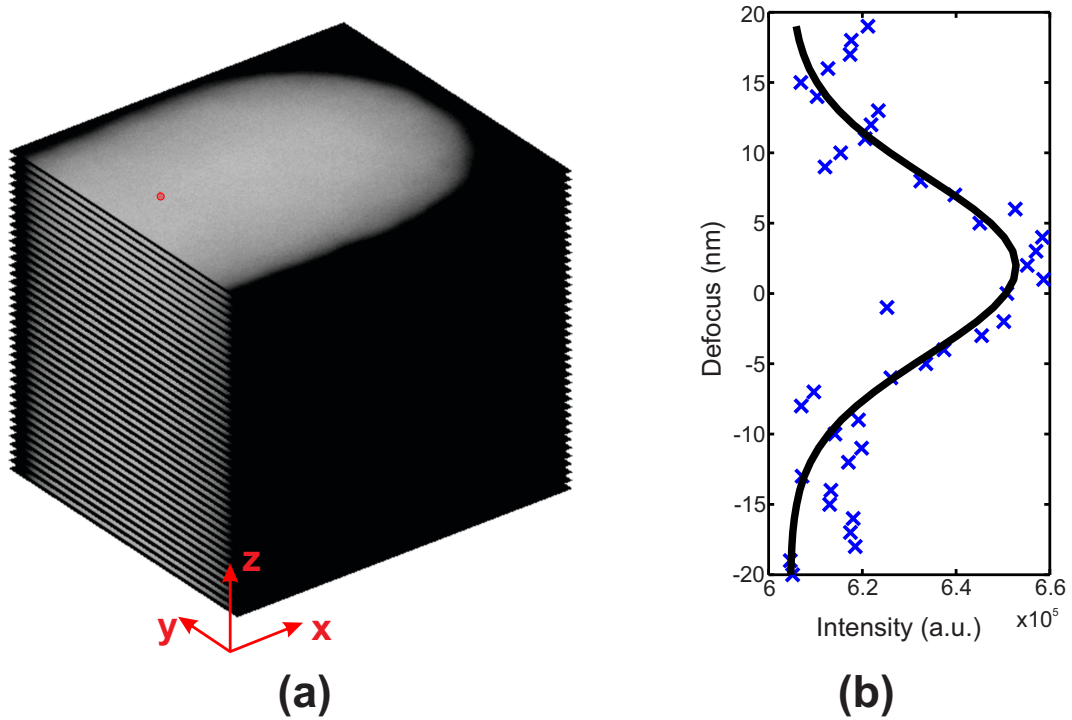


Figure 6.4: Illustration of the different steps used in the reconstruction algorithm. (a) 2D focal series of STEM images of a Au nanorod taken along the [100] zone-axis, where the z -axis corresponds to the depth direction. (b) Experimental intensities averaged around a column position, indicated by the red dot in figure 6.4a, as a function of defocus are shown by means of blue crosses together with a fitted Gaussian function in black to determine the peak location.

detector collection range, and aberrations corrected up to 5th order. It is important to note that the incident electron dose per image is in good agreement with the dose used for the simulations. In addition to the focal series, a single atomic resolution HAADF STEM image has been acquired along the [110] zone-axis and a low magnification HAADF STEM tomography series have been taken in order to validate the 3D atomic reconstruction. The tomography series has been acquired with a tilt range from -74° to $+74^\circ$ and a tilt increment of 2° using a Fischione 2020 single tilt tomography holder. A 3D reconstruction with a resolution in the nanometre range has been obtained using the Simultaneous Iterative Reconstruction Technique (SIRT) implemented in the ASTRA toolbox [van Aarle et al., 2015].

The 3D reconstruction algorithm outlined in section 6.4.1 has been used in order to reconstruct the 3D atomic structure from the experimental focal series. The number of atoms in each atomic column (step 3) has been determined based on so-called scattering cross-sections resulting from the average of 8 central images of the focal series [Van Aert et al., 2011, Van Aert et al., 2013, De Backer et al.,

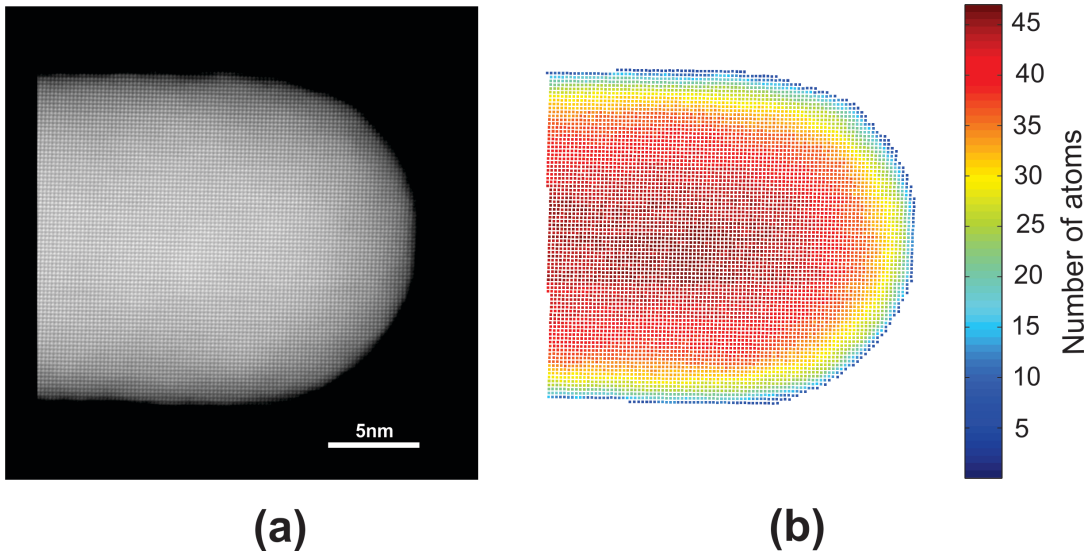


Figure 6.5: (a) Averaged projection image of the Au nanorod determined from the average of the 8 central images of the focal series acquired along the $[100]$ zone axis. (b) Atom-counting results.

2013, De Backer et al., 2015a]. This averaged projection image is shown in figure 6.5(a). The scattering cross-sections, corresponding to the total intensity of electrons scattered by the atomic columns, can indeed be shown to be robust for imaging parameters including defocus [MacArthur et al., 2013] validating this approach. The atom-counting results are shown in figure 6.5(b). Based on these atom counts and assuming that the atoms are located at positions of an FCC structure, the depth location of each atomic column has been determined. The results are summarised in figure 6.4.2. Figures 6.4.2a-c show a projection of the 3D low-resolution tomography reconstruction, a 2D STEM image, and a projection of the 3D depth sectioning reconstruction, respectively, along the $[100]$ zone-axis. In figures 6.4.2d-f, these are shown along the $[110]$ zone-axis. The accuracy of the depth sectioning reconstruction is demonstrated by comparing figure 6.4.2f with figures 6.4.2d and e showing that the overall shape of the particle can be reconstructed. However, local differences as well as non-physical fluctuations at the surface can not be avoided and reflect the limited precision with which the depth location can be determined.

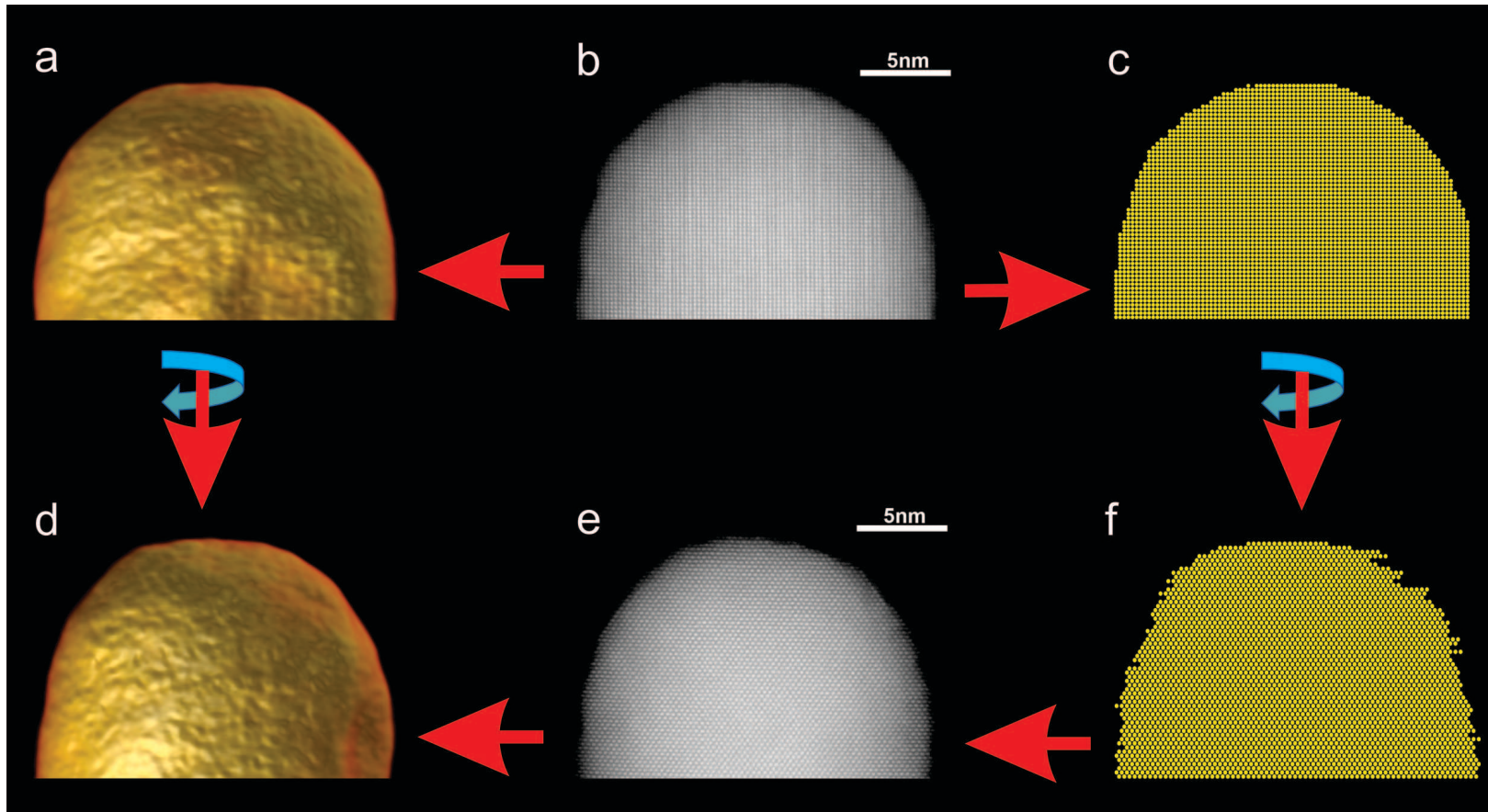


Figure 6.6: (a) 3D low-resolution tomography reconstruction along $[100]$. (b) 2D STEM projection image acquired along a $[100]$ zone-axis. (c) 3D depth sectioning reconstruction viewed along $[100]$, based on a focal series acquired along $[100]$. (d) 3D low-resolution tomography reconstruction along $[110]$. (e) 2D STEM projection image acquired along a $[110]$ zone-axis. (f) 3D depth sectioning reconstruction viewed along $[110]$, based on a focal-series acquired along $[100]$.

6.5 Conclusion

In this chapter, the use of depth sectioning in aberration corrected HAADF STEM for 3D atomic reconstruction has been investigated. Using the concept of the Cramér-Rao lower bound, the attainable precision with which individual atoms can be located along the depth direction has been predicted. It is shown that under realistic conditions, the standard deviation is large as compared to the interatomic distance thus demonstrating that the attainable precision is low. It is expected that this precision improves when using a larger illumination angle on condition that aberration correctors exist that provide a flat phase area of the Ronchigram for this larger convergence angle [Ishikawa et al., 2015]. However, when incorporating knowledge concerning the crystal structure and using quantitative methods enabling one to precisely determine the number of atoms in each atomic column, the problem reduces to locating the depth location of each atomic column. Under realistic experimental settings, the precision with which the depth location can be determined is in the sub-Å range. Based on this observation, a simple but efficient reconstruction algorithm has been proposed and used to experimentally reconstruct the tip of a gold nanorod. In this manner, the 3D shape of the rod could be reconstructed. This work can be considered as a first proof of principle, but we expect that our methodology will be of great value for a broad range of nano-systems including thin films and 2D self-assembled nanomaterials. Recent advances in atom-counting for heterogeneous nanostructures [van den Bos et al., 2016] in combination with the design of new aberration correctors that will allow the use of a larger illumination angle [Ishikawa et al., 2015], will open up new possibilities for measuring 3D surface morphology, thickness, top/surface atomic structures, point defects in bulk materials, and even depth-sensitive spectroscopy for hetero-nanostructures.

Chapter 7

General conclusions

In this thesis, a combination of image simulations and the principles of statistical parameter estimation theory has been proposed in order to retrieve structural information of nanoclusters and nanoparticles from scanning transmission electron microscopy (STEM) images. The aim of statistical parameter estimation theory is to measure, or more correctly, to estimate unknown structure parameters such as the atomic column positions or the number of atoms as accurately and precisely as possible from experimental images. Moreover, this theory can be used to calculate the highest attainable precision with which structure parameters can be estimated. An adequate calculation for this attainable precision is given by the so-called Cramér-Rao lower bound (CRLB), which is a lower bound on the variance of the parameters estimates. Using this concept, the highest attainable precision has been computed to a) locate an atomic column from a two-dimensional (2D) STEM image acquired with a high angle annular dark field (HAADF) detector, b) locate atoms of a nanocluster in three dimensions (3D) from a tilt series of annular dark field (ADF) STEM images, and c) determine the depth location of atoms of an isolated column from a focal-series of images acquired with HAADF STEM. It is important to remark that the lower bound on the variance is independent of the estimation method used. The conclusions from these studies are summarized in the following paragraphs.

One of the most accurate methods to perform STEM image simulations is the multislice (MS) algorithm with the inclusion of the frozen phonon (FP) model. However, the inclusion of the FP model requires repeated MS calculations for several different configurations of the specimen. This process is time-consuming, especially, for simulations involving high angle scattering where a dense sampling is required. An alternative method, which is computationally less intensive and which requires only a single configuration for the specimen, is by including the Absorptive Potential (AP) approximation model into the MS algorithm. One of the most remarkable differences between both methods is that the FP reproduces all the main features of the convergent beam electron diffraction pattern

which is not the case for the AP model. In this thesis, it is investigated if this effect is relevant if the purpose is to quantify specific structure parameters. In chapter 4, both models were compared in terms of the integrated intensity and the attainable precision to locate an atomic column from images acquired with HAADF STEM. This study was carried out for three atom types with weak, medium, and strong scattering factors. The results from this study show that the integrated intensity performed with the AP model is only valid for small detector ranges under low angles and for small thicknesses. The thickness and detector range values depend on the atom types. For high angles of the detector range and thick specimens this model underestimates the intensity. Furthermore, it is shown that the distribution of the intensity over the annular detector is different as compared to the FP model, especially for high angles of the detector and thick specimens. This means that the integrated intensity performed by using the AP model, is not useful due to considerable differences with the FP model. For the comparison of the attainable precision, both methods show a similar behaviour and a precision in the order of the picometre scale. It is important to note that this study was carried out assuming a symmetric annular detector with ideal sensitivity and perfectly aligned atomic columns. For future work, this comparison could be extended by including real detector sensitivity, electron source size broadening, and considering a range of acceleration voltages.

Next, electron tomography performed by high resolution (HR) STEM using a HAADF detector is evolving toward a standard technique which when combined with advanced reconstruction algorithms enables one to visualize atoms. For some nanoparticles, one can even determine the chemical nature atom-by-atom. Once the atoms are resolved in 3D, the next challenge is to refine their positions in a quantitative manner. However, the answer to the question how precise these measurements are, was still open. In this thesis, using the concept of the CRLB, which is a theoretical lower bound on the variance, quantitative measurements were obtained for the precision of the x -, y -, and z -coordinate when locating the central atom of a nanocluster in 3D. The results presented in this thesis were obtained for four small nanoclusters with a diameter size below 2.4 nm showing that the atoms can be located in 3D with a precision in the picometre range. It is important to mention that this method can be applied for any atom of the nanocluster and extended to larger nanoparticles. However, for large nanoparticles the simulations should be performed using the FP model in order to obtain reliable values. Furthermore, using the concept of the CRLB, we demonstrated that some of the experimental settings such as the annular detector range or electron dose can be optimized in order to obtain more precise measurement. The source size effect and the different values of Debye-Waller factor of the atoms only have a minor effect that can be neglected for these nanocluster sizes.

Finally, using the CRLB, it has been found that the attainable precision with which individual atoms can be located along the depth direction under realistic conditions is large as compared to the interatomic distance. However, when incorporating knowledge concerning the crystal structure and using quantitative methods enabling one to precisely determine the number of atoms in each atomic column, the problem reduces to locating the depth location of each atomic column. Under realistic experimental settings, the precision with which the depth location can be determined is in the sub-Å range. Based on this observation, a simple but efficient reconstruction algorithm has been proposed and used to experimentally reconstruct the tip of a gold nanorod. In this manner, the 3D shape of the rod could be reconstructed. This work can be considered as a first proof of principle, but we expect that our methodology will be of great value for a broad range of nanosystems including thin films and 2D self-assembled nanomaterials.

As a general conclusion, it has been shown that the combination of both image simulations and the principles of statistical parameter estimation theory is a useful tool to retrieve quantitative information from STEM experiments. Using this combination, an expression for the theoretical limits with which unknown structure parameters can be estimated, can be found using the concept of the CRLB. Furthermore, this criterion can be put forward as a powerful tool that can be used to optimize the design of a STEM experiment. Although this study is explored from a theoretical point of view, the results can be used as guidelines on optimal experiment design for quantitative electron microscopy.

Appendix A

The effect of the neighbouring columns in the computation of the CRLB

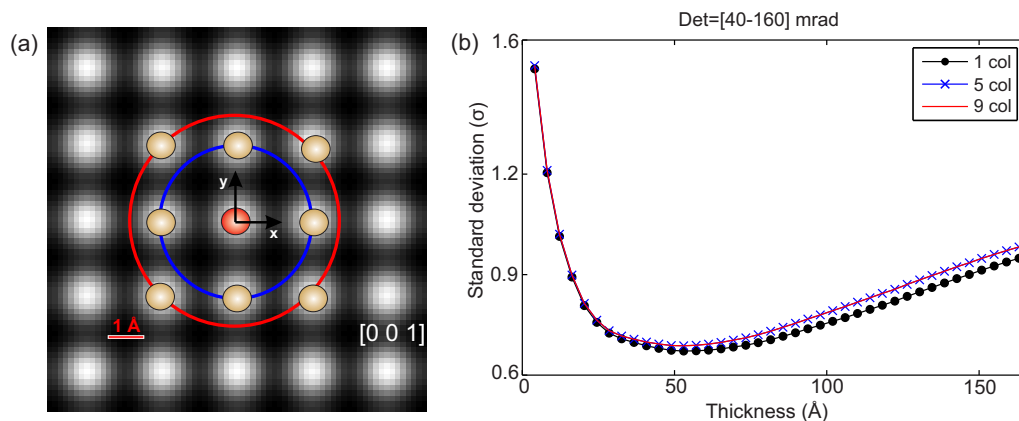


Figure A.1: a) Simulation of an FCC structure of Au atoms along [001] zone-axis for 16.3 nm thick, performed by using MS calculation for 200 FP configuration, and detector range of [40-160] mrad. The blue- and red-line shows the first and second nearest neighbour columns of the centre column (red-sphere) respectively. b) The ultimate precision given by the standard deviation σ to locate the central column shown in figure (a) as a red-sphere as a function of the thickness using the central column only (black-dots), the central column and the first nearest neighbour columns (blue-marks), and the central column plus the first and second nearest neighbour columns (red-line).

The ultimate precision to locate an atomic column in a 2D STEM image of an FCC structure, is affected by the cross-talk of the neighbouring columns. In the computation of the CRLB this means that the ultimate precision can be affected by the covariance between the column under analysis and the neigh-

bouring columns. In order to evaluate this effect, an FCC structure of gold atoms was assumed. The CRLB was computed in three different ways: i) using the atomic column under study only (2×2 Fisher matrix), ii) using the atomic column under study and the first nearest neighbouring columns (10×10 Fisher matrix), and iii) using the atomic column under analysis and the first and second nearest neighbouring columns (18×18 Fisher matrix). The results are shown in figure A.1.

The results were computed from simulations performed for the FP method with 200 phonon configurations, detector range of 40 to 160 mrad and same acceleration voltage and MS inputs given in table 4.1. Figure A.1(b), shows that the covariance does not have a large influence on the results. The black dotted line was computed using a 2×2 Fisher matrix, the blue line with cross marks was computed with a 10×10 Fisher matrix and the red line was computed with a 18×18 Fisher matrix. The difference between the blue and red marks and between the blue and the black marks are very small and can be neglected.

Appendix B

Fisher information matrix for the Gaussian model

B.1 Rotation matrix

The rotation matrix of a point described by the coordinates $(\beta_x, \beta_y, \beta_z)$ over an angle θ about an axis in the direction $\mathbf{u} = (u_x, u_y, u_z)$, where $u_x^2 + u_y^2 + u_z^2 = 1$ is given by

$$R = \begin{bmatrix} \cos\theta + u_x^2(1 - \cos\theta) & u_x u_y(1 - \cos\theta) - u_z \sin\theta & u_x u_z(1 - \cos\theta) - u_y \sin\theta \\ u_y u_x(1 - \cos\theta) + u_z \sin\theta & \cos\theta + u_y^2(1 - \cos\theta) & u_y u_z(1 - \cos\theta) - u_x \sin\theta \\ u_z u_x(1 - \cos\theta) - u_y \sin\theta & u_z u_y(1 - \cos\theta) + u_x \sin\theta & \cos\theta + u_z^2(1 - \cos\theta) \end{bmatrix}. \quad (\text{B.1})$$

The rotated coordinates can be calculated using

$$[\beta_x^j, \beta_y^j, \beta_z^j]^T = R[\beta_x, \beta_y, \beta_z]^T. \quad (\text{B.2})$$

Consider a nanoparticle with N atoms with atomic positions defined by $(\beta_{xi}, \beta_{yi}, \beta_{zi})$ with $i = 1, \dots, N$. Then, the rotated positions for each tilt in a tilt series respect of the y -axis ($\mathbf{u} = (0, 1, 0)$) can be calculated as

$$\begin{bmatrix} \beta_{xi}^j \\ \beta_{yi}^j \\ \beta_{zi}^j \end{bmatrix} = \begin{bmatrix} \cos\theta^j & 0 & \sin\theta^j \\ 0 & 1 & 0 \\ \cos\theta^j & 0 & -\sin\theta^j \end{bmatrix} \begin{bmatrix} \beta_{xi} \\ \beta_{yi} \\ \beta_{zi} \end{bmatrix}, \quad (\text{B.3})$$

where θ^j represents each tilt of a set of J rotations $j = 1, \dots, J$.

B.2 Rotation model for the Gaussian method

Using equations (5.2) and (5.3) the Gaussian model can be written as

$$f(x,y) = \sum_{i=1}^N Z_i^\zeta \exp\left(-\gamma \frac{(x - \beta_{xi})^2 + (y - \beta_{yi})^2}{r_i^2}\right) \Delta x \Delta y \quad (\text{B.4})$$

where (x,y) are the coordinates of the plane, (β_{xi}, β_{yi}) is the position of the i th atom. Furthermore, Δx and Δy are the pixel sizes, γ is an atom type dependent constant, Z_i and r_i are the atomic number and atomic radius of the i th atom, respectively, and ζ is a scattering constant. ζ and γ are constants that can be obtained by fitting. To obtain an expression for the tilt rotations we can replace β_{xi} and β_{yi} with β_{xi}^j and β_{yi}^j given by equation (B.2) into equation (B.4)

$$f^j(x,y) = \sum_{i=1}^N Z_i^\zeta \exp\left(-\gamma \frac{(x - \cos\theta^j \beta_{xi} - \sin\theta^j \beta_{zi})^2 + (y - \beta_{yi})^2}{r_i^2}\right) \Delta x \Delta y \quad (\text{B.5})$$

with j refers to each tilt. From this equation, the derivatives with respect to β_{xi} and β_{yi} can be calculated for each tilt angle.

B.3 Fisher information matrix for the central atom

The ultimate precision with which the x -, y -, and z -coordinates of a single atom can be located from a tilt series of STEM images performed by the Gaussian approximation model can be calculated from a Fisher information matrix of 3×3

$$F = \begin{bmatrix} F(1,1) & F(1,2) & F(1,3) \\ F(2,1) & F(2,2) & F(2,3) \\ F(3,1) & F(3,2) & F(3,3) \end{bmatrix} \quad (\text{B.6})$$

where each element for each tilt is given by equation (5.7). Assuming that the components do not overlap, it can be shown that the non-diagonal elements of F , are approximately equal to zero. On the other hand, it can be shown that the diagonal elements of F are non-zero. Therefore, the inverse of the diagonal elements ($\sigma_x^2 = F^{-1}(1,1)$, $\sigma_y^2 = F^{-1}(2,2)$, and $\sigma_z^2 = F^{-1}(3,3)$) can give us the attainable precision.

Using equation (5.7) and calculating the derivatives from equation (B.5) it can be shown that the element F_{11} is equal to:

$$F(1,1) = \sum_{j=1}^J \cos^2 \theta^j \left(\sum_{k=1}^K \sum_{l=1}^L \frac{1}{\lambda_{kl}^j} \frac{\partial \lambda_{kl}^j}{\partial x} \frac{\partial \lambda_{kl}^j}{\partial x} \right). \quad (\text{B.7})$$

The expression between brackets can be approximated as (see reference [Van Aert et al., 2002a])

$$\sum_{k=1}^K \sum_{l=1}^L \frac{1}{\lambda_{kl}^j} \frac{\partial \lambda_{kl}^j}{\partial x} \frac{\partial \lambda_{kl}^j}{\partial x} \approx \frac{2N_p \gamma}{r^2} \quad (\text{B.8})$$

where, N_p is the total electron dose and $(\frac{r^2}{2\gamma})^{1/2}$ is the width of the Gaussian (γ and r are defined in section B.2). Substituting equation (B.8) in (B.7) the element F_{11} is given by

$$F(1,1) \approx \sum_{j=1}^J \frac{1}{J} \cos^2 \theta^j \left(\frac{2N_p \gamma}{r^2} \right). \quad (\text{B.9})$$

Assuming that the tilt angles $\theta^j, j = 1, \dots, J$ are equidistantly located on the interval $[-\pi/2, \pi/2]$. the difference $\Delta\theta$ between successive tilt angles is equal to:

$$\Delta\theta = \frac{\pi}{J}. \quad (\text{B.10})$$

Substituting $1/J$ for $\Delta\theta/\pi$ in the equation (B.9) give us

$$F(1,1) \approx \left(\frac{2N_p \gamma}{\pi r^2} \right) \sum_{j=1}^J \cos^2 \theta^j \Delta\theta. \quad (\text{B.11})$$

If we consider $\Delta\theta$ very small compared with the interval $[-\pi/2, \pi/2]$, the summation can be approximated by the integral $\int \cos^2 \theta d\theta$. Therefore, the element F_{11} can be approximated as

$$F(1,1) \approx \frac{N_p \gamma}{\pi r^2}. \quad (\text{B.12})$$

By analogous reasoning, it can be shown that the element F_{22} and F_{33} are approximated to

$$\begin{aligned} F(2,2) &\approx \frac{2N_p \gamma}{\pi r^2} \\ F(3,3) &\approx \frac{N_p \gamma}{\pi r^2} \end{aligned} \quad (\text{B.13})$$

Therefore, using the equations B.12 and B.13 an expression for the attainable precision in the three axes is obtained.

$$\sigma_x^2 = \sigma_z^2 = \frac{r^2}{N_p \gamma}; \quad \sigma_y^2 = \frac{r^2}{2N_p \gamma}. \quad (\text{B.14})$$

The expression for total electron dose N_p can be calculated as

$$N_p = \pi J \left(\frac{Z^\zeta}{\gamma} \right) \left(\frac{r^2}{\Delta x \Delta y} \right) \quad (\text{B.15})$$

where, J is the number of projections, Z is the atomic number, ζ is scattering constant depending on the collection angle of the detector and $\Delta x, \Delta y$ are the dimensions of the pixel size. The substitution of equation B.15 in equation B.14 can rewrite the precision as

$$\sigma_x^2 = \sigma_z^2 = 2\alpha \left(\frac{1}{Z^\zeta} \right); \sigma_y^2 = \alpha \left(\frac{1}{Z^\zeta} \right) \quad (\text{B.16})$$

with $\alpha = \frac{\Delta x \Delta y}{2\pi J}$.

In order to find a mathematical expression to predict the precision for higher clusters the data of the figure 5.4 was fitted for the three coordinate axes.

$$\sigma_x = \kappa_x d^{\xi_x} + \sigma_{x0} \quad (\text{B.17})$$

$$\sigma_y = \kappa_y d^{\xi_y} + \sigma_{y0} \quad (\text{B.18})$$

$$\sigma_z = \kappa_z d^{\xi_z} + \sigma_{z0} \quad (\text{B.19})$$

where: σ_{x0} , σ_{y0} , and σ_{z0} are the precision of the x-, y-, and z-coordinate of one single atom (cluster diameter equal zero) giving by the equation (B.14); d correspond to the cluster diameter; and the constant values obtained by the fitting are: $\kappa_x = 0.1831$, $\kappa_y = 0.09425$, $\kappa_z = 0.1486$, $\xi_x = 0.6328$, $\xi_y = 0.6628$, and $\xi_z = 0.6637$

Bibliography

- [Ahmed and Crean, 2014] Ahmed, W. and Crean, S. J. (2014). Nanotechnology for tooth regeneration. *Faculty Dental Journal*, 5(1):32–37. 1, 2
- [Al Dosari and Ayesh, 2013] Al Dosari, H. M. and Ayesh, A. I. (2013). Nanocluster production for solar cell applications. *Journal of Applied Physics*, 114(5):054305. 57
- [Alania et al., 2016a] Alania, M., Altantzis, T., De Backer, A., Lobato, I., Bals, S., and Van Aert, S. (2016a). Depth sectioning combined with atom-counting in HAADF STEM to retrieve the 3D atomic structure. *Ultramicroscopy*. 8, 9, 11
- [Alania et al., 2016b] Alania, M., De Backer, A., Lobato, I., Krause, F., Van Dyck, D., Rosenauer, A., and Van Aert, S. (2016b). How precise can atoms of a nanocluster be located in 3D using a tilt series of scanning transmission electron microscopy images? *Ultramicroscopy*. 11
- [Alba et al., 2012] Alba, A., Aguilar-Ponce, R. M., Viguera-Gómez, J. F., and Arce-Santana, E. (2012). Phase correlation based image alignment with sub-pixel accuracy. In *Mexican International Conference on Artificial Intelligence*, pages 171–182. Springer. 83
- [Alem et al., 2011] Alem, N., Yazyev, O. V., Kisielowski, C., Denes, P., Dahmen, U., Hartel, P., Haider, M., Bischoff, M., Jiang, B., Louie, S. G., et al. (2011). Probing the out-of-plane distortion of single point defects in atomically thin hexagonal boron nitride at the picometer scale. *Physical review letters*, 106(12):126102. 41, 57
- [Allen et al., 2003] Allen, L., Findlay, S., Oxley, M., and Rossouw, C. (2003). Lattice-resolution contrast from a focused coherent electron probe. Part I. *Ultramicroscopy*, 96(1):47–63. 9, 24
- [Alonso, 2011] Alonso, J. (2011). *Structure and Properties of Atomic Nanoclusters*. 57

- [Altantzis, 2015] Altantzis, T. (2015). *Three-Dimensional Characterization of Atomic Clusters, Nanoparticles and their Assemblies by Advanced Transmission Electron Microscopy*. PhD thesis, University of Antwerp. 2, 5, 8
- [Bals et al., 2007] Bals, S., Batenburg, K. J., Verbeeck, J., Sijbers, J., and Van Tendeloo, G. (2007). Quantitative three-dimensional reconstruction of catalyst particles for bamboo-like carbon nanotubes. *Nano Letters*, 7(12):3669–3674. 8
- [Bals et al., 2011] Bals, S., Casavola, M., van Huis, M. A., Van Aert, S., Batenburg, K. J., Van Tendeloo, G., and Vanmaekelbergh, D. (2011). Three-dimensional atomic imaging of colloidal core–shell nanocrystals. *Nano letters*, 11(8):3420–3424. 58, 72
- [Bals et al., 2014] Bals, S., Goris, B., Liz-Marzán, L. M., and Van Tendeloo, G. (2014). Three-dimensional characterization of noble-metal nanoparticles and their assemblies by electron tomography. *Angewandte Chemie International Edition*, 53(40):10600–10610. 8
- [Barth and Kruit, 1996] Barth, J. and Kruit, P. (1996). Addition of different contributions to the charged particle probe size. *Optik*, 101(3):101–109. 34
- [Batson et al., 2002] Batson, P., Dellby, N., and Krivanek, O. (2002). Sub-ångstrom resolution using aberration corrected electron optics. *Nature*, 418(6898):617–620. 13
- [Bethe, 1928] Bethe, H. (1928). Theorie der beugung von elektronen an kristallen. *Annalen der Physik*, 392(17):55–129. 20
- [Bettens et al., 1999] Bettens, E., Van Dyck, D., Den Dekker, A., Sijbers, J., and Van den Bos, A. (1999). Model-based two-object resolution from observations having counting statistics. *Ultramicroscopy*, 77(1):37–48. 59
- [Bock et al., 2013] Bock, H., Carraro, T., Jäger, W., Körkel, S., Rannacher, R., and Schlöder, J. (2013). *Model Based Parameter Estimation: Theory and Applications*. Contributions in Mathematical and Computational Sciences. Springer Berlin Heidelberg. 31
- [Borisevich et al., 2006] Borisevich, A. Y., Lupini, A. R., and Pennycook, S. J. (2006). Depth sectioning with the aberration-corrected scanning transmission electron microscope. *Proceedings of the National Academy of Sciences of the United States of America*, 103(9):3044–3048. 8, 78
- [Burda et al., 2005] Burda, C., Chen, X., Narayanan, R., and El-Sayed, M. A. (2005). Chemistry and properties of nanocrystals of different shapes. *Chemical reviews*, 105(4):1025–1102. 5

- [Carter and Williams, 2016] Carter, C. and Williams, D. (2016). *Transmission Electron Microscopy: Diffraction, Imaging, and Spectrometry*. Springer International Publishing. 8, 9, 32
- [Cha et al., 2007] Cha, J. J., Weyland, M., Briere, J.-F., Daykov, I. P., Arias, T. A., and Muller, D. A. (2007). Three-dimensional imaging of carbon nanotubes deformed by metal islands. *Nano Letters*, 7(12):3770–3773. 8
- [Chalmers et al., 2012] Chalmers, G. R., Bustin, R. M., and Power, I. M. (2012). Characterization of gas shale pore systems by porosimetry, pycnometry, surface area, and field emission scanning electron microscopy/transmission electron microscopy image analyses: Examples from the barnett, woodford, haynesville, marcellus, and doig units. *AAPG bulletin*, 96(6):1099–1119. 7
- [Christodoulou et al., 2007] Christodoulou, J., Suryanarayana, C., Han, B., Lavernia, E., and Newbery, A. (2007). Mechanical alloying and severe plastic deformation. In *Materials Processing Handbook*, pages 13–1. CRC Press. 5
- [Cosgriff et al., 2008] Cosgriff, E., D’Alfonso, A., Allen, L., Findlay, S., Kirkland, A., and Nellist, P. (2008). Three-dimensional imaging in double aberration-corrected scanning confocal electron microscopy, Part I: Elastic scattering. *Ultramicroscopy*, 108(12):1558–1566. 78
- [Cosgriff and Nellist, 2007] Cosgriff, E. and Nellist, P. (2007). A Bloch wave analysis of optical sectioning in aberration-corrected STEM. *Ultramicroscopy*, 107(8):626–634. 78
- [Cowley and Moodie, 1957] Cowley, J. M. and Moodie, A. F. (1957). The scattering of electrons by atoms and crystals. I. A new theoretical approach. *Acta Crystallographica*, 10(10):609–619. 9, 20
- [Crewe et al., 1968] Crewe, A., Wall, J., and Welter, L. (1968). A high-resolution scanning transmission electron microscope. *Journal of Applied Physics*, 39(13):5861–5868. 7
- [Croitoru et al., 2006] Croitoru, M., Van Dyck, D., Van Aert, S., Bals, S., and Verbeeck, J. (2006). An efficient way of including thermal diffuse scattering in simulation of scanning transmission electron microscopic images. *Ultramicroscopy*, 106(10):933–940. 9, 24, 42
- [Curley et al., 2007] Curley, B. C., Johnston, R. L., Young, N. P., Li, Z., Di Vece, M., Palmer, R. E., and Bleloch, A. L. (2007). Combining theory and experiment to characterize the atomic structures of surface-deposited Au₃₀₉ clusters. *The Journal of Physical Chemistry C*, 111(48):17846–17851. 59, 60

- [Davisson and Germer, 1928] Davisson, C. and Germer, L. (1928). Reflection and refraction of electrons by a crystal of nickel. *Proceedings of the National Academy of Sciences*, 14(8):619–627. 6
- [De Backer et al., 2015a] De Backer, A., Gonnissen, J., Van Aert, S., et al. (2015a). Optimal experimental design for nano-particle atom-counting from high-resolution STEM images. *Ultramicroscopy*, 151:46–55. 69, 78, 84, 85
- [De Backer et al., 2015b] De Backer, A., Martinez, G., MacArthur, K., Jones, L., Béché, A., Nellist, P., and Van Aert, S. (2015b). Dose limited reliability of quantitative annular dark field scanning transmission electron microscopy for nano-particle atom-counting. *Ultramicroscopy*, 151:56–61. 43
- [De Backer et al., 2013] De Backer, A., Martinez, G., Rosenauer, A., and Van Aert, S. (2013). Atom counting in HAADF STEM using a statistical model-based approach: methodology, possibilities, and inherent limitations. *Ultramicroscopy*, 134:23–33. 11, 43, 78, 84, 85
- [De Backer et al., 2011] De Backer, A., Van Aert, S., and Van Dyck, D. (2011). High precision measurements of atom column positions using model-based exit wave reconstruction. *Ultramicroscopy*, 111(9):1475–1482. 11
- [De Backer et al., 2016] De Backer, A., van den Bos, K., Van den Broek, W., Sijbers, J., and Van Aert, S. (2016). StatSTEM: An efficient approach for accurate and precise model-based quantification of atomic resolution electron microscopy images. *Ultramicroscopy*, 171:104–116. 84
- [Deepak et al., 2015] Deepak, F., Mayoral, A., and Arenal, R. (2015). *Advanced Transmission Electron Microscopy: Applications to Nanomaterials*. Springer International Publishing. 4, 5, 57
- [den Dekker et al., 2005] den Dekker, A., Van Aert, S., van den Bos, A., and Van Dyck, D. (2005). Maximum likelihood estimation of structure parameters from high resolution electron microscopy images. Part I: a theoretical framework. *Ultramicroscopy*, 104(2):83–106. 11
- [den Dekker et al., 1999] den Dekker, A. J., Sijbers, J., and Van Dyck, D. (1999). How to optimize the design of a quantitative HREM experiment so as to attain the highest precision. *Journal of Microscopy*, 194(1):95–104. 39
- [Drexler, 1986] Drexler, E. (1986). *Engines of Creation: The Coming Era of Nanotechnology*. Anchor Books. 1
- [Dwyer et al., 2008] Dwyer, C., Erni, R., and Etheridge, J. (2008). Method to measure spatial coherence of subangstrom electron beams. *Applied Physics Letters*, 93(2):021115. 73

- [Dwyer et al., 2010] Dwyer, C., Erni, R., and Etheridge, J. (2010). Measurement of effective source distribution and its importance for quantitative interpretation of STEM images. *Ultramicroscopy*, 110(8):952–957. 74
- [Engel and Colliex, 1993] Engel, A. and Colliex, C. (1993). Application of scanning transmission electron microscopy to the study of biological structure. *Current opinion in biotechnology*, 4(4):403–411. 7
- [Ercius et al., 2012] Ercius, P., Xin, H. L., Zheng, H., and Dwyer, C. (2012). Quantitative confocal sectioning in double-corrected STEM utilizing electron energy loss spectroscopy and post-specimen C c correction. *Microscopy and Microanalysis*, 18(S2):1026–1027. 9
- [Erni et al., 2009] Erni, R., Rossell, M. D., Kisielowski, C., and Dahmen, U. (2009). Atomic-resolution imaging with a sub-50-pm electron probe. *Physical Review Letters*, 102(9):096101. 13
- [Ferrando et al., 2008] Ferrando, R., Jellinek, J., and Johnston, R. L. (2008). Nanoalloys: from theory to applications of alloy clusters and nanoparticles. *Chemical reviews*, 108(3):845–910. 4
- [Ferwerda et al., 1986a] Ferwerda, H., Hoenders, B., and Slump, C. (1986a). The fully relativistic foundation of linear transfer theory in electron optics based on the Dirac equation. *Journal of Modern Optics*, 33(2):159–183. 17
- [Ferwerda et al., 1986b] Ferwerda, H., Hoenders, B., and Slump, C. (1986b). Fully relativistic treatment of electron-optical image formation based on the Dirac equation. *Journal of Modern Optics*, 33(2):145–157. 17
- [Frank, 1992] Frank, J. (1992). *Electron Tomography: Three-dimensional Imaging with the Transmission Electron Microscope*. Language of science. Plenum Press. 8
- [Fujiwara, 1961] Fujiwara, K. (1961). Relativistic dynamical theory of electron diffraction. *Journal of the Physical Society of Japan*, 16(11):2226–2238. 17
- [Gao and Peng, 1999] Gao, H. and Peng, L.-M. (1999). Parameterization of the temperature dependence of the Debye-Waller factors. *Acta Crystallographica Section A: Foundations of Crystallography*, 55(5):926–932. 43
- [Gonnissen et al., 2014] Gonnissen, J., De Backer, A., Den Dekker, A., Martinez, G., Rosenauer, A., Sijbers, J., and Van Aert, S. (2014). Optimal experimental design for the detection of light atoms from high-resolution scanning transmission electron microscopy images. *Applied Physics Letters*, 105(6):063116. 69

- [Gonnissen et al., 2016] Gonnissen, J., De Backer, A., den Dekker, A., Sijbers, J., and Van Aert, S. (2016). Detecting and locating light atoms from high-resolution STEM images: The quest for a single optimal design. *Ultramicroscopy*, 170:128–138. 11, 52, 69
- [Goris et al., 2012] Goris, B., Bals, S., Van den Broek, W., Carbó-Argibay, E., Gómez-Graña, S., Liz-Marzán, L. M., and Van Tendeloo, G. (2012). Atomic-scale determination of surface facets in gold nanorods. *Nature materials*, 11(11):930–935. 58, 72, 77
- [Goris et al., 2015] Goris, B., De Beenhouwer, J., De Backer, A., Zanaga, D., Batenburg, K. J., Sánchez-Iglesias, A., Liz-Marzán, L. M., Van Aert, S., Bals, S., Sijbers, J., et al. (2015). Measuring lattice strain in three dimensions through electron microscopy. *Nano letters*, 15(10):6996–7001. 58, 72
- [Grieb et al., 2013] Grieb, T., Müller, K., Fritz, R., Grillo, V., Schowalter, M., Volz, K., and Rosenauer, A. (2013). Quantitative chemical evaluation of dilute GaNAs using ADF STEM: Avoiding surface strain induced artifacts. *Ultramicroscopy*, 129:1–9. 7, 41, 77
- [Grillo, 2009] Grillo, V. (2009). The effect of surface strain relaxation on HAADF imaging. *Ultramicroscopy*, 109(12):1453–1464. 10, 31
- [Grochola et al., 2005] Grochola, G., Russo, S. P., and Snook, I. K. (2005). On fitting a gold embedded atom method potential using the force matching method. *The Journal of chemical physics*, 123(20):204719. 75
- [Gutsch et al., 2005] Gutsch, A., Mühlenweg, H., and Krämer, M. (2005). Tailor-made nanoparticles via gas-phase synthesis. *Small*, 1(1):30–46. 5
- [Gwinn and Vallyathan, 2006] Gwinn, M. R. and Vallyathan, V. (2006). Nanoparticles: health effects: pros and cons. *Environmental health perspectives*, pages 1818–1825. 2
- [Haberland, 2012] Haberland, H. (2012). *Clusters of Atoms and Molecules: Theory, Experiment, and Clusters of Atoms*. Springer Series in Chemical Physics. Springer Berlin Heidelberg. 4
- [Habiba et al., 2014] Habiba, K., Makarov, V. I., Weiner, B. R., and Morell, G. (2014). Fabrication of nanomaterials by pulsed laser synthesis. *Manufacturing Nanostructures, One Central Press, Manchester, UK*. 6
- [Hainfeld and Wall, 1988] Hainfeld, J. F. and Wall, J. S. (1988). High resolution electron microscopy for structure and mapping. In *Biotechnology and the Human Genome*, pages 131–147. Springer. 7

- [Hartel et al., 1996] Hartel, P., Rose, H., and Dinges, C. (1996). Conditions and reasons for incoherent imaging in STEM. *Ultramicroscopy*, 63(2):93–114. 7, 8
- [Hata et al., 2015] Hata, S., Sato, K., Murayama, M., Tsuchiyama, T., and Nakashima, H. (2015). An experimental protocol development of three-dimensional transmission electron microscopy methods for ferrous alloys: Towards quantitative microstructural characterization in three dimensions. *ISIJ International*, 55(3):623–631. 7
- [Hillyard and Silcox, 1995] Hillyard, S. and Silcox, J. (1995). Detector geometry, thermal diffuse scattering and strain effects in ADF STEM imaging. *Ultramicroscopy*, 58(1):6–17. 10, 31
- [Hirsch et al., 2013] Hirsch, P., Lozano, J., Rhode, S., Horton, M., Moram, M., Zhang, S., Kappers, M., Humphreys, C., Yasuhara, A., Okunishi, E., et al. (2013). The dissociation of the [a+ c] dislocation in GaN. *Philosophical Magazine*, 93(28-30):3925–3938. 9, 78
- [Husain and Khan, 2016] Husain, M. and Khan, Z. H. (2016). *Advances in nanomaterials*, volume 79. Springer. 2, 4
- [Ishikawa et al., 2015] Ishikawa, R., Lupini, A. R., Hinuma, Y., and Pennycook, S. J. (2015). Large-angle illumination STEM: toward three-dimensional atom-by-atom imaging. *Ultramicroscopy*, 151:122–129. 88
- [Ishizuka, 2002] Ishizuka, K. (2002). A practical approach for STEM image simulation based on the FFT multislice method. *Ultramicroscopy*, 90(2):71–83. 9, 20, 24, 26, 42
- [Ishizuka and Uyeda, 1977] Ishizuka, K. and Uyeda, N. (1977). A new theoretical and practical approach to the multislice method. *Acta Crystallographica Section A: Crystal Physics, Diffraction, Theoretical and General Crystallography*, 33(5):740–749. 20
- [Jagannathan, 1990] Jagannathan, R. (1990). Quantum theory of electron lenses based on the Dirac equation. *Physical Review A*, 42(11):6674. 17
- [Jagannathan et al., 1989] Jagannathan, R., Simon, R., Sudarshan, E., and Mukunda, N. (1989). Quantum theory of magnetic electron lenses based on the Dirac equation. *Physics Letters A*, 134(8):457–464. 17
- [Jellinek, 1999] Jellinek, J. (1999). *Theory of Atomic and Molecular Clusters: With a Glimpse at Experiments*. Cluster physics. Springer. 4
- [Jellinek, 2008] Jellinek, J. (2008). Nanoalloys: tuning properties and characteristics through size and composition. *Faraday discussions*, 138:11–35. 4

- [Jiang et al., 2007] Jiang, J., Yuan, J., and Bleloch, A. (2007). Cluster scale composition determination in a boron-rich compound. *Applied Physics Letters*, 91(11):113107. 9
- [Jinnai et al., 2000] Jinnai, H., Nishikawa, Y., Spontak, R. J., Smith, S. D., Agard, D. A., and Hashimoto, T. (2000). Direct measurement of interfacial curvature distributions in a bicontinuous block copolymer morphology. *Phys. Rev. Lett.*, 84:518–521. 8
- [Johnston, 2002] Johnston, R. (2002). *Atomic and Molecular Clusters*. Master’s Series in Physics and Astronomy. CRC Press. 4
- [Johnston and Wilcoxon, 2012] Johnston, R. and Wilcoxon, J. (2012). *Metal Nanoparticles and Nanoalloys*. Frontiers of nanoscience. Elsevier. 5
- [Jones, 2016] Jones, L. (2016). Quantitative ADF STEM: acquisition, analysis and interpretation. In *IOP Conference Series: Materials Science and Engineering*, volume 109, page 012008. IOP Publishing. 9
- [Jones and Nellist, 2013] Jones, L. and Nellist, P. D. (2013). Identifying and correcting scan noise and drift in the scanning transmission electron microscope. *Microscopy and Microanalysis*, 19(04):1050–1060. 58, 72
- [Jones et al., 2015] Jones, L., Yang, H., Pennycook, T. J., Marshall, M. S., Aert, S., Browning, N. D., Castell, M. R., and Nellist, P. D. (2015). Smart Align—a new tool for robust non-rigid registration of scanning microscope data. *Advanced Structural and Chemical Imaging*, 1(1):1. 58, 72
- [Kacher et al., 2015] Kacher, J., Cui, B., and Robertson, I. M. (2015). In situ and tomographic characterization of damage and dislocation processes in irradiated metallic alloys by transmission electron microscopy. *Journal of Materials Research*, 30(09):1202–1213. 7
- [Kendall and Stuart, 1967] Kendall, M. and Stuart, A. (1967). *The Advanced Theory of Statistics: Inference and relationship*. Number v. 2 in The Advanced Theory of Statistics. Hafner Pub. Co. 37
- [Khan et al., 2014] Khan, A., Rashid, R., Murtaza, G., and Zahra, A. (2014). Gold nanoparticles: synthesis and applications in drug delivery. *Tropical journal of pharmaceutical research*, 13(7):1169–1177. 5
- [Khanal et al., 2014] Khanal, S., Spitale, A., Bhattarai, N., Bahena, D., Velazquez-Salazar, J. J., Mejía-Rosales, S., Mariscal, M. M., and José-Yacamán, M. (2014). Synthesis, characterization, and growth simulations of Cu–Pt bimetallic nanoclusters. *Beilstein journal of nanotechnology*, 5(1):1371–1379. 4

- [Kirkland, 1999] Kirkland, E. J. (1999). Advanced computing in electron microscopy, earl j. kirkland 1998. plenum press, new york and london. 260 pages. 9, 81
- [Kirkland, 2011] Kirkland, E. J. (2011). On the optimum probe in aberration corrected ADF-STEM. *Ultramicroscopy*, 111(11):1523–1530. 15, 16
- [Kirkland, 2016] Kirkland, E. J. (2016). Computation in electron microscopy. *Acta Crystallographica Section A: Foundations and Advances*, 72(1). 15, 16
- [Kirkland, 2010] Kirkland, J. (2010). *Advanced Computing in Electron Microscopy*. SpringerLink: Springer e-Books. Springer US. 15, 17, 18, 19, 20, 22
- [Kisielowski et al., 2001] Kisielowski, C., Principe, E., Freitag, B., and Hubert, D. (2001). Benefits of microscopy with super resolution. *Physica B: Condensed Matter*, 308:1090–1096. 32
- [Klenov et al., 2007] Klenov, D. O., Findlay, S. D., Allen, L. J., and Stemmer, S. (2007). Influence of orientation on the contrast of high-angle annular dark-field images of silicon. *Physical Review B*, 76(1):014111. 10, 31
- [Knoll and Ruska, 1932] Knoll, M. and Ruska, E. (1932). Beitrag zur geometrischen elektronenoptik. i. *Annalen der Physik*, 404(5):607–640. 6
- [Krivanek et al., 1999] Krivanek, O., Dellby, N., and Lupini, A. (1999). Towards sub-Å electron beams. *Ultramicroscopy*, 78(1):1–11. 16
- [LeBeau et al., 2008] LeBeau, J. M., Findlay, S. D., Allen, L. J., and Stemmer, S. (2008). Quantitative atomic resolution scanning transmission electron microscopy. *Physical Review Letters*, 100(20):206101. 9, 10, 23, 24, 73
- [LeBeau and Stemmer, 2008] LeBeau, J. M. and Stemmer, S. (2008). Experimental quantification of annular dark-field images in scanning transmission electron microscopy. *Ultramicroscopy*, 108(12):1653–1658. 10, 23
- [Lentzen, 2006] Lentzen, M. (2006). Progress in aberration-corrected high-resolution transmission electron microscopy using hardware aberration correction. *Microscopy and Microanalysis*, 12(03):191–205. 7
- [Li et al., 2008] Li, Z., Young, N., Di Vece, M., Palomba, S., Palmer, R., Bleloch, A., Curley, B., Johnston, R., Jiang, J., and Yuan, J. (2008). Three-dimensional atomic-scale structure of size-selected gold nanoclusters. *Nature*, 451(7174):46–48. 9
- [Loane et al., 1991] Loane, R. F., Xu, P., and Silcox, J. (1991). Thermal vibrations in convergent-beam electron diffraction. *Acta Crystallographica Section A: Foundations of Crystallography*, 47(3):267–278. 22

- [Loane et al., 1992] Loane, R. F., Xu, P., and Silcox, J. (1992). Incoherent imaging of zone axis crystals with ADF STEM. *Ultramicroscopy*, 40(2):121–138. 7
- [Lobato, 2014] Lobato, I. (2014). *Accurate modeling of high angle electron scattering*. PhD thesis, University of Antwerp. 17, 18, 19, 20
- [Lobato et al., 2016] Lobato, I., Van Aert, S., and Verbeeck, J. (2016). Progress and new advances in simulating electron microscopy datasets using MULTEM. *Ultramicroscopy*. 27, 81, 84
- [Lobato and Van Dyck, 2015] Lobato, I. and Van Dyck, D. (2015). MULTEM: A new multislice program to perform accurate and fast electron diffraction and imaging simulations using graphics processing units with CUDA. *Ultramicroscopy*, 156:9–17. 27, 81, 84
- [Logsdail, 2013] Logsdail, A. (2013). *Computational Characterisation of Gold Nanocluster Structures*. Springer Theses. Springer International Publishing. 61
- [Louis et al., 2012] Louis, C., Louis, C., and Pluchery, O. (2012). *Gold Nanoparticles for Physics, Chemistry and Biology*. EBL-Schweitzer. Imperial College Press. 5
- [MacArthur et al., 2013] MacArthur, K., Pennycook, T., Okunishi, E., D’Alfonso, A., Lugg, N., Allen, L., Nellist, P., et al. (2013). Probe integrated scattering cross sections in the analysis of atomic resolution HAADF STEM images. *Ultramicroscopy*, 133:109–119. 86
- [MacArthur et al., 2014] MacArthur, K. E., Jones, L. B., and Nellist, P. D. (2014). How flat is your detector? non-uniform annular detector sensitivity in STEM quantification. *Journal of Physics: Conference Series*, 522(1):012018. 10, 31, 43
- [Maccagnano-Zacher et al., 2008] Maccagnano-Zacher, S., Mkhoyan, K., Kirkland, E., and Silcox, J. (2008). Effects of tilt on high-resolution ADF-STEM imaging. *Ultramicroscopy*, 108(8):718–726. 10, 31
- [Mackay, 1962] Mackay, A. (1962). A dense non-crystallographic packing of equal spheres. *Acta Crystallographica*, 15(9):916–918. 64
- [Martin, 2012] Martin, T. (2012). *Large Clusters of Atoms and Molecules*. Nato Science Series E. Springer Netherlands. 4
- [Martinez et al., 2015] Martinez, G., Jones, L., De Backer, A., Béché, A., Verbeeck, J., Van Aert, S., and Nellist, P. (2015). Quantitative STEM normalisation: the importance of the electron flux. *Ultramicroscopy*, 159:46–58. 10

- [Martinez et al., 2014] Martinez, G., Rosenauer, A., De Backer, A., Verbeeck, J., and Van Aert, S. (2014). Quantitative composition determination at the atomic level using model-based high-angle annular dark field scanning transmission electron microscopy. *Ultramicroscopy*, 137:12–19. 84
- [Martínez, 2014] Martínez, G. T. (2014). *Quantitative Model-based High Angle Annular Dark Field Scanning Transmission Electron Microscopy*. PhD thesis, University of Antwerp. 26
- [Marton, 1934] Marton, L. (1934). Electron microscopy of biological objects. *Physical Review*, 46(6):527. 7
- [Midgley et al., 2007] Midgley, P. A., Ward, E. P., Hungría, A. B., and Thomas, J. M. (2007). Nanotomography in the chemical, biological and materials sciences. *Chemical Society Reviews*, 36(9):1477–1494. 8
- [Midgley et al., 2001] Midgley, P. A., Weyland, M., Thomas, J. M., and Johnson, B. F. (2001). Z-contrast tomography: a technique in three-dimensional nanostructural analysis based on Rutherford scattering electronic supplementary information (ESI) available: 3D animations of a Pd–Ru bimetallic catalyst generated from a tomographic reconstruction of HAADF STEM images. see <http://www.rsc.org/suppdata/cc/b1/b101819c>. *Chemical Communications*, (10):907–908. 8
- [Mkhoyan et al., 2008] Mkhoyan, K., Maccagnano-Zacher, S., Kirkland, E., and Silcox, J. (2008). Effects of amorphous layers on ADF-STEM imaging. *Ultramicroscopy*, 108(8):791–803. 10, 31
- [Mock et al., 2002] Mock, J., Barbic, M., Smith, D., Schultz, D., and Schultz, S. (2002). Shape effects in plasmon resonance of individual colloidal silver nanoparticles. *The Journal of Chemical Physics*, 116(15):6755–6759. 4
- [Molière, 1939] Molière, K. (1939). Über den einfluß der absorption auf den brechungseffekt der elektronenstrahlen. II. teil. versuch eines formalen absorptionsansatzes im rahmen der betheschen theorie. *Annalen der Physik*, 426(5):461–472. 24
- [Mood et al., 1974] Mood, A., Graybill, F., and Boes, D. (1974). *Introduction to the Theory of Statistics*. International Student edition. McGraw-Hill. 35
- [Muller et al., 2001] Muller, D. A., Edwards, B., Kirkland, E. J., and Silcox, J. (2001). Simulation of thermal diffuse scattering including a detailed phonon dispersion curve. *Ultramicroscopy*, 86(3):371–380. 22
- [Muller and Mills, 1999] Muller, D. A. and Mills, M. J. (1999). Electron microscopy: probing the atomic structure and chemistry of grain boundaries,

- interfaces and defects. *Materials Science and Engineering: A*, 260(1):12–28. 32
- [Murphy et al., 2008] Murphy, C. J., Gole, A. M., Stone, J. W., Sisco, P. N., Alkilany, A. M., Goldsmith, E. C., and Baxter, S. C. (2008). Gold nanoparticles in biology: beyond toxicity to cellular imaging. *Accounts of chemical research*, 41(12):1721–1730. 5
- [Nellist et al., 2008] Nellist, P., Cosgriff, E., Behan, G., and Kirkland, A. (2008). Imaging modes for scanning confocal electron microscopy in a double aberration-corrected transmission electron microscope. *Microscopy and Microanalysis*, 14(01):82–88. 78
- [Nellist and Pennycook, 1999] Nellist, P. and Pennycook, S. (1999). Incoherent imaging using dynamically scattered coherent electrons. *Ultramicroscopy*, 78(1):111–124. 23
- [Nellist and Pennycook, 2000] Nellist, P. and Pennycook, S. (2000). The principles and interpretation of annular dark-field Z-contrast imaging. *Advances in imaging and electron physics*, 113:147–203. 7, 8
- [Nellist et al., 2004] Nellist, P. D., Chisholm, M. F., Dellby, N., Krivanek, O., Murfitt, M., Szilagy, Z., Lupini, A. R., Borisevich, A., Sides, W., and Pennycook, S. J. (2004). Direct sub-ångström imaging of a crystal lattice. *Science*, 305(5691):1741–1741. 13
- [Notarianni et al., 2014] Notarianni, M., Vernon, K., Chou, A., Aljada, M., Liu, J., and Motta, N. (2014). Plasmonic effect of gold nanoparticles in organic solar cells. *Solar Energy*, 106:23–37. 5
- [O’Keefe et al., 2005] O’Keefe, M. A., Allard, L. F., and Blom, D. A. (2005). HRTEM imaging of atoms at sub-ångström resolution. *Journal of electron microscopy*, 54(3):169–180. 7
- [Olson, 2000] Olson, G. B. (2000). Designing a new material world. *Science*, 288(5468):993–998. 57
- [Pennycook and Jesson, 1991] Pennycook, S. and Jesson, D. (1991). High-resolution Z-contrast imaging of crystals. *Ultramicroscopy*, 37(1):14–38. 24
- [Pennycook and Nellist, 2011] Pennycook, S. and Nellist, P. (2011). *Scanning Transmission Electron Microscopy: Imaging and Analysis*. Springer New York. 7
- [Plimpton, 1995] Plimpton, S. (1995). Fast parallel algorithms for short-range molecular dynamics. *Journal of computational physics*, 117(1):1–19. 75

- [Pokropivny and Skorokhod, 2007] Pokropivny, V. and Skorokhod, V. (2007). Classification of nanostructures by dimensionality and concept of surface forms engineering in nanomaterial science. *Materials Science and Engineering: C*, 27(5):990–993. 2
- [Qi et al., 2010] Qi, T., Grinberg, I., and Rappe, A. M. (2010). Correlations between tetragonality, polarization, and ionic displacement in PbTiO₃-derived ferroelectric perovskite solid solutions. *Physical Review B*, 82(13):134113. 41, 57
- [Rai and Subramanian, 2009] Rai, R. S. and Subramanian, S. (2009). Role of transmission electron microscopy in the semiconductor industry for process development and failure analysis. *Progress in crystal growth and characterization of materials*, 55(3):63–97. 7
- [Rao et al., 2006] Rao, C. N. R., Müller, A., and Cheetham, A. K. (2006). *The chemistry of nanomaterials: synthesis, properties and applications*. John Wiley & Sons. 5
- [Rayleigh, 1879] Rayleigh, L. (1879). XXXI. investigations in optics, with special reference to the spectroscope. *The London, Edinburgh, and Dublin Philosophical Magazine and Journal of Science*, 8(49):261–274. 58
- [Retsky, 1974] Retsky, M. (1974). Observed single atom elastic cross sections in a scanning electron microscope. Technical report, Chicago Univ., Ill.(USA). Dept. of Physics. 43
- [Rez, 1985] Rez, P. (1985). The use of array processors attached to minicomputers for multislice image calculations. *Ultramicroscopy*, 16(2):255–259. 20
- [Rose, 1976] Rose, H. (1976). Nonstandard imaging methods in electron microscopy. *Ultramicroscopy*, 2:251–267. 10
- [Rosenauer et al., 2009] Rosenauer, A., Gries, K., Müller, K., Pretorius, A., Schowalter, M., Avramescu, A., Engl, K., and Lutgen, S. (2009). Measurement of specimen thickness and composition in alxga1-xn/gan using high-angle annular dark field images. *Ultramicroscopy*, 109(9):1171–1182. 10, 26, 43
- [Rosenauer and Schowalter, 2008] Rosenauer, A. and Schowalter, M. (2008). STEMSIM—a new software tool for simulation of STEM HAADF Z-contrast imaging. In *Microscopy of Semiconducting Materials 2007*, pages 170–172. Springer. 27, 29, 64
- [Rosenauer et al., 2008] Rosenauer, A., Schowalter, M., Titantah, J. T., and Lamoen, D. (2008). An emission-potential multislice approximation to simulate thermal diffuse scattering in high-resolution transmission electron microscopy. *Ultramicroscopy*, 108(12):1504–1513. 9, 24, 29, 42, 64

- [Sao-Joao et al., 2005] Sao-Joao, S., Giorgio, S., Pénisson, J.-M., Chapon, C., Bourgeois, S., and Henry, C. (2005). Structure and deformations of Pd- Ni core- shell nanoparticles. *The Journal of Physical Chemistry B*, 109(1):342–347. 4
- [Sawada et al., 2007] Sawada, H., Hosokawa, F., Kaneyama, T., Ishizawa, T., Terao, M., Kawazoe, M., Sannomiya, T., Tomita, T., Kondo, Y., Tanaka, T., et al. (2007). Achieving 63 pm resolution in scanning transmission electron microscope with spherical aberration corrector. *Japanese journal of applied physics*, 46(6L):L568. 13
- [Sawada et al., 2008] Sawada, H., Sannomiya, T., Hosokawa, F., Nakamichi, T., Kaneyama, T., Tomita, T., Kondo, Y., Tanaka, T., Oshima, Y., Tanishiro, Y., et al. (2008). Measurement method of aberration from Ronchigram by autocorrelation function. *Ultramicroscopy*, 108(11):1467–1475. 16
- [Scherzer, 1936] Scherzer, O. (1936). Über einige fehler von elektronenlinsen. *Zeitschrift für Physik*, 101(9-10):593–603. 9
- [Scherzer, 1949] Scherzer, O. (1949). The theoretical resolution limit of the electron microscope. *Journal of Applied Physics*, 20(1):20–29. 64
- [Schmid and Fenske, 2010] Schmid, G. and Fenske, D. (2010). Metal clusters and nanoparticles. 57
- [Scott et al., 2012] Scott, M., Chen, C.-C., Mecklenburg, M., Zhu, C., Xu, R., Ercius, P., Dahmen, U., Regan, B., and Miao, J. (2012). Electron tomography at 2.4-angstrom resolution. *Nature*, 483(7390):444–447. 77
- [Sheppard, 2004] Sheppard, C. J. (2004). Orthogonal aberration functions for high-aperture optical systems. *JOSA A*, 21(5):832–838. 16
- [Simon Kaluza, 2009] Simon Kaluza, Bertrand Honnert, E. J. (2009). *European risk observatory literaure review - Workplace exposure to nanoparticles*. European Agency for Safety and Health at Work. 2
- [Singhal et al., 1997] Singhal, A., Yang, J., and Gibson, J. (1997). STEM-based mass spectroscopy of supported Re clusters. *Ultramicroscopy*, 67(1-4):191–206. 43
- [Spence, 1999] Spence, J. C. (1999). The future of atomic resolution electron microscopy for materials science. *Materials Science and Engineering: R: Reports*, 26(1):1–49. 32
- [Springborg, 2000] Springborg, M. (2000). *Methods of electronic-structure calculations*. Wiley Chichester. 32

- [Takagi, 1958] Takagi, S. (1958). On the temperature diffuse scattering of electrons I. Derivation of general formulae. *Journal of the Physical Society of Japan*, 13(3):278–286. 23
- [Tanaka, 2014] Tanaka, N. (2014). *Scanning Transmission Electron Microscopy of Nanomaterials: Basics of Imaging and Analysis*. World Scientific Publishing Company. 7
- [Tang et al., 2014] Tang, Y., Zhu, Y., Wang, Y., Wang, W., Xu, Y., Ren, W., Zhang, Z., and Ma, X. (2014). Atomic-scale mapping of dipole frustration at 90 [deg] charged domain walls in ferroelectric PbTiO₃ films. *Scientific reports*, 4. 41, 57
- [Taniguchi et al., 1974] Taniguchi, N. et al. (1974). On the basic concept of nanotechnology. In *Proc. Intl. Conf. Prod. Eng. Tokyo, Part II, Japan Society of Precision Engineering*, pages 18–23. 1
- [Thomson, 1928] Thomson, G. (1928). Experiments on the diffraction of cathode rays. In *Proceedings of the Royal Society of London A: Mathematical, Physical and Engineering Sciences*, volume 117, pages 600–609. The Royal Society. 6
- [Tiwari et al., 2012] Tiwari, J. N., Tiwari, R. N., and Kim, K. S. (2012). Zero-dimensional, one-dimensional, two-dimensional and three-dimensional nanostructured materials for advanced electrochemical energy devices. *Progress in Materials Science*, 57(4):724–803. 2
- [Toumey, 2009] Toumey, C. (2009). Plenty of room, plenty of history. *Nature nanotechnology*, 4(12):783–784. 1
- [Tylecote, 1992] Tylecote, R. (1992). A history of metallurgy, the institute of materials. *London: Oxford university*, page p111. 5
- [Utsunomiya and Ewing, 2003] Utsunomiya, S. and Ewing, R. C. (2003). Application of high-angle annular dark field scanning transmission electron microscopy, scanning transmission electron microscopy-energy dispersive X-ray spectrometry, and energy-filtered transmission electron microscopy to the characterization of nanoparticles in the environment. *Environmental Science & Technology*, 37(4):786–791. 7
- [Valcárcel and López-Lorente, 2014] Valcárcel, M. and López-Lorente, Á. (2014). *Gold Nanoparticles in Analytical Chemistry*. Comprehensive Analytical Chemistry. Elsevier Science. 5

- [van Aarle et al., 2015] van Aarle, W., Palenstijn, W. J., De Beenhouwer, J., Altantzis, T., Bals, S., Batenburg, K. J., and Sijbers, J. (2015). The ASTRA Toolbox: A platform for advanced algorithm development in electron tomography. *Ultramicroscopy*, 157:35–47. 85
- [Van Aert, 2003] Van Aert, S. (2003). *Statistical experimental design for quantitative atomic resolution transmission electron Microscopy*. PhD thesis, University of Delf. 39
- [Van Aert et al., 2011] Van Aert, S., Batenburg, K. J., Rossell, M. D., Erni, R., and Van Tendeloo, G. (2011). Three-dimensional atomic imaging of crystalline nanoparticles. *Nature*, 470(7334):374–377. 10, 58, 72, 77, 78, 84, 85
- [Van Aert et al., 2013] Van Aert, S., De Backer, A., Martinez, G., Goris, B., Bals, S., Van Tendeloo, G., and Rosenauer, A. (2013). Procedure to count atoms with trustworthy single-atom sensitivity. *Physical Review B*, 87(6):064107. 11, 43, 78, 84, 85
- [Van Aert et al., 2005] Van Aert, S., Den Dekker, A., Van Den Bos, A., Van Dyck, D., and Chen, J. (2005). Maximum likelihood estimation of structure parameters from high resolution electron microscopy images. Part II: a practical example. *Ultramicroscopy*, 104(2):107–125. 11
- [Van Aert et al., 2002a] Van Aert, S., Den Dekker, A., Van Dyck, D., and Van Den Bos, A. (2002a). High-resolution electron microscopy and electron tomography: resolution versus precision. *Journal of Structural Biology*, 138(1):21–33. 97
- [Van Aert et al., 2002b] Van Aert, S., Den Dekker, A., Van Dyck, D., and Van Den Bos, A. (2002b). Optimal experimental design of STEM measurement of atom column positions. *Ultramicroscopy*, 90(4):273–289. 37, 39, 52, 59, 62, 69
- [Van Aert et al., 2002c] Van Aert, S., den Dekker, A. J., van den Bos, A., and Van Dyck, D. (2002c). High-resolution electron microscopy: from imaging toward measuring. *IEEE Transactions on Instrumentation and Measurement*, 51 (4). 41
- [Van Aert et al., 2009] Van Aert, S., Verbeeck, J., Erni, R., Bals, S., Luysberg, M., Van Dyck, D., and Van Tendeloo, G. (2009). Quantitative atomic resolution mapping using high-angle annular dark field scanning transmission electron microscopy. *Ultramicroscopy*, 109(10):1236–1244. 7, 11, 34, 41, 43, 77
- [van Benthem et al., 2005] van Benthem, K., Lupini, A. R., Kim, M., Baik, H. S., Doh, S., Lee, J.-H., Oxley, M. P., Findlay, S. D., Allen, L. J., Luck,

- J. T., et al. (2005). Three-dimensional imaging of individual hafnium atoms inside a semiconductor device. *Applied Physics Letters*, 87(3):034104. 9, 77, 78
- [van Benthem et al., 2006] van Benthem, K., Lupini, A. R., Oxley, M. P., Findlay, S. D., Allen, L. J., and Pennycook, S. J. (2006). Three-dimensional ADF imaging of individual atoms by through-focal series scanning transmission electron microscopy. *Ultramicroscopy*, 106(11):1062–1068. 9, 77, 78
- [van den Bos, 2007] van den Bos, A. (2007). *Parameter Estimation for Scientists and Engineers*. Wiley. 31, 34, 36, 39, 40
- [van den Bos and den Dekker, 2001] van den Bos, A. and den Dekker, A. (2001). Resolution reconsidered—conventional approaches and an alternative. *Advances in Imaging and Electron Physics*, 117:241–360. 34, 35, 36, 40
- [van den Bos et al., 2016] van den Bos, K. H., De Backer, A., Martinez, G. T., Winckelmans, N., Bals, S., Nellist, P. D., and Van Aert, S. (2016). Unscrambling mixed elements using high angle annular dark field scanning transmission electron microscopy. *Physical Review Letters*, 116(24):246101. 88
- [Van den Broek et al., 2010] Van den Broek, W., Van Aert, S., and Van Dyck, D. (2010). A model based reconstruction technique for depth sectioning with scanning transmission electron microscopy. *Ultramicroscopy*, 110(5):548–554. 78
- [Van Dyck, 1975] Van Dyck, D. (1975). The path integral formalism as a new description for the diffraction of high-energy electrons in crystals. *physica status solidi (b)*, 72(1):321–336. 19
- [Van Dyck, 2009] Van Dyck, D. (2009). Is the frozen phonon model adequate to describe inelastic phonon scattering? *Ultramicroscopy*, 109(6):677–682. 23
- [Van Dyck, 2011] Van Dyck, D. (2011). Persistent misconceptions about incoherence in electron microscopy. *Ultramicroscopy*, 111(7):894–900. 22, 44
- [Van Tendeloo et al., 2012] Van Tendeloo, G., Van Dyck, D., and Pennycook, S. J. (2012). *Handbook of Nanoscience, 2 Volume Set*. John Wiley & Sons. 8, 9, 32
- [Verbeeck et al., 2012] Verbeeck, J., Béch e, A., and Van den Broek, W. (2012). A holographic method to measure the source size broadening in STEM. *Ultramicroscopy*, 120:35–40. 10, 31, 74
- [Vollath, 2008] Vollath, D. (2008). *Nanomaterials: An Introduction to Synthesis, Properties and Applications*. Wiley. 5

- [Von Ardenne, 1938] Von Ardenne, M. (1938). Das elektronen-rastermikroskop. *Zeitschrift für Physik*, 109(9-10):553–572. 7
- [Wall and Hainfeld, 1986] Wall, J. and Hainfeld, J. (1986). Mass mapping with the scanning transmission electron microscope. *Annual review of biophysics and biophysical chemistry*, 15(1):355–376. 7
- [Wall and Simon, 2001] Wall, J. S. and Simon, M. N. (2001). Scanning transmission electron microscopy of DNA-protein complexes. *DNA-Protein Interactions: Principles and Protocols*, pages 589–601. 7
- [Wang, 2014] Wang, G. (2014). Plasmon excitation of atomic clusters and their assembly by electrons and photons. In *Journal of Physics: Conference Series*, volume 488, page 012046. IOP Publishing. 57
- [Wang, 1998] Wang, Z. (1998). The frozen-lattice approach for incoherent phonon excitation in electron scattering. How accurate is it? *Acta Crystallographica Section A: Foundations of Crystallography*, 54(4):460–467. 22
- [Wang et al., 2011] Wang, Z., Li, Z., Park, S., Abdela, A., Tang, D., and Palmer, R. (2011). Quantitative Z-contrast imaging in the scanning transmission electron microscope with size-selected clusters. *Physical Review B*, 84(7):073408. 8
- [Watanabe et al., 2001] Watanabe, K., Yamazaki, T., Hashimoto, I., and Shiojiri, M. (2001). Atomic-resolution annular dark-field STEM image calculations. *Physical Review B*, 64(11):115432. 42
- [Weickenmeier and Kohl, 1991] Weickenmeier, A. and Kohl, H. (1991). Computation of absorptive form factors for high-energy electron diffraction. *Acta Crystallographica Section A: Foundations of Crystallography*, 47(5):590–597. 24
- [Weiss et al., 1991] Weiss, J., Carpenter, R., and Higgs, A. (1991). A study of small electron probe formation in a field emission gun TEM/STEM. *Ultra-microscopy*, 36(4):319–329. 13
- [Weyland and Muller, 2005] Weyland, M. and Muller, D. (2005). Tuning the convergence angle for optimum STEM performance. *FEI Nanosolutions*, 1:24–35. 64
- [Wilson, 1990] Wilson, T. (1990). *Confocal Microscopy*. Acad. Press. 78
- [Wolf and Yip, 1992] Wolf, D. and Yip, S. (1992). *Materials Interfaces: Atomic-level Structure and Properties*. Springer Netherlands. 41

- [Xin and Muller, 2009] Xin, H. L. and Muller, D. A. (2009). Aberration-corrected ADF-STEM depth sectioning and prospects for reliable 3D imaging in S/TEM. *Journal of electron microscopy*, 58(3):157–165. 9, 78
- [Xu et al., 2015] Xu, R., Chen, C.-C., Wu, L., Scott, M., Theis, W., Ophus, C., Bartels, M., Yang, Y., Ramezani-Dakhel, H., Sawaya, M. R., et al. (2015). Three-dimensional coordinates of individual atoms in materials revealed by electron tomography. *Nature materials*, 14(11):1099–1103. 58, 72
- [Yang et al., 2015] Yang, H., Lozano, J., Pennycook, T., Jones, L., Hirsch, P., and Nellist, P. (2015). Imaging screw dislocations at atomic resolution by aberration-corrected electron optical sectioning. *Nature communications*, 6. 9, 78
- [Yankovich et al., 2014] Yankovich, A. B., Berkels, B., Dahmen, W., Binev, P., Sanchez, S., Bradley, S., Li, A., Szlufarska, I., and Voyles, P. M. (2014). Picometre-precision analysis of scanning transmission electron microscopy images of platinum nanocatalysts. *Nature communications*, 5. 58, 72
- [Yoshioka, 1957] Yoshioka, H. (1957). Effect of inelastic waves on electron diffraction. *Journal of the Physical Society of Japan*, 12(6):618–628. 24
- [Zhang et al., 2007] Zhang, Q., Kano, J., and Saito, F. (2007). Fine grinding of materials in dry systems and mechanochemistry. *Handbook of Powder Technology*, 12:509–528. 5
- [Zuo and Spence, 2016] Zuo, J. and Spence, J. (2016). *Advanced Transmission Electron Microscopy: Imaging and Diffraction in Nanoscience*. Springer New York. 22

List of symbols and abbreviations

Roman characters

Character	page	meaning
$()^T$	35	transposition of a vector or matrix
$\langle \rangle_t$	23	average over the time
C_3	15	spherical aberration of third order
C_5	15	spherical aberration of fifth order
$\text{cov}()$	37	covariance
$D(\mathbf{g})$	26	detector function
$\mathbb{E}[]$	36	expectation
E_0	43	acceleration voltage
e	17	electron charge
f_{kl}	26	fraction of electrons expected to be recorded at pixel (x_k, y_l)
f_{kl}^j	61	fraction of electrons expected to be recorded at pixel (x_k, y_l) at the tilt angle θ^j
	80	fraction of electrons expected to be recorded at pixel (x_k, y_l) at the defocus Δf^j
F	53	Fisher information matrix
$F(p, q)$	37	(p, q) th element of the Fisher information matrix
F^{-1}	37	inverse of the Fisher information matrix
$F^{-1}(p, p)$	37	elements of the diagonal of the inverse of the Fisher information matrix
\mathbf{g}	15	two dimensional spacial frequency vector
h	37	displacement of a component to calculate the numerical derivative
I	33	probe current
i	15	imaginary unit being equal to $\sqrt{-1}$
J	59	number of projections
j	17	index
K	33	number of pixels along the x -axis in STEM image
k	33	index
(k, l)	33	pixel at the position \mathbf{R}_{kl}
L	33	number of pixels along the y -axis in STEM image
l	33	index

\mathbf{k}_0	18	three dimensional wave vector
N_p	33	total number of detected electrons
$P(\boldsymbol{\omega}, \boldsymbol{\beta})$	35	joint probability density function
\mathbf{r}	17	three dimensional vector being equal to (x, y, z)
\mathbf{R}	15	two dimensional vector being equal to (x, y)
\mathbf{w}	35	vector of available observations
w_{kl}	35	observation at the measurement point $(x_k, y_l)^T$
w_{kl}^j	59	observation at the measurement point $(x_k, y_l)^T$ at the tilt angle θ^j
x	15	spatial coordinate
y	15	spatial coordinate
Z	57	atomic number
z	17	spatial coordinate
z_n	21	n slices
$\text{var}(\)$	37	variance

Greek characters

Character	page	meaning
α	15	objective aperture angle
α_0	43	convergence angle
$\boldsymbol{\beta}$	34	vector of position parameters
β_x	36	x -coordinate of the position of an isolated component
β_y	36	y -coordinate of the position of an isolated component
β_z	36	z -coordinate of the position of an isolated component
β_{x_p}	36	x -coordinate of the position of the p th component
β_{y_q}	36	y -coordinate of the position of the q th component
β_{z_s}	36	z -coordinate of the position of the s th component
λ	15	relativistic electron wavelength
λ_{kl}	34	expectation of Poisson distributed observation at the measurement point $(x_k, y_l)^T$
λ_{kl}^j	61	expectation of Poisson distributed observation at the measurement point $(x_k, y_l)^T$ at the tilt angle θ^j
	80	expectation of Poisson distributed observation at the measurement point $(x_k, y_l)^T$ at defocus Δf^j
∇	19	gradient operator in three dimensions
∇_{xy}	19	gradient operator in two dimensions
Δ	17	Laplacian's operator in three dimensions
Δ_{xy}	19	Laplacian's operator in two dimensions
Δf	15	defocus

Δf^j	80	j th image of depth sectioning experiment
Δx	34	pixel size of STEM image in the x -coordinate
Δy	33	pixel size of STEM image in the y -coordinate
Δz	78	depth resolution
Ω	25	volume of the slice
ω	35	vector of observations, which are considered as independent variables
ψ	15	wave function
σ	20	interaction parameter
$\sigma_{\beta_x}^2$	53	Cramér-Rao lower bound on the variance of the position coordinate β_x of a component
$\sigma_{\beta_y}^2$	53	Cramér-Rao lower bound on the variance of the position coordinate β_y of a component
σ_x	63	standard deviation with respect to x -axis
σ_y	63	standard deviation with respect to y -axis
σ_z	63	standard deviation with respect to z -axis
θ^j	59	j th tilt angle of electron tomography experiment
τ	33	dwel time
ε	20	slice thickness

Abbreviations

Abbreviation	page	meaning
0D	2	zero-dimensional
1D	2	one-dimensional
2D	2	two-dimensional
3D	2	three-dimensional
TEM	4	transmission electron microscopy
CTEM	4	conventional transmission electron microscopy
STEM	7	scanning transmission electron microscopy
HRTEM	7	high resolution transmission electron microscopy
ADF	11	annular dark field
CRLB	11	Cramér-Rao lower bound
HAADF	7	high angle annular dark field
TDS	7	thermal diffuse scattering
MS	20	multislice
GAM	61	Gaussian approximation method
FP	22	frozen phonon
AP	27	absorptive potential
FWHM	43	full width at half maximum

Samenvatting

Eigenschappen van materialen worden sterk bepaald door hun atomaire structuur en chemische samenstelling. De meeste eigenschappen van materialen op macroscopische schaal kunnen gemeten worden en zijn goed bekend. Voor kleine deeltjes echter, zoals nanodeeltjes en nanoclusters waarvan de grootte enkele nanometers is ($1 \text{ nm} = 10^{-9} \text{ m}$), zullen de eigenschappen verschillen van zowel atomen (moleculen) als van het materiaal op macroscopische schaal. Dankzij hun unieke eigenschappen en talrijke toepassingen voor een groot aantal materialen en ontwerpen is de interesse in deze nanodeeltjes enorm gegroeid binnen de wetenschappelijke en bedrijfswereld. Theoretisch en experimenteel kon aangetoond worden dat de structuur van deze nanomaterialen verband houdt met hun karakteristieke eigenschappen. Daarom is een gedetailleerde structurele en chemische karakterisering op atomaire schaal nodig om hun eigenschappen te begrijpen.

Hoge resolutie (HR) rastertransmissie-elektronenmicroscopie (STEM, scanning transmission electron microscopy) is ontwikkeld als één van de experimentele technieken om de interne structuur van materialen op atomaire schaal te bestuderen. Hoge hoek donkerbeeldvorming met een ringvormige detector (HAADF, high angle annular dark field) in het bijzonder, laat toe om beelden met atomaire resolutie van materialen te verkrijgen. Deze afbeeldingen zijn gevoelig voor de structuur en chemische samenstelling van het materiaal. Nochtans mag men niet vergeten dat STEM beelden tweedimensionale (2D) projecties zijn van een driedimensionaal (3D) object. Vaak zal een dergelijke afbeelding niet gebruikt kunnen worden voor een volledige 3D structurele en morfologische karakterisering. Elektronentomografie is daarom een standaardtechniek geworden om betrouwbare 3D informatie te verkrijgen. Deze techniek, gecombineerd met geavanceerde reconstructie-algoritmes, laat toe om atomen te visualiseren en zelfs de chemische samenstelling in sommige nanodeeltjes atoomsgewijs te bepalen.

Zodra atoomkolommen of individuele atomen in respectievelijk 2D of 3D zichtbaar zijn, wordt de volgende uitdaging om de posities en chemische samenstelling op een kwantitatieve manier te verfijnen zodat structuurparameters zo precies mogelijk gemeten kunnen worden. Hoewel HR STEM toelaat om sub-Ångström-resolutie te bereiken, zijn statistische parameterschattingsmethoden en beeldsi-

mulaties nodig voor een kwantitatieve structurele en chemische karakterisering. Statistische parameterschattingstheorie laat toe om parameters te schatten door een parametrisch model te fitten aan de experimentele beelden. Dit gebeurt door de parameters van het model iteratief te bepalen door een maat te optimaliseren die de overeenkomst tussen het experimenteel beeld en het model uitdrukt. Beeldsimulaties laten toe om de kwantummechanische oorsprong van de interactie tussen de elektronen en het specimen te interpreteren. Bovendien kunnen beeldsimulatie gebruikt worden om te vergelijken met de experimentele beelden als validatie van de geschatte parameters. De combinatie van statistische parameterschattingstheorie en beeldsimulaties is hier voorgesteld om een methode te ontwikkelen die toelaat om de theoretische limieten te kwantificeren waarmee atoomkolommen of atomen van een nanocluster in respectievelijk 2D of 3D gelokaliseerd kunnen worden uit een STEM experiment. Dit concept is onderzocht vanuit een theoretisch standpunt.

Deze thesis kan opgedeeld worden in vier delen. Het eerste deel bestaat uit een algemene inleiding waar de motivatie en het belang van het onderzoek beschreven worden in hoofdstuk 1. Het tweede deel geeft een samenvatting over de theoretische fysica achter de beeldvorming in STEM en de basisprincipes van statistische parameterschattingstheorie in respectievelijke hoofdstukken 2 en 3. Het derde deel bestaat uit de resultaten van het werk en wordt beschreven in hoofdstukken 4, 5 en 6. In hoofdstuk 4 wordt de betrouwbaarheid vergeleken van de twee meest populaire methoden om STEM beeldsimulaties uit te voeren. Dit gebeurt in functie van de parameters die gebruikt worden voor de kwantificatie van de beelden, namelijk de geïntegreerde intensiteit en de precisie van de atoomkolommen. In hoofdstuk 5 wordt onderzocht wat de theoretische limiet is waarmee atomen van een nanocluster in 3D gelokaliseerd kunnen worden op basis van een tiltserie beelden opgenomen met donkerbeeldvorming met een ringvormige detector (ADF, annular dark field) in STEM. Deze studie is gebaseerd op het concept van de Fisher informatiematrix dat toelaat om een uitdrukking af te leiden voor de hoogst haalbare precisie waarmee atomen gelokaliseerd kunnen worden in 3D. Verder worden sommige experimentele instellingen van de microscoop geoptimaliseerd met dit criterium. In hoofdstuk 6 wordt hetzelfde concept gebruikt om de haalbare precisie te onderzoeken waarmee de dieptelocatie van een atoom en het massamiddelpunt van een geïsoleerde atoomkolom gemeten kunnen worden uit een focuserie van beelden opgenomen in HAADF STEM. Daarenboven werd een 3D reconstructiemethode ontwikkeld gebaseerd op een focuserie HAADF STEM beelden. Tot slot worden in het vierde deel, in hoofdstuk 7, algemene conclusies getrokken en toekomstperspectieven besproken.

Publication

Papers in journals

1. Thickness dependence of scattering cross-sections in quantitative scanning transmission electron microscopy
G. T. Martinez, K. H. W. van den Bos, **M. Alania**, P. D. Nellist, S. Van Aert, submitted to Ultramicroscopy (2017)
2. Frozen phonon and absorptive model for high angle annular dark field scanning transmission electron microscopy: a comparison study in terms of integrated intensity and atomic column position measurement
M. Alania, I. Lobato, S. Van Aert, submitted to Ultramicroscopy (2017)
3. How precise can atoms of a nanocluster be located in 3D using a tilt series of scanning transmission electron microscopy images?
M. Alania, A. De Backer, I. Lobato, F.F. Krause, D. Van Dyck, A. Rosenauer, S. Van Aert, Ultramicroscopy accepted manuscript (2016)
<https://doi.org/10.1016/j.ultramic.2016.12.013>
4. Depth sectioning combined with atom-counting in HAADF STEM to retrieve the 3D atomic structure
M. Alania, T. Altantzis, A. De Backer, I. Lobato, S. Bals, S. Van Aert, Ultramicroscopy 177 (2017) 36–42
<https://doi.org/10.1016/j.ultramic.2016.11.002>

Conference abstracts

1. Towards 3D atomic structures through nanoparticle atom-counting: advances, challenges, and expectations.
S. Van Aert, A. De Backer, **M. Alania**, A. De wael, K.H.W. van den Bos, T. Altantzis, I. Lobato, L. Jones, G.T. Martinez, P.D. Nellist, and S. Bals, MMC 2017 Manchester
2. Model-based ADF STEM: from images towards precise atomic structures

in two and three dimensions.

S. Van Aert, K.H.W. van den Bos, A. De wael, **M. Alania**, A. De Backer, L. Jones, G.T. Martinez, S. Bals, and P.D. Nellist, MRS Fall meeting & exhibit, 2016, Boston-Massachusetts USA

3. Understanding the use of scattering cross-sections in quantitative ADF STEM.

Gerardo T Martinez, Karel H.W. van den Bos, **M. Alania**, Peter D Nellist, Sandra Van Aert, 16th European Microscopy Congress (EMC), 2016, Lyon-France

4. How precise can atoms of a nanocluster be positioned in 3D from a tilt series of scanning transmission electron microscopy images?

M. Alania, A. De Backer, I. Lobato, F.F. Krause, D. Van Dyck, A. Rosenauer, S. Van Aert, 16th European Microscopy Congress (EMC), 2016, Lyon-France

Acknowledgements

I would like to thank all the people who contributed in some way to the work described in this thesis. First and foremost, I would like to express my sincere gratitude to my academic promotor, Professor Dr. Sandra Van Aert, for accepting me into her group, for her continuous support during my PhD study and research, for her patience, motivation, enthusiasm, and immense knowledge. Her guidance helped me both for the research and writing of this thesis. Besides my promotor I want to express my appreciation and gratitude to Professor Dr. Gustaaf Van Tendeloo and Professor Dr. Dirk Van Dyck for promoting and supporting the collaboration between Peru and Belgium in the field of Materials science. I am very grateful to the members of my PhD committee for their interest in my work and reviewing my thesis, and giving me very useful remarks and feedback to improve this thesis. Every result described in this thesis was accomplished with the help and support of fellow group-mates and collaborators. Ivan Lobato, Annick De Backer and I worked together for most of the articles included in this thesis, and without their efforts my job would have undoubtedly been more difficult. I greatly benefited from their keen scientific insights, their knack for solving seemingly intractable practical difficulties, and their ability to put complex ideas into simple terms. Special thanks to Professor Dr. Andreas Rosenauer and Florian Krause from the University of Bremen for their collaboration and for providing access to the STEMSIM software. I would also like to thank Thomas Altantzis for useful discussions about STEM experiments and for providing very nice STEM images. It is a great pleasure to thank everyone of our group Karel van den Bos, Julie Gonnissen, Jarmo Fatermans, Annelies De wael, and Knut Müller-caspary for their interesting remarks and discussions during our Friday meetings. My gratitude also goes to all the administrative staff for their help in various aspects during my PhD, such as: Liesbet Laurens for her help with the design of the cover of the book, Sabine Van Deun, Marianne Samson, Christine Vanspreybroeck, Lydia Cassiers and Hilde Evans for their support and administrative assistance. In addition, I would like to express my gratitude to all the EMAT members for the friendly work atmosphere, scientific discussions, dinners and good moments during the last four years.

Finally, I would like to acknowledge friends and family who supported me during my time here. First and foremost, I would like to thank Mom, Dad, sisters, and brother for their constant love and support. Aurora Elvira, Fiorella Echevarria, Maria Filippousi, Maria Ebea, Javier Gonzales, Ricardo Egoavil, Robert Paria, and Victor Fernandez made my time here at Antwerp a lot more fun.